Thermochemical seasonal heat storage for the built environment

a multi-scale investigation

PROEFSCHRIFT

ter verkrijging van de graad van doctor aan de
Technische Universiteit Eindhoven, op gezag van de
rector magnificus, prof.dr.ir. F.P.T. Baaijens, voor een
commissie aangewezen door het College voor
Promoties, in het openbaar te verdedigen
op dinsdag 4 juli 2017 om 16.00 uur

door

Mohammadreza Gaeini

geboren te Teheran, Iran

Dit proefschrift is goedgekeurd door de promotoren en de samenstelling van de promotiecommisie is als volgt:

voorzitter:	prof.dr.	L.P.H. de Goey
1e promotor:	prof.dr.	H.A. Zondag
2e promotor:	prof.dr.ir.	D.M.J. Smeulders
copromotor:	dr. ir.	C.C.M. Rindt
leden:	prof.dr.	P. Neveu (Perpignan University)
	prof.dr.ir.	T.H. van der Meer (Twente university)
	prof.dr.ir.	G.P.J. Verbong
adviseur:	dr.-ing	H. Kerskes (Stuttgart University)

to my mother ...

TU/e Technische Universiteit
Eindhoven
University of Technology

Contents

Contents

GENERAL INTRODUCTION

1.1 Energy problem

Increasing the use of renewable energy sources is among the main topics under investigation all over the world, because of climate change and depletion of fossil fuel resources. According to the International Energy Agency (IEA), the building sector is responsible for 24 % of the world's total CO_2 emission, and is the largest consumer of energy, accounting for approximately 40 % of the world's total primary energy consumption[1], of which 75% is used for space heating and domestic water heating[2]. Therefore, a significant potential to reduce green house gas emissions exists by replacing fossil fuel by renewable energy in this sector. Energy storage is a key step to shift to renewable energy sources, which are inherently intermittent. Solar energy, as one of the most exploitable renewable energy sources, is available more than required in residential houses during summer, while during winter, it is insufficient to meet the heating demand. Figure 1.1 shows the mismatch between solar irradiation and heat demand (gas consumption). A solution is to store excess of solar thermal energy in summer using a so-called thermal battery, which can be discharged to provide heat for the residential demand in winter[3].

1.2 Thermochemical heat storage

Thermal storage technologies suitable for building applications are classified in three categories based on the storage principle used: sensible, latent and thermochemical heat storage[6]. The latter option is a promising method with a potentially high energy storage density[7], since heat can be stored in a compact and quasi loss-free way over a long time[8] by utilizing thermochemical materials (TCMs). In the thermochemical heat storage process, heat is stored
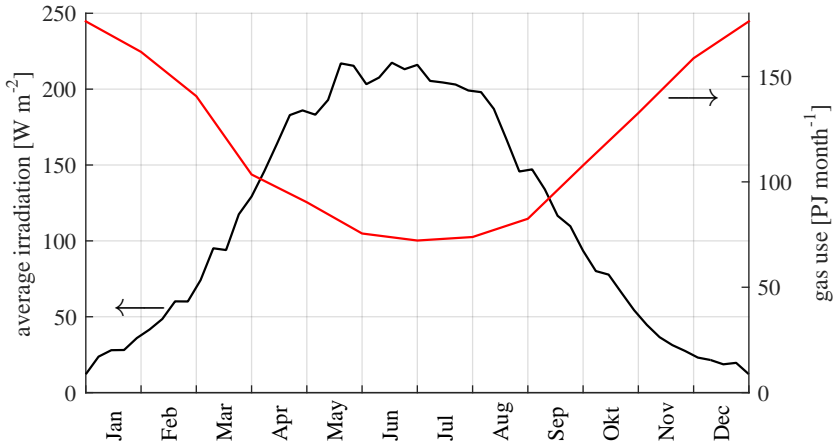
Figure 1.1: Solar irradiation per square meter[4] (average from year 1977 to 2015) and gas consumption[5] (average from year 2010 to 2015) in the Netherlands.

into an endothermal dissociation reaction, splitting the thermochemical material into two components (charging). At a later time, the energy can be retrieved from the reverse exothermal recombination reaction between the two components (discharging). A reversible chemical gas-solid reaction can be employed, that involves a solid state TCM as sorbent (A), according to the reaction $A(s) + B(g) \leftrightarrow AB(s) + heat$. Water vapor is mostly used as sorbate (B) in such systems for application in the built environment.

A schematic view of a typical thermochemical heat storage system is shown in Figure 1.2. Heat generated by a solar collector during summer (charging season) can be employed to desorb water from the material. Solar irradiation is converted into heat in a solar thermal collector, and used to heat up air. The air flow supplies heat to the reactor to charge the TCM, where sorbate (e.g. water vapor) is desorbed from the TCM and is drained to the ambient. The energy stored in this way can be retrieved during winter (discharging season) by introducing water vapor to the dehydrated material. Air from the ambient is directed through a humidifier (e.g. bubble column) and then to the reactor to react with the TCM. In a practical real system with application in the built environment, the moisture content of the air may be increased by additional evaporation of water using heat from a low temperature heat source such as a borehole[9]. Released heat in the reactor is transferred out of the reactor by the air flow. In the heat exchanger placed after the reactor, the heat in the air flow is transferred to the heat transfer fluid in
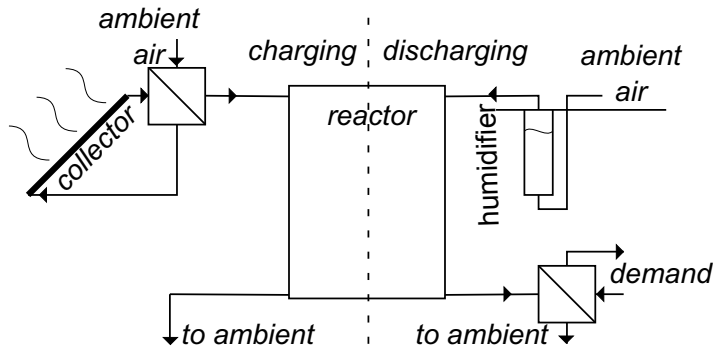
Figure 1.2: Schematic representation of a typical open thermochemical heat storage system.

the heating system (demand side).

1.3   Multi-level approach

The current lack of technological advancement in thermochemical heat storage systems can be described on three levels: material, reactor and system. Most of the research on heat storage is devoted to only one of these levels. However in order to overcome technological immaturities and to develop an optimized thermochemical heat storage system, simultaneous investigation on all levels is required. In this work, a multi-level approach is used to investigate the possibilities for thermochemical heat storage in the built environment.

1.3.1   System

In literature, both open and closed systems are investigated for long-term thermal storage of solar energy[10]. In an open system, both sorbate and energy are exchanged between the system and the environment, while in a closed system, only energy is exchanged between the system and the surrounding environment. In this work, an open system is considered, because the open system concept seems more promising for seasonal heat storage because of robustness and low cost[11]. An open sorption seasonal heat storage system for application in the built environment generally consists of a solar collector as the heat source, a borehole system as the humidifier, a sorption reactor for long term energy storage and a water vessel for short term energy storage to provide peaks in heating demand. In such a system, air is usually used as the carrier gas to carry water vapor as the sorbate into the reactor, and to transfer the released heat from the reactor to the load by convection. Since the amount of water vapor in air (or any other gas) is limited by the saturation humidity, the temperature step obtained in the reactor is limited due to the thermal mass of the airflow to be heated. In case of the built

environment, the highest possible inlet water vapor pressure is $13\,mbar$ (being the saturation water vapor pressure at 10^oC, which is a typical borehole temperature in the Dutch climate[9]). This can lead to a temperature lift of around 20^oC from a system based on zeolite. In order to cover the domestic hot water demand in a house, it is necessary to improve the system to be able to achieve higher temperatures.

Developing efficient operating conditions and strategies is another important aspect to be studied, specially for the the discharging process. Inefficiency in the charging process leads to an additional need of solar thermal energy during summer, which can simply be solved by using more solar collectors. However, inefficiency in the discharging process leads to shortage of the stored heat during winter. To solve this, more storage volume is required, which is critical. Therefore, more attention is given to the discharge process, in this work.

1.3.2 Reactor

The most important part of the seasonal sorption heat storage system is the reactor in which the material reacts with water vapor taken from humidified air. In this work, a packed bed reactor design is chosen, which is advantageous because of the low need of auxiliary energy in comparison with other types of reactors such as fluidized bed or screw reactors[12]. However, a disadvantage of the packed bed reactor design is the risk of formation of non-reactive zones, leading to a lower energy storage density. Therefore, in order to achieve a high efficiency of the thermochemical heat storage system, the reactor should be optimally designed for the intended reaction and operational conditions; which requires an in-depth understanding of the physical processes inside the reactor.

1.3.3 Material

An interesting storage material should be low-cost, non-toxic, non-corrosive and stable with fast reaction kinetics and high energy storage density[13]. For low temperature thermochemical heat storage [1], adsorption of water vapor on adsorbents[14], such as zeolite and silica gel, and hydration of salt hydrates[15], such as calcium chloride and strontium bromide, are frequently studied. In this work, zeolite 13X is used, in those places where the focus is on reactor or system performance. Although zeolite is too expensive (1-3 €/kg[16]) to be used in a full scale seasonal heat storage system, it is still a good candidate to be used in scientific studies because of its well-known properties and high stability[17].

---

[1]It is noted that the physical phenomenon of fixation or capture of sorbate (e.g. water vapor) by sorbent (e.g. zeolite) is defined under the term "adsorption" or "physi-sorption", where the sorption energy is typically related to the weak intermolecular forces (Van der Waals forces) and to hydrogen bonding and no activation energy is required. The term "thermochemical" refers to the "chemi-sorption", where stronger covalent bonding is involved[18]. However the expressions "thermochemical" and "sorption" are used interchangeably by authors[8]. Throughout this work, the term "thermochemical" is used also for the physi-sorption of zeolite, even though the process is not based on a chemical reaction, but on a physical ad/desorption reaction.

As mentioned, for a full scale seasonal heat storage in the built environment, other materials, such as salt hydrates, should be used. However, for salt hydrates, such as calcium chloride, the stability of the material is a serious concern. Therefore, in the material chapter, specific attention is given to the stability of the material, and attempts have been made to improve this stability. The effect of these stabilization methods on the performance of the material, such as kinetics and energy density, is investigated.

1.4   Objectives and outline

In order to develop an efficient thermochemical storage system with sufficient thermal power output, it is necessary to investigate the aforementioned levels in detail. The focus is on long-term thermal storage, utilizing thermochemical materials in an open system concept employing a packed bed reactor design. The main objective is to investigate the possibilities for thermochemical heat storage in the built environment. To that end, a multi-scale study is done to gain deeper insight into the material, reactor and system level. The following research questions are specifically addressed:

1. What are the key role playing parameters at the different levels?

2. How can the material be stabilized in an effective way? How are the kinetics and enthalpy of the reaction affected by the stabilization methods?

3. What are the effective phenomena determining the energy storage density of the reactor? How large are their effects and how can they be avoided?

4. How can the required temperature for the domestic demand from the system be achieved? How can the efficiency of the system be improved?

5. How can the thermochemical heat storage system be up-scaled in an effective way?

In chapter 2, a multi-level approach is described, in order to investigate the performance of the different levels (i.e. material, reactor and system). For this study a lab-scale test setup is realized and modelled numerically. By employing the validated model, predictions can be made for the dynamic thermal performance of a thermochemical heat storage system. Based on this primary study, the focus points which need to be visited on each level, will be established.

In chapter 3, investigation on the material level is performed. Specific attention is given to the stability of the material and the effects of stabilization methods on the performance of the material, such as kinetics and energy density. Calcium chloride hydrate, as a promising TCM, is tested in pure form, encapsulated in an inert material and impregnated in porous matrices. Samples of approximately 10 mg of the materials are tested in a TGA-DSC apparatus, in order to evaluate stability, cyclability, kinetics and energy density.

In chapter 4, investigation on the reactor level is performed. A detailed model of the transport phenomena occurring in the reactor, as the main part of the heat storage system, is developed, in order to evaluate the performance of the reactor. An efficient design for a large-scale thermochemical heat storage reactor is discussed.

In chapter 5, investigation on the system level is performed. A complete system setup consisting of all the components is realized and studied. For further studies on a complete thermochemical heat storage system, the simple reactor model presented in chapter 2 is combined with models for other parts of the system. Such a complete system model is employed to improve the system, in order to enable it for application in the built environment.

In chapter 6, the thermochemical heat storage system is up-scaled, and a pilot setup is designed and realized. The detailed knowledge gained in previous chapters on all the levels is applied to realize the pilot setup. The performance of the pilot setup is evaluated by experiments.

In chapter 7, conclusions are drawn on the performance of thermochemical heat storage systems on all three levels and recommendations for further research are given.

2

MULTI-LEVEL APPROACH

2.1 Introduction

As explained in the introduction, the investigation in this work is on three levels: material, reactor and system. A multi-level study on thermochemical heat storage is carried out in order to investigate the effect of the different levels on the global performance of the system. A feasible thermochemical heat storage system has to meet certain requirements regarding its global performance. Some indicators of the global performance of the system are for example thermal power output, energy storage density and efficiency. These indicators are strongly dependent on behaviour and specifications of different components of the system, such as material characteristics and reactor design.

Analysis on global performance of the system needs to be performed, in order to find the key parameters. For instance, *Michel et al. (2014)*[11] investigated closed and open thermochemical heat storage systems, and claimed that the mass transfer is the main limitation for the global performance of the open system, especially for reactors with large energy capacities. Therefore, the mass transfer phenomena occurring locally in the reactor, and hence the material reaction, are critical parameters effective on the global performance of the system. To study the effects of such local behaviours on the global performance of the system, a model is required. Such a model provides better understanding of the phenomena occurring in the system, and specifically inside the reactor as the most important part of the system.

In literature, models are developed for sorption heat storage reactors using zeolite as TCM for various types of applications. *Sun et al. (1995)*[19] first introduced a one dimensional model for the heat pump process, and further developed this

model into a two dimensional model[20]. This model is employed and developed further for other closed systems; for example, for an automobile waste heat adsorption cooling system[21], and for a sorption energy storage system for heating in buildings[22]. An extensive experimental and numerical investigation on the water vapor adsorption in zeolite 13X in an open system is performed by *Mette et al. (2014)*[23]. In all the mentioned investigations, it is found that the heat and mass transfer mechanisms occurring in the material bed are strongly coupled. This confirms the importance of developing a validated numerical model, which allows an in-depth understanding of the heat and mass transport phenomena in the reactor. The numerical model is an excellent basis for the design of the thermochemical heat storage reactor. In addition, the model can be used as a tool to study the dynamic behavior of the sorption process for different operating conditions.

In the above-mentioned models, local thermal equilibrium is assumed between the solid and gas phases. However, the phases are not in mass transfer equilibrium, and the local vapor transport between the phases is considered through reaction models. Rigorous Chemical Potential Driving Force (CPDF) models, such as the Fickian Diffusion (FD) model, can be used for analysing adsorbate transport within an adsorbent particle, in order to estimate the material reaction rate. In literature, comprehensive kinetic models have been developed to take into account the fundamental features of solid-state reactions at grain scale, but these models are quite cumbersome to handle at a continuum-scale[24]. In addition, the details of the performance calculation by such models, describing the local rates of adsorption at the particle scale, are often lost during up-scaling to process scale. *Ahn and Lee (2004)*[25] studied the effect of capillary condensation on adsorption and thermal desorption of water in zeolite 13X, by considering an elaborate model for the equilibrium amount of adsorbed water. *Dawoud et al. (2007)*[26] developed a non-isothermal model for adsorption of water vapor into a consolidated zeolite layer and studied the temperature dependence of the micropore diffusion. In all the mentioned works, a Linear Driving Force (LDF) model is used as the kinetics model. The LDF model with a lumped mass transfer coefficient, is frequently used for practical analysis of the dynamics of adsorptive processes[27], because it is simple, analytical, and physically consistent[28]. The LDF model is used here to express the kinetics of the water adsorption reaction into the material.

In this chapter, a lab-scale test setup is used as a proof-of-principle to study the concept for application in the built environment. The test setup is an open system working with a packed bed reactor filled with zeolite 13X as TCM. A model is developed for the transport phenomena occurring in the packed bed thermochemical reactor. The model incorporates the kinetics, isotherms and enthalpy of the water adsorption reaction into the material. The heat losses from the side wall of the reactor are considered by heat resistances in radial direction (quasi 2D). The model is validated by experimental results from the lab-scale test setup. The numerical and experimental results are used to calculate the heat fluxes in the reactor and are compared to evaluate the thermal performance of the system.

The model is used to investigate the performance of the material, of the reactor and of the system. The study concludes with recommendations for each level, acting as a basis for the investigations in the next chapters.

2.2 Lab-scale reactor setup

A lab-scale reactor is realized to work as a sorption heat storage system, working with water vapor adsorption on Zeolite 13X. The used zeolite 13XBF (CWK Chemiewerk Bad Köstritz GmbH[29]) consists of spherical beads with an average diameter of $2mm$. A schematic view of the setup is shown in Figure 2.1.

The inflow of the reactor is prepared in a controlled way, with respect to humidity and flow rate, by means of the GFC (Gas Flow Controller) and CEM (Controlled Evaporator Mixer). For hydration, air flow passes through the CEM where the air is mixed with the water flow coming from the water vessel regulated by a LFC (Liquid Flow Controller). For dehydration, an almost dry air flow passes through a heater, simulating the heat source (e.g. a solar collector), heating up the air to $180^{o}C$ to dehydrate the material.
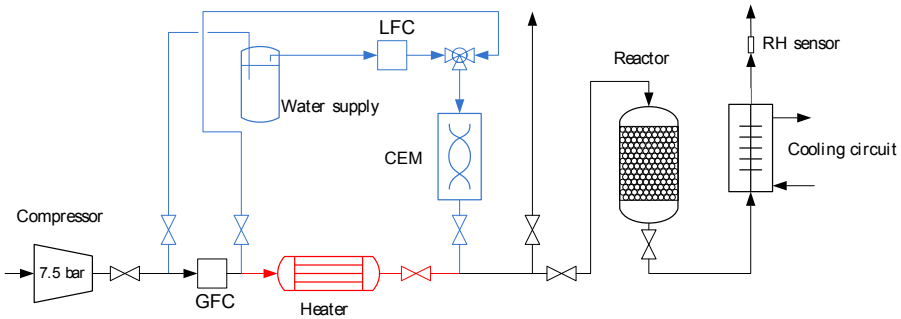
Figure 2.1: Schematic view of the lab-scale reactor setup

The reactor is a cylindrical tube, with an inner shell made of Teflon, because of its low thermal conductivity, and an outer shell made of stainless steel. In addition, a layer of glass wool insulation is used around the reactor in order to reduce the heat loss. The air flow enters the reactor from the top and leaves the reactor at the bottom. The zeolite is placed on top of a filter at the bottom of the reactor. The positions of the 17 thermocouples attached to the reactor are shown in Figure 2.2. Temperature is measured with thermocouples placed at the inlet (T_{in}) and outlet (T_{out}) of the reactor. Temperature is measured at five different heights numbered from 1 to 5 ($h = 90; 70; 50; 30; 10mm$), and three radii in the middle of the bed named M ($r = 0mm$), at the inside surface of the reactor body named B ($r = 35mm$) and at the outside surface of the stainless steel reactor wall named W ($r = 52.5mm$). Temperature and humidity at the outflow of the reactor is monitored by a humidity-temperature sensor. Since large errors in the absolute humidity can occur on low relative humidity measurements at high temperatures,

the sensor is positioned after a chiller that cools down the outflow, by which the relative humidity rises and, therefore, the absolute humidity can be determined more accurately. Properties of the adsorbent Zeolite 13X, characteristics of the reactor, and the operational conditions of the adsorption experiment are listed in Table 2.1.
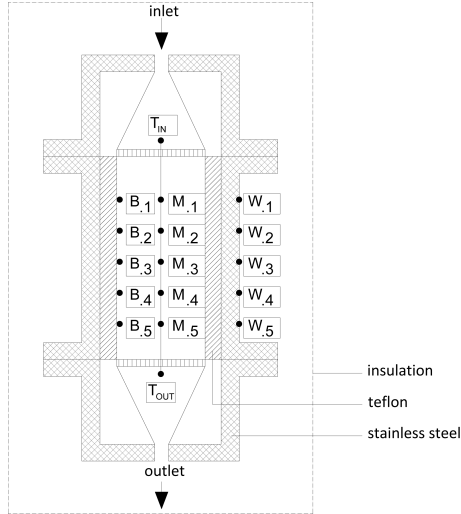
Figure 2.2: Schematic of the reactor with the position of the thermocouples located at five different heights (1-5) and in the middle of the bed (M), inside wall of the reactor body (B) and at the outside wall (W)

property	value [unit]
Bed porosity (ϵ_b)	0.4 $[-]$
particle density (ρ_p)	1150 $[kg/m^3]$
particle heat capacity ($C_{P,s}$)	880 $[J/Kg.K]$
particle thermal conductivity (λ_s)	0.4 $[W/m.K]$
Bed height (H)	0.12 $[m]$
Reactor inner diameter (D)	0.07 $[m]$
Teflon layer thickness (t_{tef})	0.075 $[m]$
Wall thickness (t_{ss})	0.01 $[m]$
Insulation thickness (t_{ins})	0.03 $[m]$
Air flow rate (ϕ)	0.001 $[m^3/s]$
inlet water concentration (c_{in})	0.3 $[mol/m^3]$
Ambient temperature (T_{amb})	21.5 $[^oC]$

Table 2.1: Properties of the adsorbent Zeolite 13XBFK[23], characteristics of the reactor, and operational conditions.

2.3   Water uptake of material

In this section, the hydration reaction of zeolite 13X is studied and modelled by the LDF model. In addition, the equilibrium isotherms and enthalpy of the reaction are investigated.

2.3.1   Kinetics model

For many adsorption systems, the diffusion-controlled kinetics may be satisfactory represented by the LDF approximation, first introduced by *Glueckauf (1955)*[30]:

$$\frac{dq}{dt} = k_{LDF}(q_{eq} - q) \tag{2.1}$$

where q and q_{eq} are the adsorbed and equilibrium loading of water in solid phase per kilograms of dry zeolite, and k_{LDF} is the LDF kinetics coefficient. In real adsorption systems, several mass transfer resistances affect the overall kinetics. The resulting kinetics coefficient $k_{LDF}[s^{-1}]$ is a lumped parameter that considers the external film resistance, the macropore resistance and the micropore resistance[31]:

$$k_{LDF} = \left(\frac{d_p}{6k_f} + \frac{d_p^2}{60\epsilon_b \delta_P} \right)^{-1} \tag{2.2}$$

The first term on the right hand side represents the mass transfer resistance in the external film of fluid around the particle. The mass transfer coefficient in the external film, k_f, can be obtained from the Sherwood number expressed by *Wakao and Funazkri (1978)*[32] in the range of Reynolds numbers from about 3 to 10000. However the dominant mass transfer resistance for the water vapor adsorption of zeolite 13X is the macropore diffusion resistance[31] presented by the second term on the right hand side of the equation above, in which δ_P is given by[33]:

$$\delta_P = \frac{1}{\tau} \left(\frac{1}{\delta_M} + \frac{1}{\delta_K} \right)^{-1} \tag{2.3}$$

where τ is tortuosity, and δ_P, δ_M and δ_K are the macropore, molecular and Knudsen diffusivity, respectively. The molecular diffusivity for the binary gas mixture of air and water can be evaluated by *Chapman-Enskog (1970)* theory[34], and the Knudsen diffusion by the kinetic theory[33].

The above mentioned kinetics coefficient k_{LDF} is usually only temperature dependent, however in some types of zeolite it is also concentration dependent[35]. The concentration dependency of the kinetics arises mainly from the thermodynamics correction factor; calculations by the corrected coefficient lead to better results[31]:

$$k_{LDF}^* = k_{LDF} \left(\frac{\rho_p R T}{\epsilon_p} \frac{\partial q_{eq}}{\partial p_v} \right)^{-1} \tag{2.4}$$

2.3.2 Equilibrium isotherms

Based on IUPAC classification, six isotherm shapes were identified for adsorption in solids[36]. The adsorption of water vapor on zeolite 13X at low water vapor pressure behaves as type 1[37], where the equilibrium loading of water in the adsorbed phase on zeolite, q_{eq}, is an exponential function of the water concentration in the gas phase. It can be expressed with the Langmuir ($n = 1$) or Langmuir-Freundlich ($n \neq 1$) isotherms:

$$q_{eq} = \frac{q_{max}(bp_v)^{1/n}}{1 + (bp_v)^{1/n}} \tag{2.5}$$

where q_{max} is the maximum amount of adsorbed water in high water vapor pressures, p_v is the partial pressure of water vapor, and b and n are temperature-dependent parameters, which can be described as follows[38]:

$$b = b_0 exp \left(\frac{\Delta E}{R T_0} (T_0/T - 1) \right) \tag{2.6}$$

$$\frac{1}{n} = \frac{1}{n_0} + \alpha \left(1 - T_0/T \right) \tag{2.7}$$

where T_0 is the reference temperature (that is assumed to be 273.15 K in this work), and b_0 and n_0 are the adsorption affinity constant and exponent constant at the reference temperature, respectively. ΔE is the activation energy for desorption.

Experimental information about the water uptake on zeolite 13XBFK is provided by the manufacturer at temperatures of 25, 80 and 95$^o C$. The Langmuir and Langmuir-Freundlich equations are fitted to the experimental data and the model parameters are extracted. Results are presented in Table 2.2. *Mette et al. (2014)*[23] approximated the adsorption equilibrium water loading using the Dubinin-Astakhov equation which is based on the micro-pore filling theory of Polanyi[39]. The comparison between the experimental data, Langmuir-Freundlich and Dubinin-Astakhov fit is shown in Figure 2.3. The isotherm model with the obtained fitting parameters is generalized for all temperatures and is implemented in the model.

2.3.3 Enthalpy of reaction

By using the van't Hoff equation, a concentration dependent form of the adsorption enthalpy can be obtained as follows[38]:
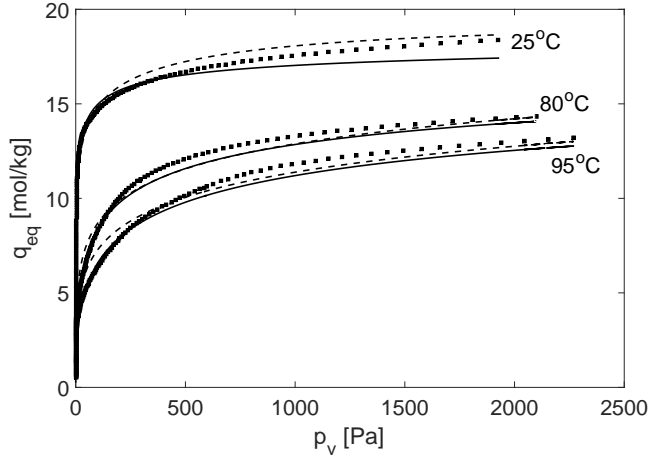
Figure 2.3: Zeolite 13X water uptake isotherms for temperature of 25^oC, 80^oC and 95^oC; experimental data (dots), Langmuir-Freundlich fitted curves (solid lines) and Dubinin-Astakhov fitted curves (dash lines).

parameter	Langmuir	Langmuir-Freundlich
q_{max} $[mol/kg]$	16	19
b_0 $[1/Pa]$	1.730	4.002
$\Delta E[J/mol]$	51800	65572
n_0 [-]	1	2.976
α [-]	0	0.377

Table 2.2: parameters of the Langmuir and Langmuir-Freundlich equilibrium models for adsorption of water vapor on zeolite 13X

$$\Delta H = \Delta E - (\alpha R T_0)n^2 ln \left(\frac{q}{q_{max} - q} \right) \qquad (2.8)$$

In Equation 2.8, temperature dependency of the maximum loading (q_{max}) is assumed to be negligible. The adsorption enthalpy for the Langmuir-Freundlich isotherm (Table 2.2) is calculated and is presented in Figure 2.4. As can be seen, the adsorption heat decreases with water loading. The Langmuir-Freundlich isotherm model, despite having the correct finite capacity at sufficiently large pressures, is applicable only in the intermediate range of water loading ($0 < q < q_{max}$).

13
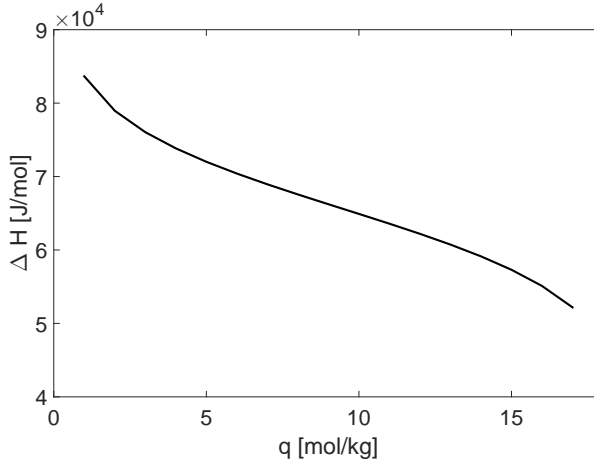
Figure 2.4: Adsorption enthalpy at different water loadings for zeolite 13XBF.

2.4 Transport phenomena in reactor

In this section, a non-isothermal and non-adiabatic model including mass and energy transfer equations is developed, to study the thermal performance of the reactor. The equations in the model which describe the dynamics of the system are formulated under the following assumptions: (a) the flow in the reactor can be described by an axially dispersed plug flow model[40]; (b) heat transfer in radial direction through the bed and the reactor walls can be modeled as a one-dimensional resistance model; (c) the gas phase behaves as an ideal gas and is in thermal equilibrium with the solid phase; (d) the adsorbent beads have identical characterizations and the bed properties are uniform. The temperature distribution problem is determined by two PDEs, one for the bed temperature (T_b) and the other one for the reactor wall temperature (T_R), connected by heat resistances. An schematic view of the model is shown in Figure 2.5. The bed and wall temperatures are solved in the nodal points in axial direction and are in contact through the resistances in radial direction.

By considering these assumptions, the governing heat and mass balances can be written by a set of PDEs along the vertical axial coordinate (z) and the time (t). The velocity can be evaluated based on $u = \phi/A$, where ϕ and A are the gas flow rate and cross-sectional area of the bed.

The water mass balance is expressed based on the water vapor concentration, c:

$$\epsilon_b \frac{\partial c}{\partial t} + u \frac{\partial c}{\partial z} - D_z \frac{\partial^2 c}{\partial z^2} + (1 - \epsilon_b)\rho_p \frac{dq}{dt} = 0 \tag{2.9}$$

where ϵ_b is the bed porosity, ρ_p is the particle density, q is the averaged amount of adsorbed water per kg of zeolite and D_z the axial dispersion coefficient, which
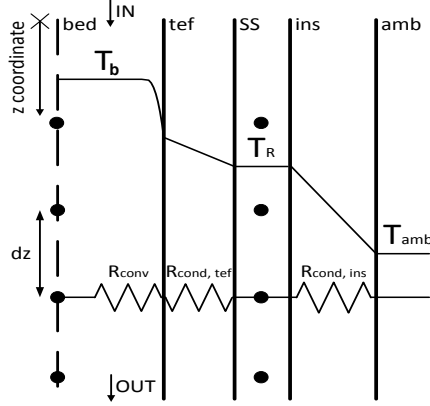
Figure 2.5: Schematic of the 1D model in axial direction with the heat resistances in radial direction (quasi 2D model) for the reactor shown in Figure 2.2.

can be calculated based on the Peclet number:

$$D_z = u d_p / P e_z \tag{2.10}$$

Here Peclet number based on axial dispersion coefficient $P e_z$ is derived from Gunn's correlation[40].

The energy balance in the bed is given based on the bed temperature (temperature of the gas and solid phases in the bed), T_b:

$$\overline{\rho C_P} \frac{\partial T_b}{\partial t} + \rho_g C_{P,g} u \frac{\partial T_b}{\partial z} - \lambda_{eff} \frac{\partial^2 T_b}{\partial z^2}$$

$$- (1 - \epsilon_b) \rho_p \frac{dq}{dt} \Delta H + \frac{4}{\pi d_i^2} \frac{(T_b - T_R)}{R_i} = 0 \tag{2.11}$$

The effective thermal conductivity in axial direction, λ_{eff}, can be estimated by the model of *Zehner and Schlünder*[41] which is satisfactory over a broad range of solid-to-fluid thermal conductivities and solid fractions, as follows:

$$\frac{\lambda_{eff}}{\lambda_g} = 1 - \sqrt{1 - \epsilon_b} + \frac{2\sqrt{1 - \epsilon_b}}{1 - B/\beta} \left(\frac{(1 - 1/\beta)B}{(1 - B/\beta)^2} ln(\frac{\beta}{B}) - \frac{B+1}{2} - \frac{B-1}{1 - B/\beta} \right) \tag{2.12}$$

with B the shape factor which for spherical particles can be approximated as $B = 1.25 \left(\frac{1-\epsilon_b}{\epsilon_b} \right)^{10/9}$ and $\beta = \lambda_p / \lambda_g$ the particle to gas heat conductivity ratio.

The overall volumetric heat capacity, $\overline{\rho C_P}$, consists of several terms as shown in Equation 2.13, which are the heat capacity of the air in the bed voids (first term), the heat capacity of the air in the beads pores (second term), the heat capacity of the solid (third term) and the heat capacity of the adsorbed water (fourth term).

It is dominated by the third and forth terms because of the higher density of the solid phase compared to the gas phase.

$$\overline{\rho C_P} = \epsilon_b \rho_g C_{P,g} + (1 - \epsilon_b)\epsilon_p \rho_g C_{P,g}$$
$$+ (1 - \epsilon_b)\rho_p C_{P,p} + (1 - \epsilon_b)\rho_p q C_{P,v} M_v \quad (2.13)$$

In Equation 2.11, the last term represents the heat loss from the inside reactor wall, at inner diameter of the reactor d_i, per unit of reactor volume. The heat loss through the reactor wall is modeled by considering wall temperature (T_w) and the thermal mass of the reactor wall in another energy balance for the reactor wall:

$$\rho_R C_{P,R} \frac{\partial T_R}{\partial t} - \lambda_{SS} \frac{\partial^2 T_R}{\partial z^2} = \frac{(T_b - T_R)}{R_i A_R} - \frac{(T_R - T_{amb})}{R_o A_R} \quad (2.14)$$

in which d_i and d_o refer to the inner and outer diameters of the reactor, R_i and R_o represent the heat resistances at the inner and outer sides of the wall, and A_R is the cross-sectional area of the body of the reactor wall. The heat resistance at the inner side of the wall (R_i) is a summation of the convective heat resistance at the inside wall and the conductive heat resistance in the teflon layer ($R_i = R_{cond,tef} + R_{conv}$), see Figure 2.5. According to *Ahn et al.* [42] considering heat transfer in a packed bed, the relation between the Nusselt number and the Reynolds number is assumed to be similar as the case of heat transfer of flow in a circular tube. In this model, the convective heat resistance at the inside wall is calculated using the Nusselt number relation presented in Equation 2.15:

$$Nu_{PM} = 0.309 Re_{PM}^{0.8} Pr \quad (2.15)$$

where the Reynolds number in the porous medium is defined as $Re_{PM} = d_p u \rho_g / \mu_g (1 - \epsilon_b)$ and Pr is the Prandtl number. The heat resistance at the outer side of the wall (R_o) is mainly determined by the conductive heat resistance of the insulation layer. The convective heat resistance at the outside surface of the insulation layer is neglected ($R_o = R_{cond,ins}$).

2.5 Energy balance of system

The energy flows which contribute to the heat balance are shown in Figure 2.6. The energy produced during the adsorption ($P_{reaction}$) is partly consumed to heat up the material inside the reactor itself ($P_{sensible}$), and the rest leaves the reactor by means of air flow through the reactor ($P_{convection}$) or is lost from the bed to the reactor body (P_{loss}). The net energy theoretically should be zero, thus the heat balance is:

$$P_{convection} - P_{reaction} + P_{sensible} + P_{loss} = 0 \quad (2.16)$$

The abovementioned energy flows can be calculated by the equations presented in Table 2.3 for the experimental and numerical results. The convection
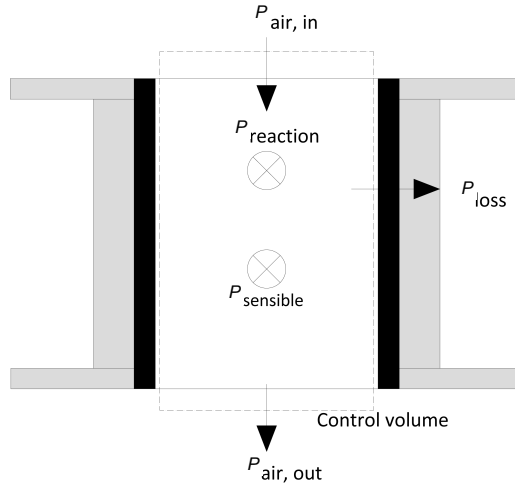
Figure 2.6: Schematic view of the energy flows in the reactor (shown in Figure 2.2).

term (first term in Table 2.3) in the reactor is calculated as the difference between the convective heat transfer by the outflow and inflow air, which are calculated based on the flow rate and the temperature of the outlet (T_{out}) and inlet (T_{in}) of the reactor (second and third terms in Table 2.3), respectively. The thermal power produced by the reaction (fourth term in the Table 2.3) is calculated based on the experimentally measured water accumulation in the reactor (($\dot{m}_{v,in} - \dot{m}_{v,out})/M_v$), and based on the numerically calculated reaction rate (dq/dt) integrated over the entire length of the bed (L). The stored sensible heat in the bed (fifth term in Table 2.3) is calculated based on the time derivative of the bed temperature integrated over the whole length of the bed. To determine the experimental value of this term, it is assumed that in each of the bed segments ($i = 1, 2, ...5$) the bed temperature is equal to the measured temperature at the center of the bed at the thermocouple positions M1-5. The thermal loss power (sixth term in Table 2.3) is calculated based on the temperature difference between the inside and outside wall of the reactor, and the heat resistance of the wall (R) integrated over the entire length of the bed. The calculated heat flows over time based on the numerical and experimental results are shown in Figure 2.12. The total produced or consumed powers are integrated during the entire process time and the resulting energies are presented in Table 2.4.

2.6 Model validation

The complete model as presented in section 2.4, is developed and solved in COMSOL Multiphysics, which is a Finite Element Method (FEM) based program. The final set of equations consists of four PDEs:

#	term	experimental	numerical
1	$P_{convection}$	$P_{air,out} - P_{air,in}$	$P_{air,out} - P_{air,in}$
2	$P_{air,out}$	$(\dot{m}_a C_{P,a} + \dot{m}_{v,out} C_{P,v}) T_{out}$	$(\rho_{air} C_{P,a} + c_{out} M_v C_{P,v}) \phi_a T_{out}$
3	$P_{air,in}$	$(\dot{m}_a C_{P,a} + \dot{m}_{v,in} C_{P,v}) T_{in}$	$(\rho_a C_{P,a} + c_{in} M_v C_{P,v}) \phi_a T_{in}$
4	$P_{reaction}$	$\frac{\dot{m}_{v,in} - \dot{m}_{v,out}}{M_v} \Delta H$	$\int_0^H \rho_b A_b \Delta H \frac{dq}{dt} dz$
5	$P_{sensible}$	$\sum_{i=1}^{5} \overline{\rho C_P} A_r \frac{\Delta T_{Mi}}{\Delta t} \Delta L$	$\int_0^H \overline{\rho C_P} \frac{dT_b}{dt} dz$
6	P_{loss}	$\sum_{i=1}^{5} \frac{T_{Bi} - T_{Wi}}{R} \Delta L$	$\int_0^H \frac{T_b - T_R}{R} dz$

Table 2.3: equations of energy flows in the reactor

- Equation 2.9 for modeling the water concentration in the gas phase (c);

- Equation 2.11 for modeling the bed temperature (T_b);

- Equation 2.14 for modeling the wall temperature (T_R);

- Equation 2.1 for modeling the water loading in the solid phase (q).

The PDEs are discretized in space by Lagrange linear shape functions. Both the bed and wall domains are meshed with an element size of $1mm$ (chosen based on a mesh convergence study). The solver is a fully coupled time-dependant solver. A Backward Differentiation Formula (BDF) scheme (with a maximum order of 5 and a minimum order of 1) with an initial time step of 0.001 s is used as the time stepping method. The relative, absolute and event tolerances are set to 1E-2. The model is validated by means of comparing the numerically calculated and the experimentally measured temperature profiles, and further by comparison between the thermal fluxes calculated by the model and the ones calculated based on the experimental results.

In order to validate the model, experiments are performed for the conditions as presented in Table 2.1. Figure 2.7 shows the temperatures that are experimentally measured at the inlet and outlet of the reactor and at the thermocouple positions $M1 - 5$. The temperature of the bed increases immediately after the start of the experiment because of the reaction in the bed near the inlet section. The heat is convected to the downstream sections by means of the flow through the bed. Hence the temperature is increased all over the bed. The measured inlet temperature T_{in} (which is also used as the inlet temperature in the numerical model) gradually drops at the beginning of the experiment since the temperature in the humidifier (CEM unit in Figure 2.1) drops due to the evaporation energy extracted from it. Since the reaction causes an almost fixed temperature step in the bed, a higher inlet temperature will result in higher bed and outlet temperatures. So the slightly higher temperature at the inlet at the start of the experi-

ment is the reason for the corresponding initial peaks in the temperature of the bed and the outlet air. During this peak, the outlet temperature T_{out} is slightly lower than the bed temperature, which is caused by the heat loss to the reactor wall. While the wall temperature increases over time, the heat transfer to the wall decreases due to the heating up of the wall and the outflow temperature becomes equal to the bed temperature. After the material at a certain position in the bed is completely hydrated and the reaction is finished, the temperature at the corresponding location in the reactor drops to the cold air inflow temperature. The reaction front passes along the height of the bed and the temperature at each height (at the thermocouple positions M1-5) drops when the reactive zone is passed. The temperature at the outlet of the reactor, T_{out}, remains high, because of the reaction heat released in the reactive zone which is moving through the bed over time. This process continues until almost $15000s$ when the reaction is finished everywhere in the bed.
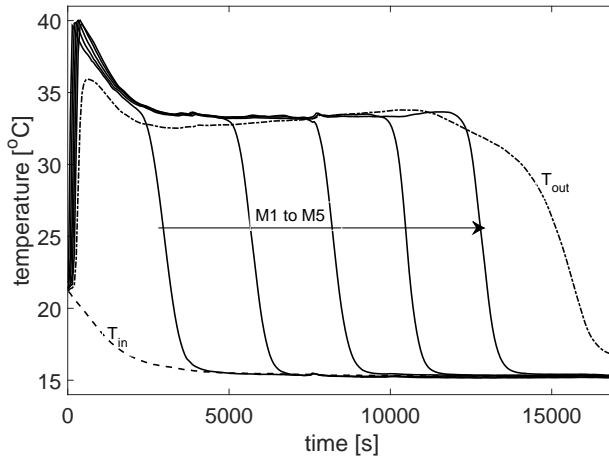
Figure 2.7: Temperatures measured at the inlet and outlet of the reactor and at the thermocouple positions $M1-5$, for the experiment with the operational conditions mentioned in Table 2.1.

The numerically calculated and experimentally measured temperatures at five different heights in the bed (M1-5) are compared in Figure 2.8. The comparison of bed temperatures shows good agreement. The calculated wall temperatures in the model are compared to the experimentally measured temperatures at five different heights (W1-5) in Figure 2.9. The calculated wall temperatures show a faster increase and decrease and higher maximum than the measured ones. That is probably because of over estimation of the heat transfer coefficient at the inside wall of the reactor in the model. A lower heat transfer between the bed and the wall can also explain the slightly slower decrease in the bed temperature calculated by the model at the end of the cool down process at each height, since the wall looses its heat to the airflow more slowly than calculated.
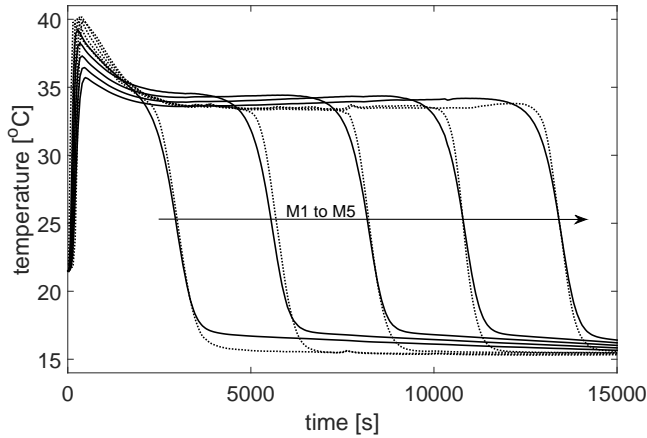
Figure 2.8: Numerical (solid) and experimental (doted) bed temperature at the thermocouple positions $M1 - 5$, for the experiment with the operational conditions mentioned in Table 2.1.
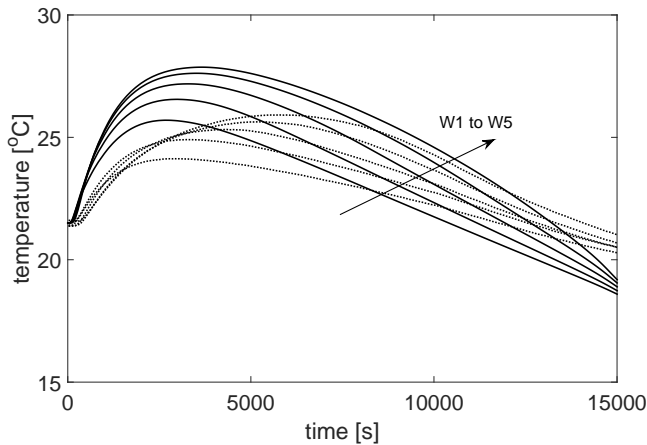
Figure 2.9: Numerical (solid) and experimental (doted) reactor wall temperature at the thermocouple positions $W1 - 5$, for the operational conditions mentioned in Table 2.1.

2.7 Results and discussion

2.7.1 Material performance

Several simulations are run with different equilibrium fits and kinetics coefficients, in order to investigate the influence on the results. The temperatures calculated and measured in the middle of the bed at the thermocouple position

$M3$ are compared, since the temperature profiles at the other thermocouple positions show the same trend. In Figure 2.10, the results from the model with Langmuir-Freundlich and Langmuir adsorption isotherms, using the parameters in Table 2.2, are compared with the experimental results. The Langmuir-Freundlich isotherm shows a better prediction of the temperature in the reactor than the Langmuir isotherm, which is expected according to the higher accuracy of the Langmuir-Freundlich fit.
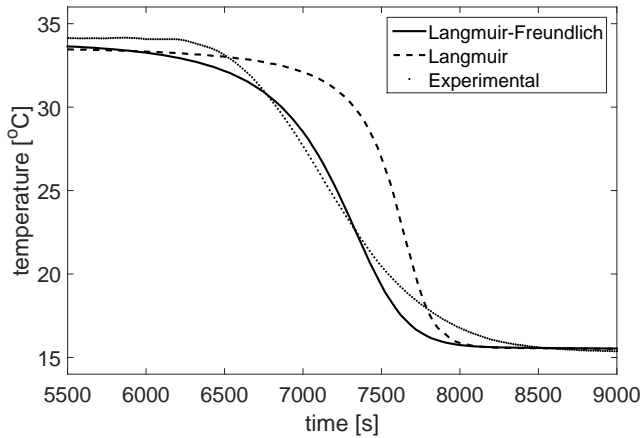
Figure 2.10: Temperature profiles at the thermocouple position $M3$ for different equilibrium isotherms, for the operational conditions mentioned in Table 2.1.
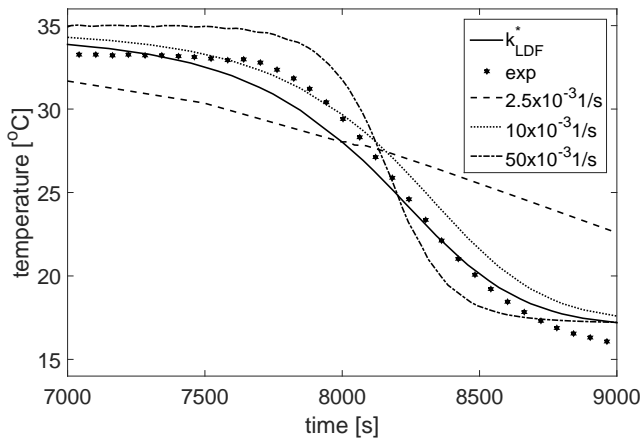
Figure 2.11: Temperature profiles at the thermocouple position $M3$ for different kinetics coefficients, for the operational conditions mentioned in Table 2.1.

The effect of the kinetics coefficient of the adsorption reaction (k_{LDF}) on the temperature profile in the reactor is investigated, and the result at the thermocouple position $M3$ is presented in Figure 2.11. By increasing the kinetics coefficient, the temperature drop becomes steeper (a sharper reaction interface). The best result is obtained when the kinetics coefficient is around $0.001 s^{-1}$, and it is best formulated by the corrected coefficient (indicated as k_{LDF}^*).

2.7.2 Reactor performance

The heat fluxes from Table 2.3 are calculated based on both the experimentally measured temperatures and numerically calculated temperatures. As can be seen in Figure 2.12, the calculated heat fluxes based on the experimental and numerical results are in good agreement, except for some deviations for the convection and reaction powers at the end of the process. The difference in the reaction power follows the same trend as the difference between calculated and measured water vapor concentrations at the outlet of the reactor (Figure 2.13). The water vapor concentration at the outlet of the reactor increases when the bed is fully hydrated and no more water can be adsorbed by the material. The measured water vapor concentration increases slower compared to the simulated one. This slower increase does not seem to be related to any limitation in the kinetics of the zeolite, since the decline in temperature after passing of the thermal front is very rapid, as shown in Figure 2.7. Possibly, this effect may be related to a faster completion of the reaction in the near wall region than in the center of the reactor allowing vapor to pass in the near-wall region, while the reaction in the center is still ongoing. This could be caused by several effects, such as e.g. non-uniform flow due to higher porosity near the wall, or due to less effective drying of the zeolite during the charging state due to heat losses at the wall. The model, with the assumption of one dimensionality, is not able to determine the significance of these effects and validity of these hypotheses. It suggests that for better understanding of heat and mass transfer phenomena in radial direction, a more sophisticated investigation of the modeling is needed; however the difference is only seen in the powers at the end of the process, and has only a limited effect on the energy, as the power is overestimated in one part (from around 11000s to 15000s) and underestimated in another (after 15000s).

Total energies are calculated by integrating the heat fluxes over the entire time of the process ($E = \int_0^{t_{end}} P$), and are presented in Table 2.4. The error in experimentally calculated energies is calculated as $error = E_{convection} - E_{reaction} + E_{sensible} + E_{loss}$.

As can be seen in Figure 2.12 and Table 2.4, the heat loss to the wall based on the numerical results is higher than the one based on the experimental results, because the heat loss based on the experimentally measured temperatures becomes negative after around 8000s. It means that the reactor wall releases part of its sensible heat back to the bed instead of losing it to the ambient. For the numerical results, this happens in a later stage of the process. The heat loss predicted by the model in the first phase, when the heat loss is positive and the wall temperature
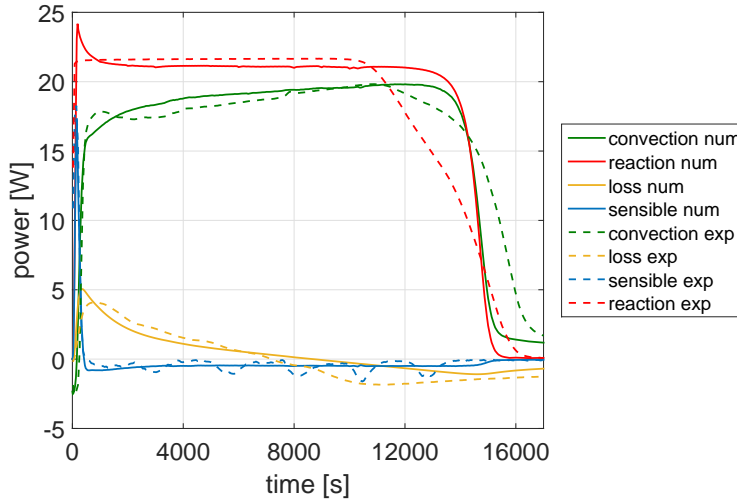
Figure 2.12: Numerical (solid) and experimental (dotted) heat fluxes in the reactor during the hydration process, for the operational conditions mentioned in Table 2.1.

term	experimental [kJ]	numerical [kJ]
$E_{convection}$	277	270
$E_{reaction}$	287	295
$E_{sensible}$	-3	-7
E_{loss}	8	32
error	-5	0

Table 2.4: Total energies calculated based on experimental and numerical results, for the operational conditions mentioned in Table 2.1.

is increasing, is close to the measured value. It suggests that the heat transfer coefficient at the inside wall when the reactor body is releasing heat to the bed should be calculated in a different way than when the heat is transferred from the bed to the wall. In this specific condition, the heat loss and the sensible heat stored in the bed are negligible compared to the reaction heat and the convection heat transfer by the air flow. That is because the stored sensible heat in the bed and most of the heat loss from the bed to the wall are released again to the air in a later phase of the process. This happens when the temperature of the air drops. The calculated sensible heats are negative because the starting bed temperature is higher than the inlet temperature at the end of the process (Figure 2.7) due to the cooling down of the humidifier by evaporation ($T_{in} < T_{amb}$).
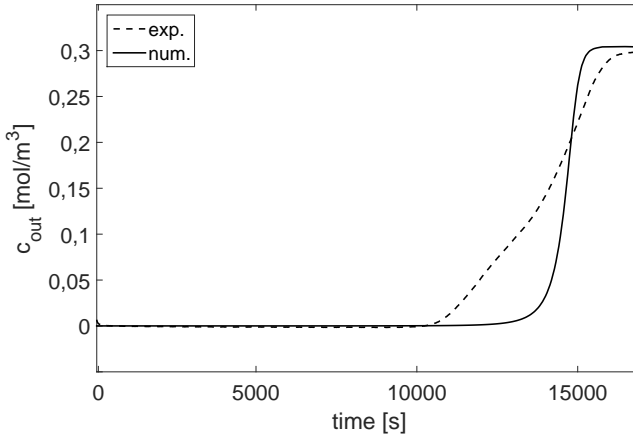
Figure 2.13: Numerical and experimental concentrations at the outlet of the reactor, for the operational conditions mentioned in Table 2.1.

2.7.3 System performance

In section 2.6, the model is validated by the experimental results from the lab-scale reactor with the characteristics presented in Table 2.1. In this section, the validated model is used to study the effect of different parameters on the performance of an up-scaled system with the characteristics presented in Table 2.5. The effect of the kinetics coefficient and the residence time on thermal performance of a thermochemical heat storage reactor under full scale normal operating conditions is investigated. A segment of a large scale reactor with a segment volume of about $51L$ is defined in the model and a larger air flow rate (compared to the lab-scale case) is applied to get a high heating power in the order of $1kW$. The inlet water concentration is chosen at around $13mbar$ water vapor pressure, and the whole reactor is initially at ambient temperature. The characteristics of this large scale reference case are presented in Table 2.5.

property	value
Bed height (H)	$0.56\ m$
Reactor inner diameter (d_i)	$0.34\ m$
Reactor outer diameter (d_o)	$0.35\ m$
Air flow rate (ϕ)	$0.04\ m^3/s$
inlet water concentration (c_{in})	$0.57\ mol/m^3$
Ambient temperature (T_{in})	$21.5\ °C$

Table 2.5: Characteristics of the large scale reference case

Effect of kinetics coefficient

The thermal performance of the reactor for different kinetics coefficients is investigated by introducing the efficiency of the reactor as $\eta = E_{convection}/E_{reaction}$ and the average power ($E_{convection}/t_{end}$) of the reactor. The results are shown in Figure 2.14 and Figure 2.15, respectively, for three cases where the inlet temperature is set as: (1) the experimentally measured inlet temperature in the lab-scale experiment, (2) ambient temperature, and (3) $40^0 C$. The first case is the one presented in Figure 2.7. The second one is simulating the condition that the humid cold air is heated up to the ambient temperature before entering the reactor. The third case is resembling the reactor under normal operating conditions for heating purposes in the built environment. In this case, since the achievable temperature step in the reactor by means of the reaction is limited, a heat recovery system should be used to preheat the inflow air of the reactor. This can be done by transferring the existing excess of heat in the exhaust air from the system, which is discussed in chapter 5.

In Figure 2.14 for the first case ($T_{in} = T_{exp}$), it can be seen that the efficiency slightly decreases for larger values of the kinetics coefficient. A higher efficiency is obtained for a slower reaction, caused by the fact that the inlet temperature is lower than the ambient temperature. It means that at a certain time in parts of the reactor where the reaction is finished, the bed actually gains energy from the ambient, so the efficiency increases by decreasing the kinetics coefficient. By increasing the inlet temperature to the ambient temperature, the change in the efficiency of the reactor for different kinetics coefficients is not significant, because there is no energy gain from the ambient. By further increase in the inlet temperature to $40^0 C$ the efficiency drops further. For this case, the efficiency decreases for lower values of the kinetics coefficient. Because of slow reactions, the total process time is larger, which leads to a higher heat loss.

In Figure 2.15, it can be seen that the power is lower for higher inlet temperatures due to the higher heat loss, but for the higher kinetics coefficient this difference is small. The declining trend of the average power by decreasing the kinetics coefficient is similar in all the cases. In addition, the average power decreases for lower values of the kinetics coefficient, which leads to a smaller temperature step. A lower temperature in the reactor leads to a higher water uptake by the zeolite material (Figure 2.3), and more adsorption energy is released. Also heat loss decreases because of the smaller temperature gradient over the reactor wall. It can be seen that for the kinetics coefficients larger than around $0.001s^{-1}$ the efficiency remains in a same range. On the other hand, for faster reaction (higher kinetics coefficient) the total adsorption energy produced is lower because of the lower water uptake at higher temperatures, and the heat loss is larger. This is caused by the larger temperature gradient over the reactor wall. However, the total reaction time is shortened because of the fast reaction. Hence, the change in the total heat loss energy is limited, resulting in almost the same efficiencies for high kinetics coefficients.
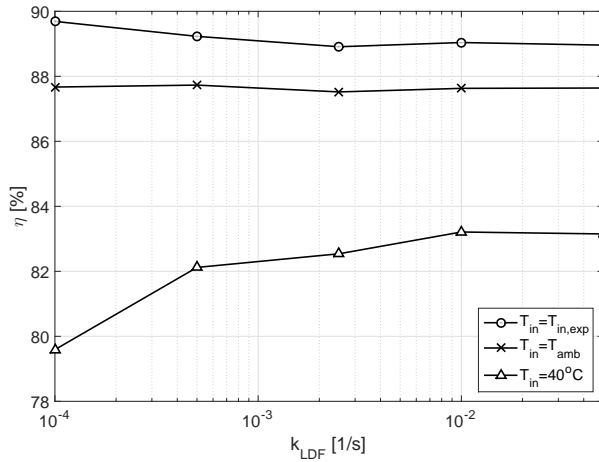
Figure 2.14: Effect of the kinetics coefficient on the efficiency of the up-scaled reactor at different inlet temperatures, for the operational conditions mentioned in Table 2.5.
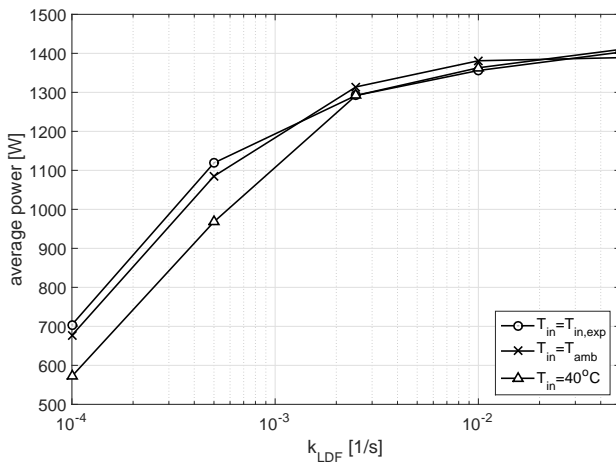
Figure 2.15: Effect of the kinetics coefficient on the average power of the up-scaled reactor at different inlet temperatures, for the operational conditions mentioned in Table 2.5.

Effect of residence time

A parameter study is carried out into the effect of the gas flow rate on thermal performance of a thermochemical heat storage reactor under full scale normal operating conditions. The same reactor as in the previous section is considered (Table 2.5) and the results are presented in Figure 2.16. The efficiency of the reactor in all the cases increases by increasing the gas flow rate to around $80l/s$. By

further increasing the gas flow rate for the cases with inlet temperature the same as in the lab-scale experiment and with the inflow at ambient temperature, the efficiency stays the same. However, the efficiency decreases for high volumetric flows for the case with the inlet temperature at 40^oC. An optimum flow rate of around $80l/s$ can be seen for this case.
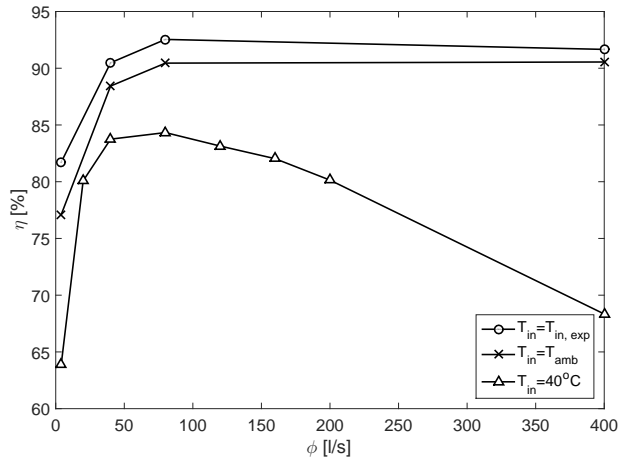
Figure 2.16: Effect of the flow rate on the efficiency of the up-scaled reactor at different inlet temperatures, for the operational conditions mentioned in Table 2.5.

In order to investigate the effect of the gas flow rate on the performance of reactors with different sizes, the residence time of the gas flow in the reactor is defined as the reactor volume divided by the gas flow rate. The efficiencies of reactors with different sizes for different residence times are shown in Figure 2.17. In all cases the aspect ratio of the bed is the same ($H/D = 1.65$). By increasing the size of the reactor, the efficiency generally increases. For each reactor size, there is an optimum residence time (around 0.6- 0.7 s), which corresponds to an optimum flow rate. The optimum flow rate for each reactor size is shown in Figure 2.18, and the optimum residence time is found to be 0.62 s.

The effect of the kinetics coefficient on the efficiency of a reactor with a volume of 51 liter is investigated (Figure 2.19). By decreasing the kinetics coefficient, the efficiency of the reactor generally decreases. The optimum efficiency of the reactor (at the optimum residence time) drops from around 84% for a kinetics coefficient of 100×10^{-4} to around 53% for a kinetics coefficient of 0.10×10^{-4}. In addition, the curves get flatter for lower kinetics coefficients, which means that the efficiency of the reactor is less sensitive to the residence time change. In other words, the performance of a thermochemical reactor is limited by the kinetics for the case of a slow reaction, and by the flow rate for the case of a fast reaction. This can be seen in Figure 2.20, where each point represents the optimum efficiency of a reactor (with volume of $51L$) working with the corresponding kinetics coefficient. The points are fitted with a linear function to the inverse of the kinetics
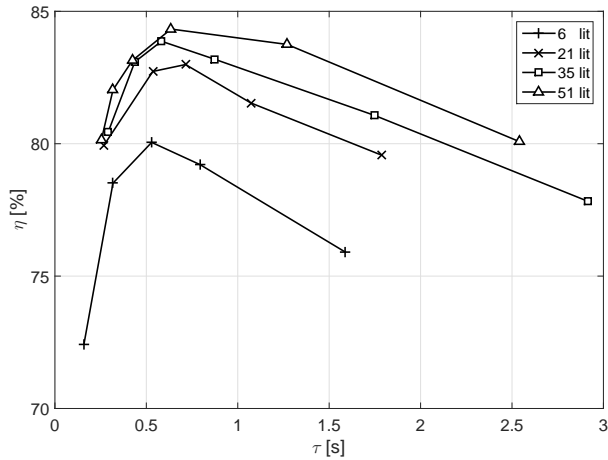
Figure 2.17: Effect of the gas residence time in the reactor on the efficiency of the up-scaled reactor for the different reactor volumes with the inlet temperature at 40^0C (the kinetics coefficient is calculated by Equation 2.4).
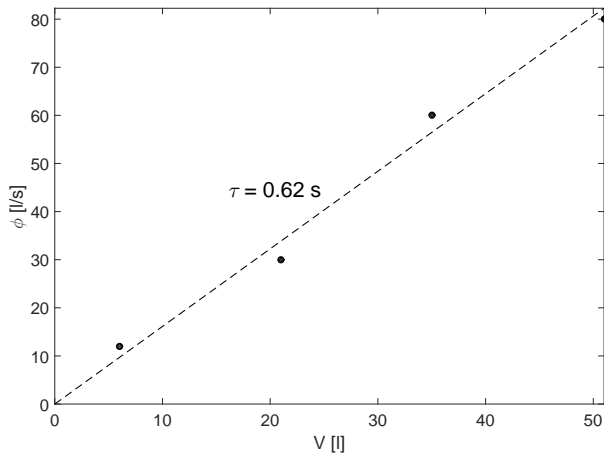
Figure 2.18: Optimum residence time for different reactor volumes with the inlet temperature at 40^0C (the kinetics coefficient is calculated by Equation 2.4).

coefficient. For slower reaction (smaller values of kinetics coefficients in the right hand side of the graph) the optimum residence time is larger, because the water vapor in the flow needs more time to be adsorbed by the material. However, for fast reactions (larger values of the kinetics coefficients in the left hand side of the graph) the optimum residence time is not dependent on the kinetics coefficient but has a constant value of $\tau = 0.62s$, as shown Figure 2.18. This suggests that

for fast reactions the optimum residence time is related to the inflow water concentration and the kinetics coefficient as $\tau \approx c_{in}.V_m/k_{LDF}$, where V_m is the molar volume of water vapor, which is around $0.0224m^3/mol$ for ideal gas at 25^0C temperature and $1atm$ pressure. However, it needs to be checked for other inflow water concentrations.
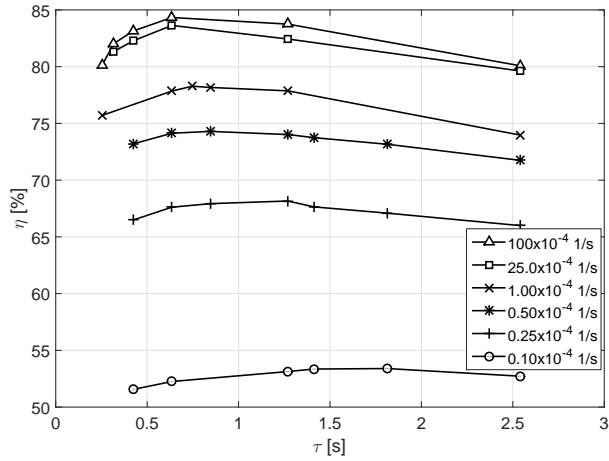
Figure 2.19: Effect of the gas residence time on the efficiency of the up-scaled reactor with a segment volume of $51L$ and the inlet temperature at 40^0C for different kinetics coefficients.
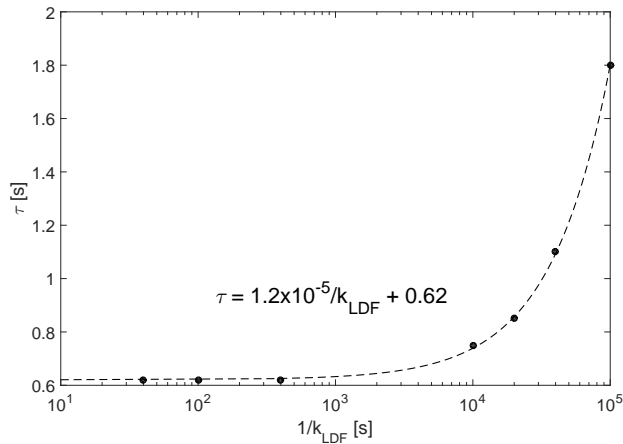
Figure 2.20: Optimum flow rate in the up-scaled reactor with a segment volume of $51L$ and the inlet temperature at 40^0C for different kinetics coefficients.

2.8 Conclusions

A study using a multi-level approach is performed on thermochemical heat storage, in order to investigate the performance of the different levels (i.e. material, reactor and system). A lab-scale test setup is realized and modelled numerically. The test setup is an open system working with a packed bed reactor filled with zeolite 13X as TCM. The numerical model is a non-isothermal and non-adiabatic model to simulate the thermal performance of the test setup. The model is validated by comparing the numerically calculated and experimentally measured temperatures in the material bed. By employing the validated model, predictions can be provided for the thermal performance of a thermochemical heat storage system.

On the material level, the effect of the adsorption reaction between the gas and solid phases on the thermal performance of the system is investigated. In particular, attention is given to the choice of the isotherm model between Langmuir and Langmuir-Freundlich. Based on a comparison between model and experiment, it is found that the Langmuir-Freundlich fit is a better option than a simple Langmuir fit, although using the Langmuir fit makes the simulation slightly faster. For the LDF model, an accurate value of the kinetics coefficient is determined to be the one corrected by the thermodynamics correction factor (presented in Equation 2.4).

On the reactor level, the thermal powers are calculated to study the performance of the reactor. The model is also validated by comparing the numerically and experimentally determined thermal powers. The calculated heat fluxes based on the experimental and numerical results are in good agreement, except for some deviations for the convection and reaction powers at the end of the process. The powers calculated based on the model drop faster compared to the ones calculated based on the experiment. The difference in the reaction power follows the same trend as the difference between calculated and measured water vapor concentrations at the outlet of the reactor. The water vapor concentration at the outlet of the reactor increases when the bed is fully hydrated and no more water can be adsorbed by the material. The measured water vapor concentration increases slower compared with the simulated one. This slower increase does not seem to be related to any limitation in the kinetics of the zeolite, since the decline in temperature after passing of the thermal front inside the bed is very rapid. Possibly, this effect may be related to a faster completion of the reaction in the near wall region than in the center of the reactor allowing vapor to pass in the near-wall region, while the reaction in the center is still ongoing. This could be caused by several effects, such as non-uniform flow due to higher porosity near the wall, or due to less effective drying of the zeolite during the charging state due to heat losses at the wall. The model developed in this chapter, with the assumption of one dimensionality, is not able to determine the significance of these effects and validity of these hypotheses.

On the system level, the model is used to study the performance of an up-scaled system. Effects of the material performance and reactor design on the

efficiency and average power are studied. The effect of the kinetics coefficient on the efficiency of a large scale reactor is studied. It is found that faster adsorption (kinetics coefficient from $0.0001s^{-1}$ to $0.1s^{-1}$) increases both the efficiency (from around 80% to around 83%) and the thermal power output of the reactor (from around $0.6kW$ to around $1.4kW$). However, this effect is only significant below a threshold value of the kinetics coefficient, which for the present case is found to be about $0.001s^{-1}$. Above this threshold value, the effect of the kinetics coefficient on the efficiency and the power of the reactor is small. It is found that for each reactor size there is an optimum flow rate. The maximum efficiency at the optimum residence time decreases drastically by decreasing the kinetics coefficient for large reactor size. For the present case a residence time of about $0.62s$ provides maximum efficiency in a large scale reactor. The optimum residence time (and hence the optimum flow rate) is not dependent on the kinetics coefficient of the reaction for large values of the kinetics coefficient (in this case, higher than around $0.001s^{-1}$). For smaller values of the kinetics coefficient, a further decrease in the kinetics coefficient causes an increase in the optimal residence time. For fast reactions (large kinetics coefficients) the optimum residence time seems to be related to the inflow water concentration and the kinetics coefficient as $\tau \approx c_{in}.V_m/k_{LDF}$, where V_m is the molar volume of water vapor. However, this needs to be checked for other inflow water concentrations.

Based on the multi-level study performed in this chapter, the focus points, which need to be studied in the next chapters, are established.

In this chapter, zeolite is used as TCM because of its high stability. However, for a full scale seasonal heat storage in the built environment, zeolite is too expensive and other materials, such as salt hydrates, should be used. For salt hydrates, the stability of the material is a serious concern. Therefore, in chapter 3 specific attention is given to study the stability of the material, and attempts have been made to improve the stability of the materials. The effect of stabilization on the performance of the material, such as kinetics and energy density, is investigated.

Since mass and heat transfer are determining phenomena dictating the performance of a reactor, an accurate model describing these phenomena is an indispensable tool to come to an efficient design of a large-scale thermochemical heat storage reactor. This study shows that the radial effects at the inside wall of the reactor play an important role in predicting proper heat fluxes values. Therefore, the model will be improved in chapter 4 by considering the radial effects in a 2D calculation. This will increase the computational time, but it can be helpful to get more detailed insight.

The simple system studied in this chapter was limited to the reactor boundaries. However, a complete thermochemical heat storage system consists of other components as well. For further studies on a complete thermochemical heat storage system in chapter 5, the simple reactor model presented in this chapter is combined with models for other parts of the system. Such a complete system model can predict the thermal performance of the system and be applied to the energy analysis, design and optimization of a new thermochemical heat storage system.

The upscaling of the thermochemical heat storage system is finally done in chapter 6, where the design and realization of a pilot setup is discussed.

3

MATERIAL PERFORMANCE

3.1 Introduction

For low temperature thermochemical heat storage, salt hydrates are frequently investigated. The studies are done on material level[15] and system level. Several Prototypes are built based on salt hydrates, such as magnesium chloride[9] and strontium bromide[43].

Calcium chloride is one of the promising salt hydrates for thermochemical heat storage for common building applications[44]. A reversible chemical gas-solid reaction can be employed that involves $CaCl_2$, according to the de-re/hydration reaction of $CaCl_2.xH_2O(s) + heat \leftrightarrow CaCl_2.(x-y)H_2O(s) + yH_2O(g)$. A review on the use of calcium chloride in applied thermal engineering is done in[45]. The interest for calcium chloride has been triggered by: easy availability and subsequently cheap price (0.1-0.4 €/kg[16]), high capacity for water uptake and energy storage, relatively better chemical stability than other salt hydrates, low corrosiveness and non-toxicity. Furthermore, the material dehydrates at low temperature (below 100^oC), which makes it suitable for the applications.

The equilibrium loading of $CaCl_2$ at a vapor pressure of $1.3kPa$ at different discrete temperatures is taken from the phase diagram of calcium chloride[46] shown in Figure 3.1. The equilibrium loading at two temperatures (20^oC and 30^oC) is also measured in the experiments (explained in the next sections) and shown in the figure. The data are well fitted with a power function as shown in the figure, which will be used in the results section. It should be noted that the equilibrium loading curve for the solid state (the part below the aqueous solution line) should have a step function shape. These steps should be visible at 6, 4, 2, 1 and 0 state of hydration values. Therefore, the real equilibrium loading can

be express by the step function, however a pseudo-equilibrium loading can be express by the extrapolated function.
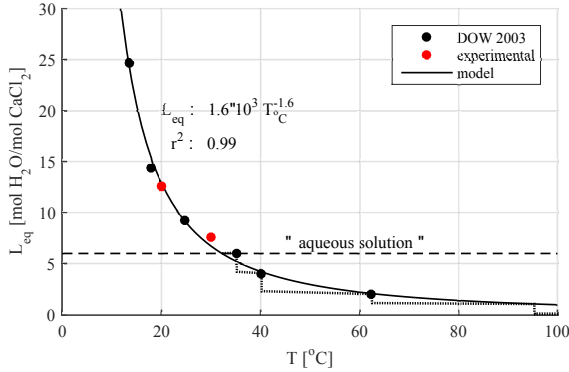
Figure 3.1: The equilibrium loading of calcium chloride under a vapor pressure of $1.3 kPa$.

The hydration reaction steps for known states of hydration for calcium chloride (an-, mono-, di-, tetra- and hexahydrate) with the reaction enthalpies are presented in Table 3.1. During the hydration process, after a certain state of hydration liquefaction occurs, which is caused by the depression of the melting point upon water uptake. This is caused by the highly hygroscopic nature of the material. In practice, this means the formation of an aqueous solution instead of a solid state material. Dehydration of such overhydrated solution yields an agglomerated bulk of solid material, instead of the initial powdery porous form. Agglomeration is an undesirable behavior of the material as TCM, because it prevents or decelerates the subsequent water uptake process. Therefore, most thermochemical storage studies do not intend to use calcium chloride in pure form. A solution for this problem is the use of additional materials, which helps to stabilize the physical structure of the material. However, this can decrease the energy storage density and/or reaction rate.

reaction	$\Delta h [kJ/mol_{salt}]$
$CaCl_2 + H_2O \rightarrow CaCl_2.H_2O$	71.6
$CaCl_2.H_2O + H_2O \rightarrow CaCl_2.2H_2O$	51.9
$CaCl_2.2H_2O + 2H_2O \rightarrow CaCl_2.4H_2O$	117.1
$CaCl_2.4H_2O + 2H_2O \rightarrow CaCl_2.6H_2O$	120.7
$CaCl_2 + 6H_2O \rightarrow CaCl_2.6H_2O$	361.3

Table 3.1: Enthalpies of reactions between calcium chloride hydrates and water vapor[47].

The major concern at this stage is liquefaction followed by washing out of ac-

tive material and agglomeration into large chunks of salt, thus deteriorating the diffusive properties of the structure. These features make the material unfit for application in a thermochemical heat storage system, since stability is required for many cycles. Preventing the overhydration to be reached would help stabilizing the material. However, this means restricting the conditions to which the reactor material is exposed during storage. This is hard to accomplish without the use of energy and technology to prevent either low temperatures or high humidity values from occurring in the system. Apart from additional costs, this will make the system more complicated. Furthermore, in case of failures like leakages in the reactor wall or power outage, stability of the calcium chloride based material cannot be guaranteed.

In literature, attempts have been made to make calcium chloride stable for thermochemical heat storage. For example, with a simple mixture of $CaCl_2$ and $MgCl_2$, *Rammelberg et al. (2013)*[48] obtained a higher cycle stability and higher reaction enthalpy than the combined effect of both salts taken individually. *Iyimen-Schwarz & Lechner (1983)*[49] have shown that the addition of alumina powder decreases the aglomoration but also decreases the energy storage density (15 %), by the addition of the neutral substances. Impregnation of salt hydrates into a porous matrix is used by *Aristov et al. (1996)*[50] in order to join the pronounced heat-storing properties of salt hydrates with the stability of porous solids. Some of the used porous matrices in literature are: iron silicate[51], silica gel[52,53], zeolite[14], activated carbon[54], bentonite[55], and some mesoporous materials[56].

Microencapsulation is another approach for the stabilization of salt hydrates, although it is not so common in the context of thermochemical energy storage. In this approach (salt hydrate) particles are enveloped with a second inherently stable material to prevent coalescence or agglomeration. Recently, there is a growing interest in the microencapsulation of inorganic phase change materials[57]. More specifically, the microencapsulation of CaCl2 hydrates has been reported by *R. Cuypers et al.*[58]. It is claimed that both the physical stability and reaction kinetics can be enhanced, however it still needs to be investigated more elaborately.

In literature, the performance of the material under investigation is usually studied with Thermo-Gravitational Analysis (TGA) and Differential Scanning Calorimetry (DSC) methods. These methods are mostly used to evaluate the water release and energy gain of materials during the dehydration reaction, because it is a faster reaction, therefore, the results can be more accurate. However, the rehydration reaction is an important part of the cycle in which overhydration might happen blocking the water vapor transport in the material. Therefore, the hydration reaction of the material is of high interest in this chapter. The focus is on stabilization of the material during the hydration reaction without decreasing the kinetics and energy density significantly.

In this chapter, specific attention is given to the stability of calcium chloride-based materials, since it is a serious concern as discussed. Attempts have been made to stabilize calcium chloride by impregnation in expanded natural graphite and vermiculite, and by encapsulation with ethyl cellulose. The effect of these stabilization methods on the performance of the material, such as kinetics and

energy density, is investigated. Characterization of the materials is carried out with combined TGA and DSC, in order to evaluate the improvements on the basis of three subjects: reaction kinetics, heat storage density and stability.

3.2 Composite materials

Four calcium chloride-based materials are studied as presented in Table 3.2: pure salt (P), calcium chloride impregnated in expanded graphite (G), calcium chloride impregnated in vermiculite (V) and encapsulated calcium chloride powder (E). The samples are identified on basis of the dry calcium chloride content instead of the gross mass. The impregnated samples are noted with 1 as once impregnated and 2 as twice impregnated.

The pure salt is used in powder form and the estimated state of hydration for the material in the container is two moles of water per mole of calcium chloride ($CaCl_2.2H_2O$). However, due to the hygroscopic nature of the material, the water uptake after being taken out of the container and exposed to the room conditions is fast. The initial state of the calcium chloride for experiments is therefore not defined accurately. Because of this, samples are dehydrated at high temperature (150^oC) at the beginning of each experiment.

The encapsulated material is produced by spray-drying a solution of calcium chloride and ethyl cellulose in a solvent mixture composed of ethanol and water[58]. The resulting formed particles are composed of a calcium chloride dihydrate core and an ethyl cellulose shell. The respective mass fractions of calcium chloride and ethyl cellulose are $80wt\%$ and $20wt\%$. Ethyl cellulose is a hydrophobic material, i.e. swelling with water is practically negligible, and is highly permeable for water vapor.

The remaining two materials consist of salt impregnated into porous structures of vermiculite and expanded graphite. Vermiculite mainly consist of aluminium, iron and magnesium silicates minerals. Heat treatment of this material provides a porous and layered structure, having a large surface area per unit of volume. Vermiculite (Agra M4-Seedo) with a packed density of around $111kg/m^3$ and a particle size smaller than $2mm$ is used. The expanded graphite has also a layered structure with a high porosity, and is obtained by exposing graphite to high temperatures. A plate of expanded natural graphite (Sigraflex Thermophit L-sheet) with a density of $92kg/m^3$ is used to cut cylinders of $20mm$ diameter and $9mm$ thickness. A high internal porosity of around 95% is calculated, based on the density of pure graphite ($2150kg/m^3$).

Before impregnation, the host materials are submerged in ethanol alcohol, over a night in order to remove any dirt and enhance the salt content. However, for vermiculite, the attempt to remove impurities by alcohol actually reduced the uptake of salt, so the method was abandoned. Impregnation was carried out by submerging the host materials in a saturated aqueous solution of calcium chloride over a night in order to deposit the salt in the pores of the matrix. Then the water was removed in two thermal steps, first at 90^oC over a night, and then

at $190^o C$ in a convection stove. Subsequently, the samples are cooled down in a desiccator in order to protect them from moisture in the ambient.

The samples under the name V2 and G2 were impregnated twice, to increase the salt content. The second impregnation is done with the same method, and result in a considerable increase in the salt content of the samples. A different impregnation technique was also tried by submerging the host materials in molten calcium chloride salt at $800^o C$. This method was however abandoned, because it resulted in a decrease in salt content instead of an increase, as well as in agglomeration of the salt.

code	synthesis method	passive material	salt content [$wt\%$]	density [kg/m^3]	estimated porosity
P	pure	-	100	660	0.7
G1	impregnation	expanded graphite	73	300	0.9
G2	impregnation	expanded graphite	87	600	0.7
V1	impregnation	vermiculite	68	320	0.9
V2	impregnation	vermiculite	86	600	0.7
E	encapsulation	ethyl cellulose	80	190	0.9

Table 3.2: Materials.

For the pure and encapsulated materials, the volumetric bulk density is directly measured with a micro balance in a crucible with known volume. The materials are filled into the crucible without applying any force to compress the material, same as the samples used in the experiments. It is assumed that the state of hydration of the samples is $CaCl_2.2H_2O$. The calculated standard deviation is less than 7%. For the impregnated materials, the volumetric density is calculated based on the density of calcium chloride and the host materials in solid state from literature, and salt content (mass of active material to total mass of sample). The salt content can be calculated based on weighing the samples before and after the impregnation procedure, or based on the experimental results from the TGA (explained in section 3.4).

3.3   TGA-DSC experiments

The characterization of TCM is based on measurement data, obtained through the methods of Thermo-Gravitational Analysis (TGA) and Differential Scanning Calorimetry (DSC). A Simultaneous Thermal Analysis (STA) apparatus (Netzsch STA 449 F3 Jupiter) connected to a Modular Humidity Generator (MHG ProUmid) is used, which allows for simultaneous measurement of both the mass change (TGA) and the heat release/uptake (DSC) of a sample. The STA apparatus consists of a thermally controlled environment (furnace), which is subjected to a pre-defined temperature program. Sample is situated in an aluminium crucible located in the furnace, with a typical sample mass of 5 to $20mg$. An empty

crucible is located just beside the sample crucible as reference for the DSC measurement. The crucibles are assumed to be subject to identical conditions. Both crucibles are positioned on a sample holder, which is mounted on a balance. The humidity generator provides an air flow with a controlled flow rate, temperature and humidity. The air flow is from top to the bottom of the furnace. A schematic view of the setup is shown in Figure 3.2.
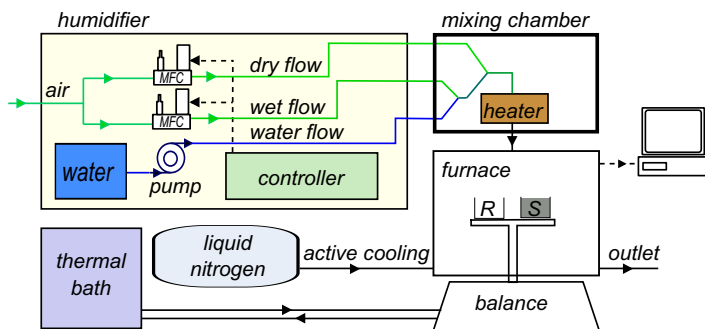
Figure 3.2: Schematic view of TGA-DSC setup.
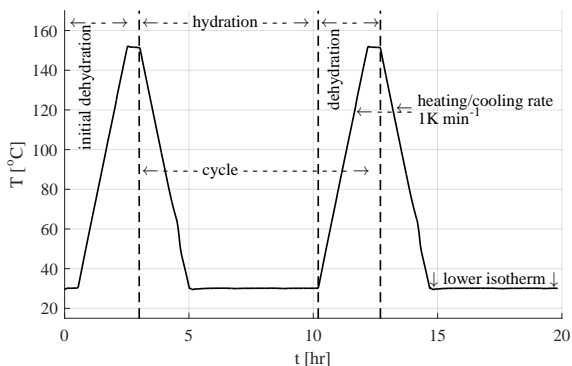
Figure 3.3: Temperature program used in the experiments.

The TG signal shows the weight change of a sample during an experiment, with respect to the initial mass, as measured with the balance. The temperature of each crucible is measured with a thermocouple attached at the bottom of each platform on which the respective crucible is situated. The temperature difference between the sample crucible and the neighbouring reference crucible is recorded. The temperature difference serves as a measure for the heat flux towards or from the sample. The DSC signal is a measure for the heat flow to or from the sample:

negative values indicate exothermic reactions, positive values indicate endothermic reactions; the direction of exothermic values is indicated on the respective axis. Generally, hydration and thus mass gain, implies an exothermic reaction, whereas dehydration implies an endothermic reaction.

The aerodynamic drag and buoyancy forces also affect the TG signal. As the temperature in the furnace changes, the density of the air changes, thus affecting the buoyancy and drag forces acting on the crucibles and crucible holder, resulting a change in the measured weight. Temperature change in the furnace can also affect the DSC signal. As the two crucibles are not located at the exact same place, the temperature change at the two locations can be sensed slightly different, which leads to a false DSC reading. However, these effects are reproducible in different experiments, therefore they can be cancelled out by conducting a so-called empty cup run. In an empty cup run, both crucibles are empty and are subjected to the exact same conditions (temperature program and humidity) as the original sample measurement. Then as a post processing step, the empty run signals are subtracted from the original sample run signals. In addition, empty runs are also used to estimate the measurement uncertainties.

Experiments are conducted under an air atmosphere with a vapor pressure of $1.3 kPa$ and flow rate of $100 ml/min$. The temperature program used in the experiments is shown in Figure 3.3, and some definitions are introduced. The initial heating is implemented for the sample to completely dehydrate and reach anhydrous state at a maximum temperature of $150^o C$.

3.4 Data post processing

In order to evaluate the performance of the materials, TG and DSC signals can be converted to performance indication factors, such as loading (or state of hydration), conversion, conversion rate, and reaction enthalpy. For instance, TG and DSC signals for an endothermic dehydration process are as shown in Figure 3.4. The TG signal shows the mass at each time (m), which drops from the initial mass (m_i) to the final value (m_f). The DSC signal shows the power with which the heat is adsorbed by the sample, which is positive for endothermic reactions. In theory, the baseline (BL) should have a value of approximately zero. The deviation of the DSC signal from the baseline indicates the occurrence of a chemical process, involving thermal effects.
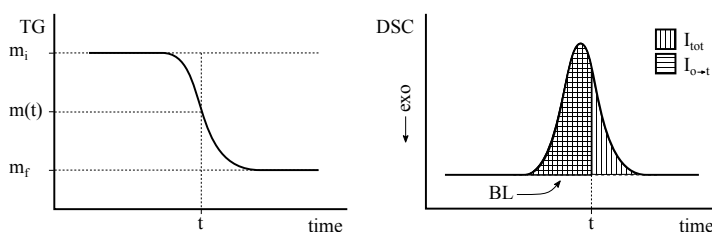
Figure 3.4: A typical TG and DSC signals obtained by the STA apparatus.

The sample mass, used in the figures and tables, represents the mass of the active material in a sample (the calcium chloride content). The salt content of the impregnated material are determined by weighing the samples before and after the impregnation. For encapsulated material, it is determined to be 80% by the ratio of active to passive material (4:1) used in the synthesis process. In addition, the salt content of each sample can be determined by the experimental results, by comparing the calculated equilibrium loading based on measurements and the theoretical equilibrium loading from Figure 3.1. This method gives results that are accurate with in one percent. The loading L, or state of hydration, is the mole of water N_{H_2O} per number of calcium chloride N_{CaCl_2} crystal units, and can be calculated by:

$$L = \frac{N_{H_2O}}{N_{CaCl_2}} = \frac{m_{H_2O} M_{CaCl_2}}{M_{H_2O} m_{CaCl_2}} \tag{3.1}$$

where m_{H_2O} is the mass increase of the sample from anhydrous state due to the absorption of water, and m_{CaCl_2} is the mass of anhydrous salt and only considers the active material in the sample (calcium chloride salt content); and M_{H_2O} and M_{CaCl_2} are the molar mass of water and calcium chloride, respectively. The anhydrous state is recognized when the TG signal is more or less constant in time at high temperatures. In addition, under the conditions applied during the experiments, the loading eventually exceeds hexahydrous state. Apparent loading would therefore be a more suitable term to be used instead of loading.

An important parameter in the material investigation is the conversion α. The conversion ranges between 0 and 1 and is used to describe the progress of a reaction. Conversion can be calculated based on the measured sample mass via TG:

$$\alpha_{TG}(t) = \frac{TG(t) - TG(t_i)}{TG(t_f) - TG(t_i)} = \frac{m - m_i}{m_f - m_i} \tag{3.2}$$

where m is the mass of the sample at a certain moment in time t, and m_i and m_f are the initial mass and the final mass of the sample, respectively. Conversion can be also calculated based on the measured energy change of the sample via DSC:

$$\alpha_{DSC}(t) = \frac{\int_{t_i}^{t}[DSC(t) - BL(t)]dt}{\int_{t_f}^{t}[DSC(t) - BL(t)]dt} = \frac{I_{0 \to t}}{I_{tot}} \tag{3.3}$$

where $I_{0 \to t}$ is the integrated area under the DSC signal curve from the beginning to the time t, and I_{tot} is the total integrated area under the DSC signal curve (as shown in Figure 3.4). In this work, the conversion of hydration reaction is calculated based on the TG signal α_{TG}, which can also be presented based on loading as:

$$\alpha = L/L_f \tag{3.4}$$

where L is the loading at a certain moment in time and L_f is the final loading value.

Based on the assumption that the hydration reactions can be described by a linear driving force (LDF) model, the rate of conversion ($d\alpha/dt$) can be written as:

$$\frac{d\alpha}{dt} = k_{LDF}\gamma \tag{3.5}$$

where k_{LDF} is the kinetics coefficient in $[s^{-1}]$, and γ is the linear driving force, which can be written in dimensionless form as:

$$\gamma = \frac{L_{eq}(t) - L(t)}{L_f} \tag{3.6}$$

where L_{eq} is the equilibrium loading at each time (derived from the equilibrium line as presented in Figure 3.1).

The enthalpy of reaction is determined through the energy change during a reaction. The stoichiometry of the reaction itself is identified through the mass change, used to calculate the change of state of hydration. Host materials are assumed to be inert to water vapor and not to participate in hydration reactions. The reaction enthalpy is the energy released per mole of $CaCl_2$ and can be obtained by:

$$\Delta h = \frac{\Delta H}{N_{CaCl_2}} \tag{3.7}$$

where ΔH is the released heat, as measured in the STA apparatus, which can be calculated by integrating the heat flow over the course of a reaction, according to:

$$\Delta H = \int_{t_i}^{t_f} [DSC(t) - BL(t)]dt = \int_{t_i}^{t_f} \dot{Q}dt \tag{3.8}$$

3.5 Results and discussions

Different samples are compared in terms of kinetics, energy density and stability. These criteria are investigated through the water adsorption and energy exchange of the materials during the re/de-hydration reaction, which are measured by the TGA and DSC methods. A typical experimental result is shown in Figure 3.5 as a function of time and temperature. A de/re-hydration of a $7mg$ encapsulated $CaCl_2$ sample subjected to a water vapor pressure of $1.3kPa$ is shown versus time and temperature. The temperature program starts from the temperature of the high temperature isotherm (150^oC), decreases at a rate of $1^oC/min$ and finally stabilizes at the temperature of the low temperature isotherm (20^oC in this case). As can be seen in Figure 3.5b, hydration starts at a temperature of around 80^oC and continues during the temperature decrease and the low temperature isotherm. During hydration, an almost stable state at the temperature around 40^oC can be
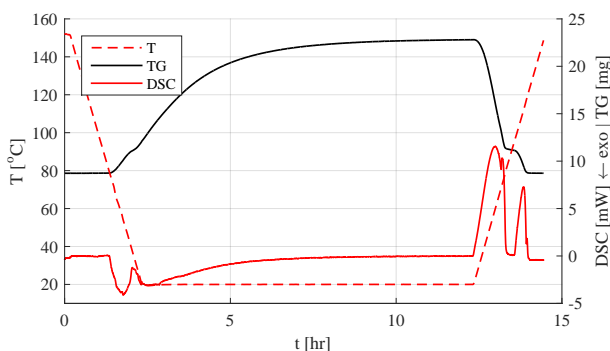
(a) vs. time
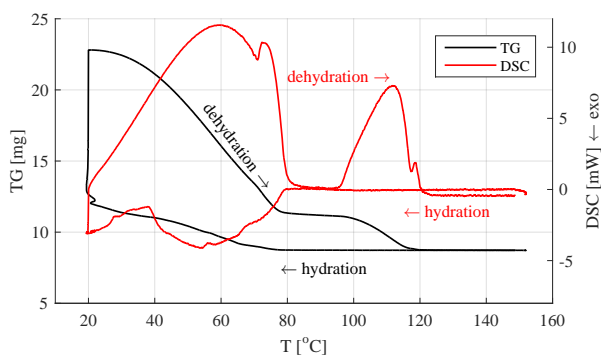
(b) vs. temperature

Figure 3.5: Typical result of de/re-hydration of a $7mg$ encapsulated $CaCl_2$ sample subjected to $1.3kPa$ water vapor pressure.

seen in both TG and DSC signals. It is recognizable in the TG signal as a semistable step at around 40^oC, and in the DSC signal it appears like a peak (it is a dip in energy release toward $0mW$) at around 40^oC. This semi-stable state is calculated to be almost $CaCl_2.2H_2O$. The hydration reaction continues also during the isotherm, till finally, the state of loading in the sample reaches the final value of $12.3 mol H_2O/mol CaCl_2$ and the energy release (DSC signal) reaches $0mW$. The dehydration reaction is much faster than the hydration reaction. The dehydration reaction starts when temperature starts to increase. The mass of the sample

decreases because of the water desorption from the sample. The mass reaches to a stable state after the temperature rises above 80^oC and continues till around 105^oC. This stable state is calculated to be $CaCl_2.2H_2O$. The dehydration continues after the temperature increases above 100^oC till 120^oC.

Similar experiments are performed on different samples from the four materials mentioned in Table 3.2. The experimental results are post processed and employed to evaluate the performance of the material in respect to the reaction kinetics, heat storage density and stability.

3.5.1 Kinetics

Kinetics characteristics of the rehydration reaction for the four materials are expressed in terms of conversion and conversion rate. The conversion of samples upon hydration is calculated based on the apparent loading by Equation 3.4. The data concerns the second rehydration in the experiments, since it is established that the material's behavior changes during the first cycle, which therefore is not representative [44].

Figure 3.6 shows the water loading and the absolute mass of water as a function of time for hydration of several samples with different sizes. As can be seen, the conversion rate decreases as the sample mass increases. This implies that the sample weight affects the conversion rate. Therefore, samples with similar masses should be used, in order to compare the kinetics of different materials. This suggests that the hydration reaction is a diffusion-limited process. The ratio between diffusion and intrinsic reaction rate, expressed as the Damköhler number Da [59], is expected to decrease as sample size decreases. Therefore, small samples are the best representation of the actual hydration reactions. Specially, since the TG signal from the STA apparatus is accurate enough, smaller samples are favourable for the kinetics study. However, the accuracy in the determination of the enthalpy of reaction for the energy density study (based on the DSC signal) might be critical.

In addition, the effect of the sample mass on the conversion rate can also be caused by the limited moisture flow towards the samples. Since a large sample simply takes up more water, it can lead to a slower water uptake relative to the sample mass. In order to check that, a test is done with a large sample of encapsulated calcium chloride material with a sample mass of $15mg$ at different flow rates of 100, 200 and $300ml/min$. It is observed that by increasing the air flow rate, the reaction rate is increased by about 10 to 20%. It suggest that the moisture supply has an effect, but still is not the main limitation factor limiting the reaction progress.

In spite of the different conversion rates, all the samples reach the same loading (around 12.3 mole of water per mole of salt) after a long enough period of time (depending on the sample size). This is an apparent loading, since the sample is in solution and it is not a crystal any more. In the subsequent analysis, conversion rates of the materials are calculated, based on the measured masses during the first three hours of the rehydration reaction, and are compared. Dur-
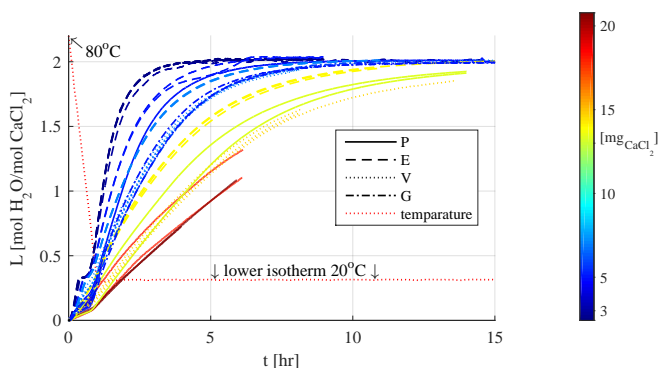
(a) relative mass and loading of water
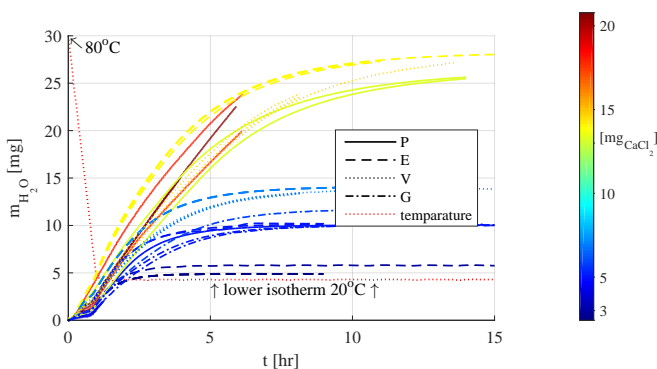
(b) absolute mass change rate

Figure 3.6: Water loading and absolute mass change vs. time for a range of sample sizes (shown with the color bar at the right side); with the vapor pressure of $1.3kPa$ and lower temperature isotherm of 20^oC.

ing this period, the materials reach at least the tetrahydrous state, depending on the sample mass. The impregnated materials are compared to both pure and encapsulated salt.

Figure 3.7 shows the conversion rate vs. time and loading for the impregnated graphite in comparison with the pure and encapsulated calcium chloride. For impregnated graphite, the conversion rate as a function of time is similar to that of pure salt. In terms of vapor diffusion, the host structure does not enhance the
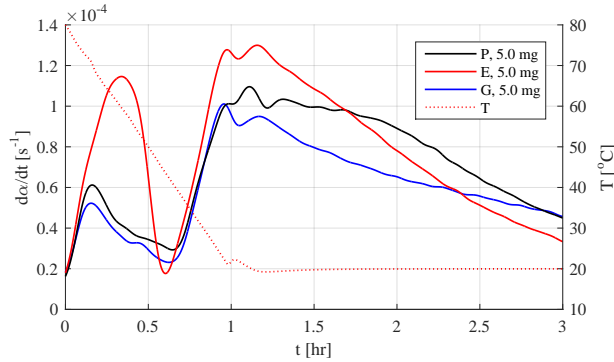
(a) vs. time
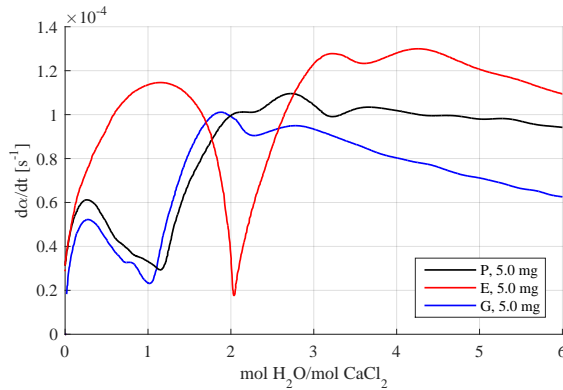
(b) vs. loading

Figure 3.7: Conversion rate of impregnated graphite in comparison with pure and encapsulated calcium chloride; for vapor pressure of $1.3 kPa$ and lower isotherms temperature of $20^o C$.

material's characteristics, for small samples. A dip is visible at the loading of $2 mol_{H_2O}/mol_{CaCl_2}$ in case of encapsulated material, while for the other two it is at around $1 mol_{H_2O}/mol_{CaCl_2}$. But in all the cases these dips happen at almost the same time (around 0.6 hours) and temperature (about $40^o C$). This can be caused by the temperature program, and the fact that temperature decreases during the first one hour. This effect will be discussed further later in this section.

Figure 3.8 shows the conversion rate vs. the time and loading of the impreg-

nated vermiculite in comparison with the pure and encapsulated calcium chloride. Because of the higher sample masses compared to the previous set of experiments, the dips are less pronounced. The impregnated vermiculite sample shows conversion rates in between values for pure and encapsulated materials during the initial stage of the process. Therefore, vermiculite seems to slightly improve the diffusive properties of the material. In general, the encapsulated material shows the fastest rehydration among all the materials. However, it should be noted that the grain size of the encapsulated material is much smaller than the one of pure calcium chloride.

Part of the hydration process takes place under non-isothermal conditions, which means that the equilibrium loading alters over time until the lower isotherm is reached. The hydration of calcium chloride under $1.3kPa$ initiates as the temperature falls below 80^oC (see Figure 3.5). The equilibrium loading at a vapor pressure of $1.3kPa$ as a function of temperature is shown in Figure 3.1. The lower isotherms during the experiments are 20^oC and 30^oC, so the equilibrium loading changes between the start of the reaction and the moment at which the lower isotherm is reached. In order to see the effect, the driving force is calculated based on Equation 3.6 and compared with the conversion rate. Figure 3.9 shows the conversion rate (left axis) and the driving force γ (right axis) as a function of loading for different sample masses of the encapsulated material. As can be seen, the conversion rate shows a strong dependency on sample size. For lighter samples, the conversion rate in general is higher and the shape of the conversion rate is more pronounced than for heavier samples. Smaller samples show a more pronounced profile for the conversion rate as a function of hydration state. In addition, a distinct dip is observed at the dihydrous state ($CaCl_2.2H_2O$), despite the positive driving force. However, the driving force for the small samples is low, which leads to a slower reaction. For the large sample with a sample size of $14mg$, the reaction rate is almost constant. This is caused by the diffusion limitation. From a hydration state around 3 to 4, the conversion rate has reached a maximum and decreases slightly with increasing hydration.

The kinetics coefficient k_{LDF} can be calculated by Equation 3.5. The kinetics coefficient is shown in Figure 3.10 as a function of loading and sample mass for pure and encapsulated samples. It is concluded that the linear driving force model can not adequately describe the reaction kinetics in details for small samples, because the kinetics coefficient is varying with loading. Specially, at the beginning of the process, where the temperature decreases. The largest values for the kinetics coefficient can be found in this segment, which can be caused by a higher activity because of higher temperature. The maximums for the kinetics coefficient of the samples of the pure material happen at lower loadings (Figure 3.10a) compared to the encapsulated material (Figure 3.10b). During the isotherm segment, a more or less constant kinetics coefficient can be seen for both the materials.

The average conversion rates and kinetics coefficients are evaluated and compared in Figure 3.11 for the pure and encapsulated materials and lower isotherm temperature of 20 and 30^oC. There is a general decreasing trend with increasing
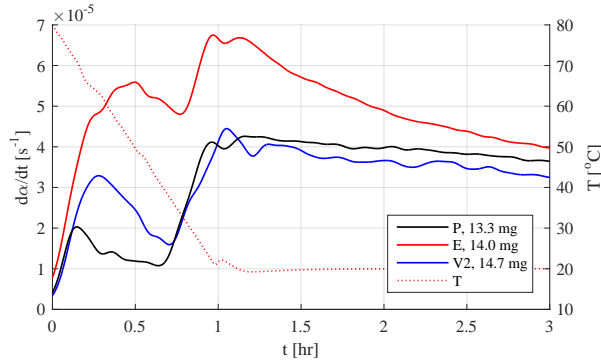
(a) vs. time
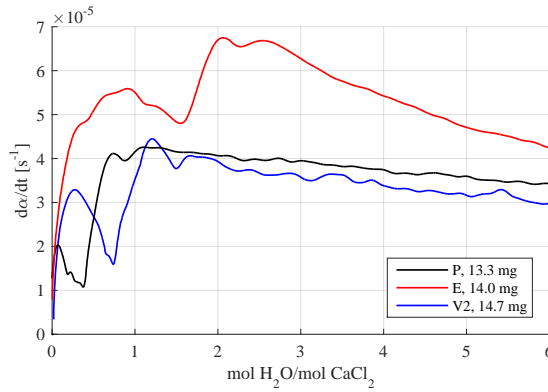
(b) vs. loading

Figure 3.8: Conversion rate of impregnated vermiculite in comparison with pure and encapsulated calcium chloride; for vapor pressure of $1.3kPa$ and lower isotherms temperature of 20^oC.

sample mass for both conversion rate and kinetics coefficient. The conversion rate and kinetics coefficient for encapsulated material are slightly higher compared to the ones for pure material with the same sizes. The average kinetics coefficients are in the order of $10^{-3}s^{-1}$ and $10^{-4}s^{-1}$ for small and large sample sizes, respectively. As presented in chapter 2, this parameter for zeolite is around $10^{-2}s^{-1}$.
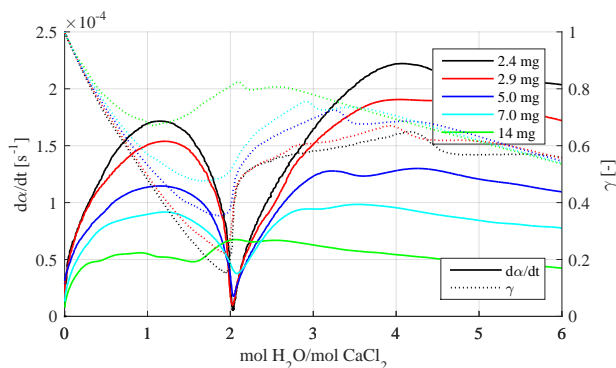
Figure 3.9: The conversion rate as a function of loading for encapsulated calcium chloride samples with different masses (solid lines), and the presumed reaction driving force as a function of material loading (dotted lines); the vapor pressure is $1.3 kPa$ and the lower isotherm temperature is 20^oC.

3.5.2 Energy storage density

The energy storage density is studied for the four calcium chloride-based materials. The energy release of samples during the hydration from anhydrous to hexahydrous state is determined. The simultaneous thermal analysis method allows the estimation of the energy per mole of calcium chloride and per mole of absorbed water. Storage density values are compared to literature values. The measured thermal power from all samples is integrated over time, from the loading of 0 to 6. The released energy is calculated by integration of the thermal power over time between the DSC signal curve and the baseline in the domain where loading (L) is between 0 and 6 $[mol_{H_2O}/mol_{CaCl_2}]$, which is shown as the red shaded area in Figure 3.12.

In Figure 3.13, the enthalpy of the hydration reaction from anhydrous to hexahydrous state is shown for samples of the materials with different masses. The calculated enthalpies seem independent of the sample mass. The energy densities per kilogram and cubic meter of material are summarized in Table 3.3. The energy densities are based on gross material mass (not the salt content). The material densities, which are used in order to calculate the energy densities, are small scale sample densities from Table 3.2. As expected, the pure material has the highest energy density, because of the highest salt content. The energy density of impregnated vermiculite is the highest among the composite materials. The energy density of the encapsulated material is the lowest. The gravimetric energy density of the encapsulated material is 80% of the pure material, which is the same as the salt content weight percentage of the encapsulated material.

Enthalpies of different steps of the hydration reaction per mole of adsorbed
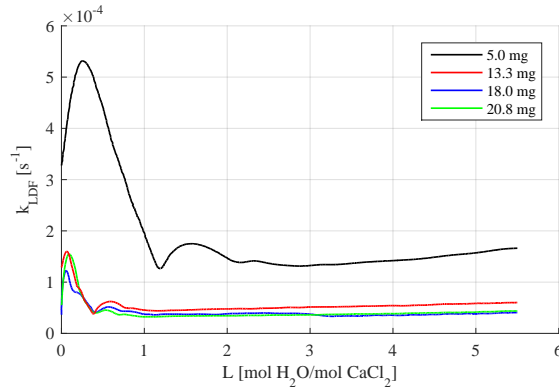
(a) pure material
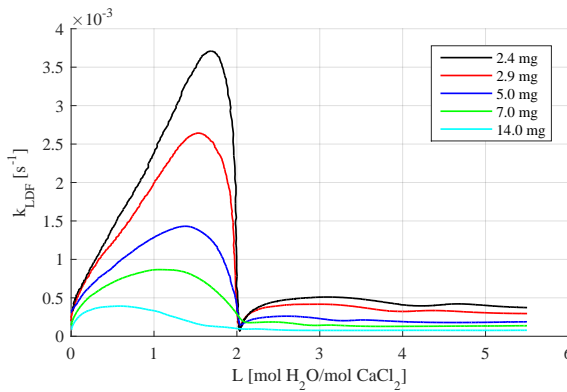
(b) encapsulated material

Figure 3.10: Linear driving force coefficient k_{LDF} for pure and encapsulated materials for a range of sample size (shown with the color bar at the right side); for vapor pressure of $1.3 kPa$ and lower isotherms temperature of $20^o C$.

water are shown in Figure 3.14, for samples of the pure and encapsulated materials. The experimental values are generally lower than the literature values. The discrepancy is in the order of 15 to 30 %. The only value which is not underestimated, is the heat release between monohydrous and dihydrous state.

The measured values show a general underestimation compared to the literature value. The cause for the underestimation can be explained in various ways. As discussed before, it is found that the hydration of the investigated materials is
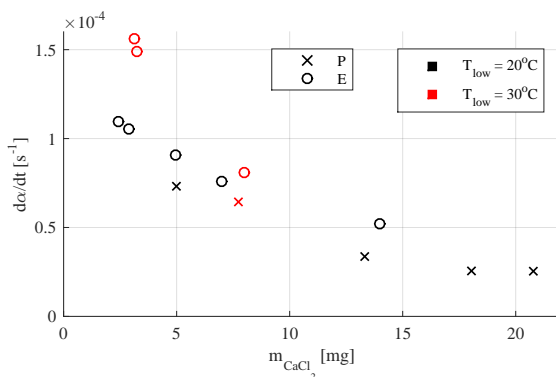
(a)
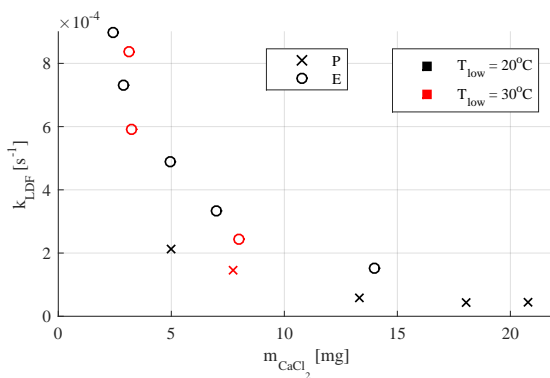
(b)

Figure 3.11: The average value of $d\alpha/dt$ and k_{LDF} as a function of sample mass, in the domain where loading (L) is between 0 and 6 $[mol_{H_2O}/mol_{CaCl_2}]$.

a non-uniform process over the whole sample. Since the thermocouple is located at the bottom of the crucible containing the sample, it senses the temperature of the the bottom part of the sample more than the temperature at the top, because of poor conductivity. In other words, the part of the released heat from the reaction occurring at the top of the sample is less effectively transferred to the bottom of the crucible (near the thermocouple) compared to the reaction occurring at the bottom of the sample. This phenomena is more pronounced in samples with poor conductivity compared to the metallic calibrants. Moreover, because of the larger
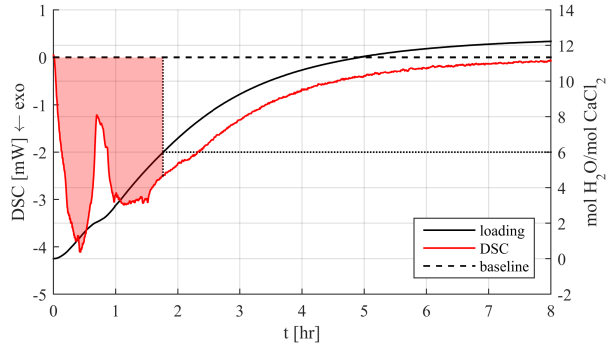
Figure 3.12: Loading and DSC signal measured for an encapsulated calcium chloride sample; the red shade illustrate the integration of release thermal power from the sample over time, which results the released energy from the loading of 0 to 6.
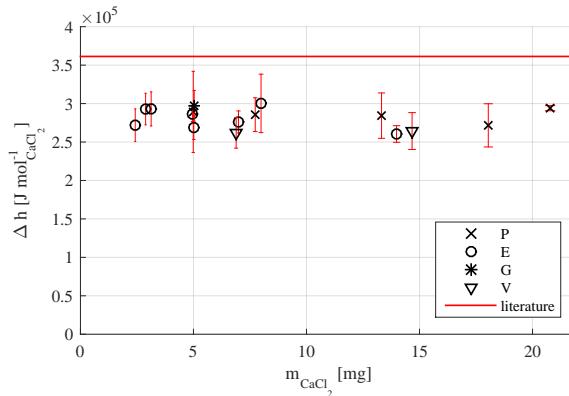
Figure 3.13: Energy densities of the hydration reaction from anhydrous to hexahydrous state for samples of the materials with different masses.

density of metallic calibrants, the volume for the calibration samples is smaller than for the salt samples. In addition, the process of melting and solidification of the calibration samples is much quicker than the hydration of salts (a few minutes versus time spans in the order of ten hours). All these effects result in a larger heat loss to the flow in the furnace compared to the heat flux sensed at the bottom of the crucible with the thermocouple.

Another reason for the underestimation in the measured enthalpies can be
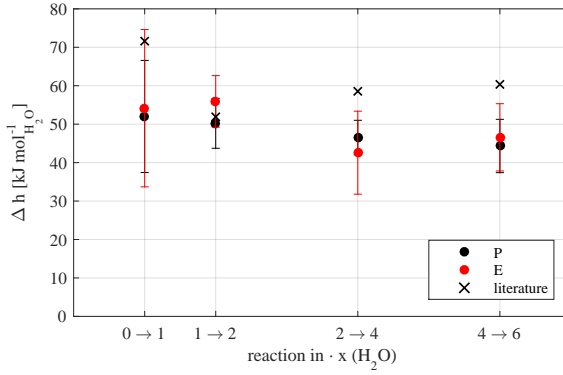
Figure 3.14: Enthalpies of hydration reaction for different state of hydration for samples of the pure and encapsulated materials.

material	$\Delta h[kJ/mol_{CaCl_2}]$	$\Delta h[MJ/kg_{material}]$	$\Delta h[GJ/m^3]$
P	290 ± 50	2.6 ± 0.5	1.7 ± 0.5
G	300 ± 20	2.0 ± 0.2	0.6 ± 0.1
V1	260 ± 20	1.6 ± 0.2	0.5 ± 0.1
V2	260 ± 25	2.0 ± 0.2	1.2 ± 0.1
E	290 ± 40	2.1 ± 0.4	0.4 ± 0.1

Table 3.3: Energy storage densities per mole of salt content, and per mass and volume unit of sample for different materials; under the water vapor pressure of $1.3kPa$ and the low temperature isotherm of 20^oC.

the differences in heat transfer-related properties between the investigated samples and the employed calibrants. The samples used for calibration of the setup are made of Gallium, Indium, Tin, Bismuth and Zink. The investigated samples mainly consist of a salt, having a typical thermal conductivity in the order of $1[W/m.K]$[60], whereas the calibration materials, which are metals, have conductivities in the order of 40 to $80[W/m.K]$. The dimensionless Biot number ($Bi = hl/k$) is a suitable parameter to evaluate the temperature distribution in a physical object having a characteristic length l and heat conductivity k that exchanges heat with a fluid flow with a convective heat transfer coefficient h. A low Biot number indicates a fast distribution of heat inside the object, while a low Biot number is an indication for non-uniform temperature distribution in the object. A comparison is made between the Biot number for a typical calibrant and a typical TCM sample. Assuming the same convective heat transfer coefficient for spherical samples with similar masses, the Biot number for the calibrant is then in the order of hundred times larger than the one calculated for the TCM sample.

Therefore, a more elaborate study on the sensitivity of the apparatus to the conductivity of the calibrant is advised. Also, more detailed knowledge about the thermal processes inside the furnace or around the sample would provide useful insight and will help defining future experiments. Furthermore, non-uniformity of hydration states throughout the sample leads to an inaccuracy in the enthalpy measurement. Therefore, smaller sample size should lead to a higher accuracy. However, using smaller sample sizes lead to a smaller energy release which will be harder to measure.

3.5.3 Stability

Stability of the materials is investigated, based on STA experiments and microscopic observations. Multi-cycle STA experiments have been conducted on the pure and encapsulated salts. The released heat during hydration between anhydrous and hexahydrous state as a function of cycle number is shown in Figure 3.15. The released heat does not vary significantly over ten to eleven cycles, apart from slight random fluctuations. For the pure material, the second and third cycle are missing, because the hexahydrous state was not reached.
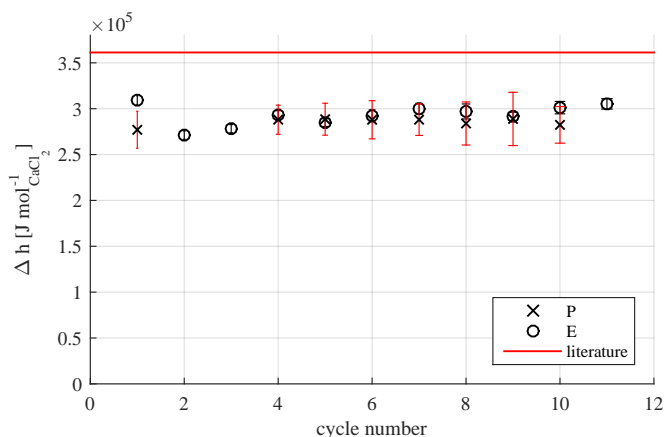
Figure 3.15: Measured storage capacity upon hydration from anhydrous to hexahydrous state over multiple cycle numbers; lower temperature isotherm is $30^{o}C$ and the vapor pressure is $1.3kPa$.

To show the behavior of samples hydrating under high humidity and subsequently dehydrating, photographs from the samples are taken during the de/rehydration process. A qualitative description of the phenomena, occurring under extreme humid conditions, can be seen in the pictures. Exact physical conditions are not recorded. First, the fresh samples are placed on a glass plate and exposed

to humid environment (approximately $2kPa$ at 20^oC) in order to hydrate them. After this period of hydration, the samples are exposed to dry environment (approximately $0.5kPa$ at 80^oC) in order to dehydrate them. Then, the samples are rehydrated again under the same condition as the first hydration. The hydration process under the stated conditions takes a day, and the dehydration process is finished within two hours.

The pictures of hydration, subsequent dehydration of the pure salt sample are shown in Figure 3.16a. During the first hydration of the pure salt sample with granular powder form, the grain structure is lost and the resulting solution droplets allow the material to coalesce and form a bigger droplet. Dehydration of this droplet results in the formation of an agglomerated piece of dry salt. The resulting agglomerated salt shows different kinetics features than the salt in initial granular form. This effect is discussed later in this section.

The pictures of hydration, subsequent dehydration and subsequent rehydration of the impregnated graphite sample are shown in Figure 3.16b. The impregnated expanded graphite first shows overhydration of the contained salt. This is seen by the change in color of the top of the sample. The fresh sample contains relatively dry calcium chloride, which appears as white spots. Deliquescence of the salt results in formation of transparent solution and allows it to flow out of the sample, a process also referred to as washing out. Subsequent dehydration of the sample leads to a structure which is similar to the dehydrated pure salt. However the structure of the graphite host matrix in the middle (probably with a part of salt content still inside) is left intact but softer, as it is vulnerable to mechanical force. After dehydration, the sample appears to be whiter than it was initially, before hydration. This means that salt has escaped from inside the graphite to the surface. The washing out effect of salt from the host matrix is an undesired process, which cannot be observed in the STA experiments, since the sample is contained in a cup, retaining all the original material.

The pictures of hydration, subsequent dehydration and subsequent rehydration of the impregnated vermiculite sample are shown in Figure 3.16c. A similar process is observed for the impregnated vermiculite sample as the impregnated graphite sample. Additionally, the structure of the vermiculite host matrix is distorted after hydration and a paste-like mixture is formed.

The pictures of hydration and subsequent dehydration of the encapsulated salt sample are shown in Figure 3.17. The top row shows the fresh sample as taken from the storage container (left) and the sample after being exposed to humid conditions for approximately one day (right). The sample seems to be expanded after hydration. This process is however poorly visible in the two stills, taken at the beginning and end of the process. In the right picture, a yellow line was drawn along the circumference of the fresh sample on the left and copied to the hydrated sample on the right in an attempt to visualize the expansion. The bottom row shows the glass plate after wiping the hydrated encapsulated material off the glass. A few drops of liquid were still attached to the glass and the glass was then exposed to a temperature around 80^oC. The remaining of salt can be recognized as small white spots on the glass. The encapsulated material also

(a) pure

(b) impregnated graphite

(c) impregnated vermiculite
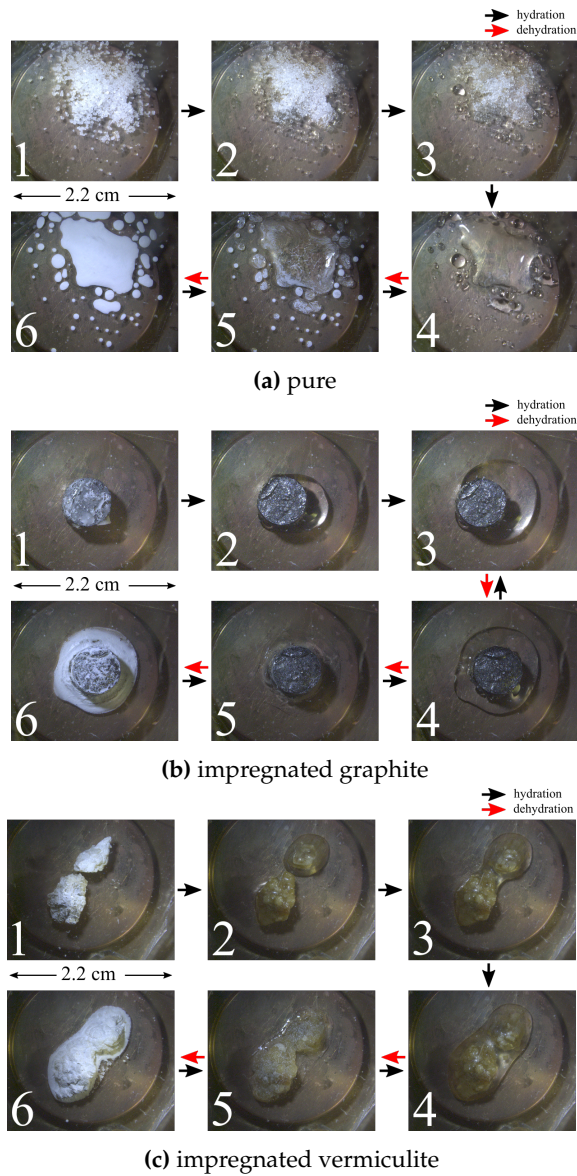
Figure 3.16: Hydration, subsequent dehydration and subsequent rehydration of pure and impregnated materials; during hydration (frames 1 to 4), the sample is exposed to a vapor pressure of roughly around $2kPa$; during dehydration (frames 4 to 6), the sample is exposed to a temperature of around $80^{o}C$ and a vapor pressure of roughly around $0.5kPa$; during rehydration (frames 6 to 4) the same condition as the first hydration is applied again.

shows washing out of material, but to a smaller extent than the impregnated materials. In terms of stability, the encapsulated material shows the best properties.
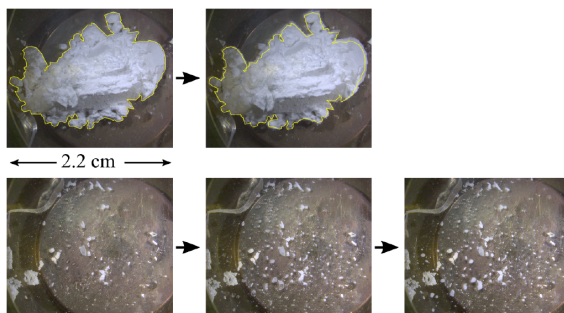
Figure 3.17: The top row shows the fresh sample as taken from its storage container (left) and the sample after being exposed to humid conditions for approximately one day (right). The bottom row of pictures show the remaining of the sample after most of it has been wiped off the glass.

The agglomeration effect of the pure salt can be also detected in STA experiments. This effect in pure salt is compared with encapsulated salt and shown in Figure 3.18. The samples are inserted in the set-up in granular form. After initial dehydration, all samples are hydrated to values beyond the hexahydrous state, which implies that deliquescence has occurred. Presumed agglomeration of the resulting solution in the crucible would lead to dehydration into a cake-like structure, as is observed in the pictures in Figure 3.16a. During the first hour of hydration of the pure salt sample, a clear decline is observed in the conversion rate between first and second cycle. In the first cycle, the sample still has its granular form, however, in the second cycle it has agglomerated. From the second cycle onwards, material behavior is well reproducible. For the case of encapsulated material, it can be seen that the agglomeration is avoided, as the first and second cycles are exactly similar.

Only during the first minutes of the experiments, the conversion rate has similar values for both the first and second cycle: a steep increase is observed. It is expected that this is caused by reactions on the material's surface. The total surface of the grains is bigger and can therefore prolong the steep increase of the conversion rate. After one hour of hydration, the conversion rates for both first and second cycle take on similar values. An explanation is that the outer layer of the grains reaches a higher state of hydration in an early stage, a process expected as a result of the non-uniformity of the process. The hydrated outer layers consequently may agglomerate and thereby obstruct the diffusion of water further into the material, and the process becomes limited by diffusion of water molecules into the salt.
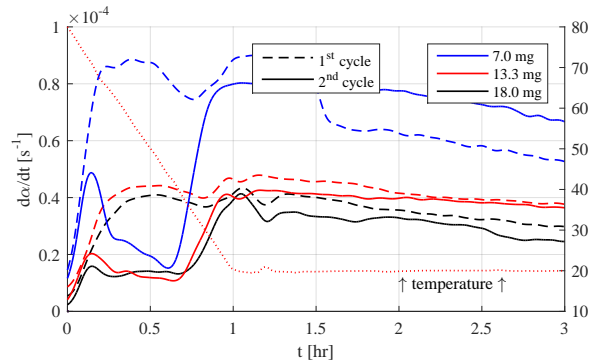
(a) pure
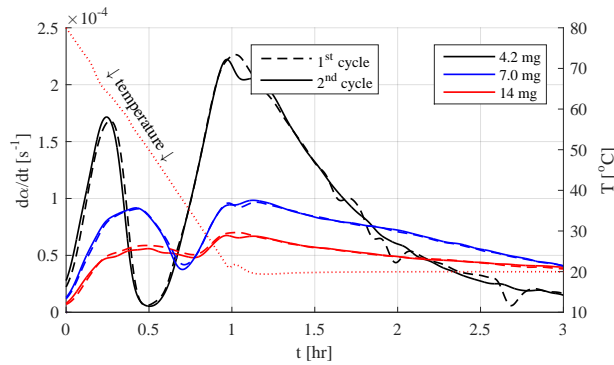
(b) encapsulated

Figure 3.18: First and second cycles of hydration of pure and encapsulated materials.

3.6 Conclusions

Attempts have been made to stabilize calcium chloride by impregnation in expanded natural graphite and in vermiculite, and by encapsulation with ethyl cellulose. The impregnation leads to $73wt\%$ and 87% salt content for once and twice impregnated graphite. Salt content of $68wt\%$ and $86wt\%$ is achieved in the once and twice impregnated vermiculite. The salt content in the encapsulated material is $80wt\%$. Characterization of the calcium chloride-based thermochemical materials is carried out on the basis of three subjects: reaction kinetics, heat storage

density and stability. In general, a strong relation between conversion rate and sample mass is observed. This suggests that the hydration reaction of calcium chloride is a diffusion-limited process.

The hydration reaction rate for impregnated materials is similar to that of pure salt. However, the impregnated vermiculite sample shows conversion rates in between the values for pure and encapsulated materials during the beginning of the hydration process. Therefore, vermiculite slightly improves the diffusive properties of the material. However, the encapsulated material shows the fastest rehydration among all the materials. The average kinetics coefficient of the hydration reaction is calculated for the pure and encapsulated materials based on the LDF model. The kinetics coefficient shows dependency on the sample mass, however the dependency is smaller for large samples. The average kinetics coefficient is roughly in the order of $10^{-3}s^{-1}$ and $10^{-4}s^{-1}$ for small (about $2mg$) and large (about $20mg$) sample masses, respectively. In general, it seems that the kinetics of the hydration reaction of the calcium chloride based materials can be expressed by the LDF model, only for large samples (larger than $10mg$).

The energy storage density is studied for the four calcium chloride-based materials. The energy density is calculated based on the enthalpy of hydration reaction for each material being dehydrated in temperature of 150^oC and being hydrated in vapor pressure of $1.3kPa$ and temperature of 20^oC. The calculated enthalpies per mole of material seem unaffected by the sample mass. The energy density of the encapsulated material is the lowest (about $0.4GJ/m^3$) among all the composite materials. The gravimetric energy density (MJ of energy stored in kg of material) of the encapsulated material is $80wt\%$ of the pure material, which is the same as the salt content percentage of the encapsulated material. The energy densities of once and twice impregnated vermiculite materials are about $0.5GJ/m^3$ and $1.2GJ/m^3$, respectively. The energy density of once impregnated graphite material is about $0.6GJ/m^3$. The energy density of the twice impregnated graphite material is not measured experimentally, but it is expected to be the highest among all the materials (roughly around $1.5GJ/m^3$).

Stability of the materials is investigated, based on STA experiments and microscopic pictures. Multi-cycle STA experiments have been conducted on the pure and encapsulated salts. The released heat does not vary significantly over ten to eleven cycles, apart from slight random fluctuations.The pictures of hydration and subsequent dehydration of the pure salt sample show that the grain structure is lost and a solution is formed on hydration (for vapor pressure in the order of $2kPa$ and temperature about 20^oC). Dehydration of this solution (for vapor pressure in the order of $0.5kPa$ and temperature about 80^oC) results in the formation of an agglomerated piece of dry salt. The impregnated samples show overhydration of the contained salt. Deliquescence of the salt results in the formation of a transparent solution, allowing it to be washed out of the sample. Subsequent dehydration of the sample leads to a structure which is similar to the dehydrated pure salt. However, the structure of the graphite host matrix (probably with a part of the salt content still inside) is left intact. After dehydration, the impregnated graphite sample appears to be whiter than it was initially, before

hydration. This means that salt has escaped from inside the graphite to the surface. The structure of the vermiculite host matrix is distorted after hydration and a paste-like mixture is formed. The encapsulated material looks stable during the hydration process, but seems to be expanded after hydration. However, a few drops of washed out liquid were still visible at the surface of the sample.

A method is developed to evaluate the agglomeration effect in STA experiments by comparing the first and second cycles. The samples are inserted in the setup in granular form. After initial dehydration, all samples are hydrated to values beyond the hexahydrous state, which implies that deliquescence has occurred. During the subsequent dehydration, agglomeration of the solution in the crucible is expected, which will lead to form a cake-like structure. During the first hour of the second hydration of the pure salt, a clear difference is observed in the conversion rate between first and second cycle. In the first cycle, the sample still has its granular form. However, in the second cycle it has agglomerated, causing a reduction of the conversion rate. From the second cycle onwards, material behavior is well reproducible. Only for the case of encapsulated material, it can be seen that the agglomeration is avoided, as the first and second cycles are exactly similar. Therefore, it seems that the agglomeration is avoided in the encapsulated material.

Within the boundary conditions for thermochemical energy storage as presented here, microencapsulated calcium chloride showed high multicyclic stability, while the pure and impregnated materials lose their porosity on overhydration, due to washing out of the calcium chloride under the given conditions. The microencapsulated material remains stable over multiple cycles and at the same time shows the fastest kinetics. However, the disadvantage of the currently used encapsulation method is the resulting low energy storage density. Future work regarding material development should be directed to improve the energy storage density, while maintaining the positive characteristics (stability and fast reaction kinetics).

In this chapter, specific attention has been given to the stability of the material, and attempts have been made to improve this stability, and the effect of these stabilization methods on the performance of the material, such as kinetics and energy density, have been investigated. In the next chapters, the focus will be on reactor or system performance. In these chapters, zeolite 13XBF is used as TCM, because of its well-known properties and high stability.

4

REACTOR DESIGN

4.1 Introduction

For better understanding of the influence of transport phenomena on the performance of the thermochemical heat storage reactor, a detailed model, which considers radial terms as well as axial terms, is needed. It is concluded from chapter 2 that the reactor wall plays an important role in the radial effects occurring in the reactor, and accordingly in the thermal performance of the reactor. This may be caused by a combination of three different effects:

- Heat loss to the ambient causes a lower temperature near the wall, which is directly correlated to the heat transfer coefficient at the inside wall of the reactor and the thermal mass of the reactor wall.

- In the region near the wall, a higher porosity is observed in the bed, because of the interaction of the particles with the rigid wall, since the spatial distribution of the particles must conform to the shape of the wall. The higher porosity near the wall causes a higher local superficial velocity (called wall channelling), hence the produced heat by the reaction is depleted faster in this region. In addition, the higher porosity near the wall results in less material near the wall, thus less reaction heat and a lower temperature as a result.

- Since the state of charge is a function of temperature and partial vapor pressure, the lower temperature near the wall during dehydration (due to heat loss) leads to a lower initial state of charge near the wall for the subsequent hydration.

An extensive investigation on the water vapor adsorption into zeolite 13X in an open system has been done by *Mette et al. (2014)*[23], and a 2D numerical model has been developed. In their work, the higher velocity in the near-wall region is implemented by using the extended Brinkman model developed by *Vortmeyer and Schuster (1983)*[61]. The radial heat and mass dispersion coefficients are estimated based on the so-called Λ_r-model developed by *Winterberg and Tsotas (2000)*[62]. In these models, an effective viscosity, introduced by *Giese et al. (1998)*[63], is employed for the wall region, which is exponentially dependent on the particle Reynolds number in the bed. However, the effect of reactor diameter (or the Reynolds number) is not considered in this correlation.

The purpose of this chapter is to understand the significance of the above mentioned effects on the thermal performance of a thermochemical heat storage packed bed reactor. First, a literature survey is done on the different models expressing the transport phenomena in the packed bed, and the best representative model is chosen. Then, the model is validated by experimental results measured in the lab-scale reactor setup by comparing the pressure drop over the bed, velocity profile below the bed and temperature profile inside the bed. In addition, the profile of adsorbed water concentration in zeolite is compared with experimental results measured by MRI. Next, an investigation on a thermochemical heat storage reactor is done with the validated numerical model. From this work, predictions of the dynamic thermal performance of an adsorption bed on reactor scale is achieved, which is used for further studies on the design and optimization of a thermochemical heat storage system. Suggestions are given in order to optimize the charging and discharging process times, hence, to improve the performance of the reactor.

4.2 Fluid Flow in Packed Bed

Packed bed reactors belong to the most widely applied reactor types, originating from their effectiveness in terms of performance as well as low capital and operating costs. Because of their popularity, the modeling of flow through porous media attracts the interest of engineers and researchers alike due to the complexity of the modeling involved. However, the modeling can be considerably simplified if one is to consider a homogeneous porous medium where the possible porosity does not vary significantly and a uniform flow distribution within the bed can be assumed. In this case, flow through packed beds can be modeled by analogy with flow in pipes when the bed porosity is uniform and low (below 0.65[64]). The pressure drop through packed beds is the result of frictional losses characterized by the linear dependence upon the flow velocity (Darcy term) and inertia characterized by the quadratic dependence upon the flow velocity (Forchheimer term). Adding these two contributions results in the well-known Ergun equation[65]:

$$-\frac{\partial p}{\partial z} = \alpha \frac{(1-\epsilon_b)^2}{\epsilon_b^3} \frac{\mu}{d_p^2} u + \beta \frac{(1-\epsilon_b)}{\epsilon_b^3} \frac{\rho}{d_p} u^2 \qquad (4.1)$$

where p is the pressure, z the axial coordinate, ϵ the porosity, μ the viscosity, d_p the particle diameter, ρ the density and u the velocity. The two first terms on the right-hand side, respectively known as Darcy and Forchheimer term, describe the pressure loss caused by the particles. *Ergun* determined the constants α and β to be 150 and 1.75 for the viscous term (often referred to as Blake-Kozeny-Carman constant) and the inertial term (often referred to as Burke-Plummer constant), respectively. The use of the simple semi-empirical Ergun equation is now generally accepted as a satisfactory prediction of pressure drop in packed beds. However, this is true for infinitely extended packed beds composed of particles that do not differ much in shape from that of spheres[66]. Corrections considering the effect of wall, bed porosity and particle shape can be applied by modifying the constants in the Ergun equation. Some of the studies on the modified Ergun equation are presented in Table 4.1. In the pressure drop relations, the average porosity ($\bar{\epsilon}$) is used. Some of the relations for average porosity are presented in Table 4.2.

#	α	β
1	150	1.75
2	150	$\left[\frac{1.5}{(D/d_p)^2} + 0.88\right]^{-2}$
3	$154\left[1 + \frac{2}{3(D/d_p)(1-\bar{\epsilon})}\right]^2$	$\left[1 + \frac{2}{3(D/d_p)(1-\bar{\epsilon})}\right]\left[\frac{1.15}{(D/d_p)^2} + 0.87\right]^{-2}$
4	$\frac{1000a}{M^2}(D/d_p)^{0.2}\frac{1}{1-\bar{\epsilon}}$	$\frac{12a}{M}(D/d_p)^{0.2}$
5	$\left[185 + 17\frac{\bar{\epsilon}}{1-\bar{\epsilon}}\left(\frac{D}{D-d_p}\right)^2\right]\frac{1}{M^2}$	$\left[1.3\left(\frac{1-\bar{\epsilon}}{\bar{\epsilon}}\right)^{1/3} + 0.03\left(\frac{D}{D-d_p}\right)^2\right]\frac{1}{M}$
M	$1 + \frac{2d_p}{3(1-\bar{\epsilon})D}$	modification factor
a	0.05 or 0.061	for loose or dense packing

Table 4.1: Formulas proposed for evaluating the constants of the Ergun equation; #1 *Mehta and Hawley (1969)*[67]; #2 *Reichelt (1972)*[68]; #3 *Eisfeld and Schnitzlein (2001)*[69]; #4 *Mntillet and Comiti (2007)*[70]; #5 *Cheng (2011)*[71].

#	Equation
1	$\bar{\epsilon} = 0.4 + 0.05(D/d_p)^{-1} + 0.412(D/d_p)^{-2}$
2	$\bar{\epsilon} = 0.373 + 0.917 exp\left(-0.824(D/d_p)\right)$

Table 4.2: Formulas proposed for evaluating the average porosity in packed bed; #1 *Dixon (1988)*[72]; #2 *Ribeiro et al. (2010)*[73].

Existence of an annular wall zone, where the average porosity is larger than in the core of the bed, forms flow channelling in this region. The influence of the wall becomes more significant as the reactor-to-particle diameter ratio D/d_p decreases. In order to take the near-wall flow channelling into account, a radial distribution of the porosity $\epsilon(r)$ can be used. A typical profile for packed beds consisting of particles with small deviations from spherical shape can be approx-

#	μ_{eff}/μ_g
1	$1 + 2.5(1 - \epsilon)$
2	1
3	$2.0 exp(3.5 \times 10^{-3} Re_p)$
4	$1 + (7 \times 10^{-6} \frac{D}{d_p} + 2 \times 10^{-5}) Re_p^2$

Table 4.3: Formulas proposed for evaluating the effective viscosity; #1 *Einstein (1906)*[74]; #2 *Brinkman (1949)*[75]; #3 *Giese et al. (1998)*[63]; #4 *Bey and Eigenberger (1997)*[76].

imated by the following exponential expression after *Giese (1998)*[77]:

$$\epsilon(r) = \epsilon_c \left(1 + 1.36 exp \left[-5\frac{R - r}{d_p} \right] \right) \qquad (4.2)$$

where ϵ_c is the porosity at the core of the reactor (far enough from the wall region), r the radial coordinate, R the radius of the bed. The wall region can provide conflicting effects on pressure loss because, on the one hand, the increase in void fraction leads to a reduction in bed resistance to the flow, whereas, on the other, wall friction itself leads to an increase in resistance. *Cohen and Metzner (1981)*[78] highlighted the twofold nature of the wall effect for the first time and have given a qualitative explanation by developing a model which distinguishes the fluid flow in the near wall region and the core region. This is further developed by *Nield (1983)*[79] by including an intermediate layer between the core and wall region. The model is further generalized by *DiFelice and Gibilaro (2004)*[80] for different reactor-to-particle diameter ratios. This type of model can circumvents problems of uncertainties with regard to conditions in the wall region.

The viscous friction at the wall, which increases the pressure drop in the bed, can not be neglected for small D/d_p ratio, due to the fact that the friction surface of the wall increases relative to the total bed surface corresponding to particles. The Darcy-Brinkman-Forchheimer equation, usually used to describe the flow profile within a porous medium bounded by rigid walls, is an extension of Darcy's law by a viscosity term in order to include the viscous forces near the wall; however its validity is restricted to low flow rates. The extended Darcy-Brinkman-Forchheimer equation incorporates the Ergun pressure loss relation as well, to allow for higher flow rates. *Vortmeyer and Schuster (1983)*[61] have quantified the wall effect with incorporating the Brinkman term in the Ergun equation:

$$-\frac{\partial p}{\partial z} = \alpha \frac{(1 - \epsilon)^2}{\epsilon^3} \frac{\mu}{d_p^2} u + \beta \frac{(1 - \epsilon)}{\epsilon^3} \frac{\rho}{d_p} u^2 - \frac{\mu_{eff}}{r} \frac{\partial}{\partial r} \left(r\frac{\partial u(r)}{\partial r} \right) \qquad (4.3)$$

where μ_{eff} is the effective viscosity. The third term in the right-hand side accounts for the pressure loss resulting from viscous friction in near-wall region, known as the Brinkman term. *Giese et al. (1998)*[77] developed an exponential relation between μ_{eff} and Re_p in packed beds of spherical glass particles, by comparing the calculated velocity profile and the measured one using Laser-

Doppler-Velocimetry. *Bey and Eigenberger (1997)*[76] developed a nonlinear relation between μ_{eff} and Re_p and Re in packed beds of spheres, rings and cylinders, by comparing the calculated velocity profile and the measured one by anemometry. The functions for particles with negligible deviation from spherical shape are presented in Table 4.3.

The dynamics of the adsorption process in a packed bed can be reliably predicted by means of a two dimensional model. However, this presupposes the implementation of both the thermal and the flow effect in the model[81]. In this work, the mass and heat transfer transport phenomena are modeled in axial and radial directions, by including the extended Darcy-Brinkman-Forchheimer equation (Equation 4.3) to model the fluid flow in the reactor. Best representing constants (Table 4.2) are obtained by comparing the calculated pressure drop to the experimental results in the results section. The most representative viscosity correlation from the different effective viscosity correlations (Table 4.3) is chosen, by comparing their effects on the velocity profile in the results section.

4.3 Experimental Setups and Techniques

4.3.1 Reactor Setup

The system studied is the reactor setup introduced in section 2.2. A schematic view of the setup and the reactor are shown in Figure 2.1 and Figure 2.2. Spherical beads of zeolite 13XBFK (CWK Chemiewerk Bad Köstritz GmbH) are used, in which the adsorption of water takes place. The properties of the material, characteristics of the reactor, and operational conditions are presented in Table 2.1.

A manometer (Digitron P200UL[82]) with an accuracy of $\pm 1 Pa$ is used to measure the pressure drop for a range of flow rates $(0 - 150 l/min)$ over the bed. The glass spherical particles of $1.5mm$, and two sizes of zeolite particles (with average diameter of $1.6mm$ and $3.0mm$) with small variation from spherical shape are used. A hot wire anemometer (TSI 8386[83]) is used to measure the velocity $15mm$ below the bed, filled with zeolite particles with two different sizes, at different radial positions.

4.3.2 MRI setup

In order to verify the moisture transport model, another setup is used as depicted in Figure 4.1. The moisture content in the reactor is measured as function of time and position using a 1.5T MRI scanner. The reactor has the same dimensions as the reactor used in the reactor setup. The influence of the flow rate and particle diameter (1.6 and $3.0mm$) on the adsorption is studied. The inflow air introduced to the system is subsequently dried and divided into two circuits. The air flow in the wet circuit passes through a temperature-controlled humidifier. The dry and wet circuit mass flow controllers are operated such that a desired humidified flow rate is achieved in steady state, which is verified with the sensor before the packed bed.
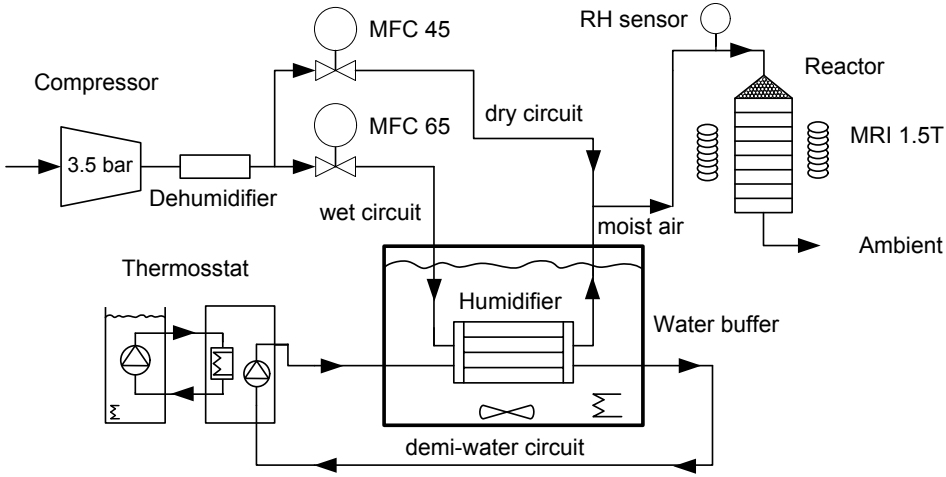
Figure 4.1: Schematic view of the MRI setup.

The applicability of MRI measurement to follow the water density during the sorption/desorption process is previously tested and verified[84]. Magnetic Resonance Imaging (MRI) technique is used for non-destructively and quantitatively measuring proton densities in a sample. The MRI scanner provides an external static magnetic field $\vec{B}_0$ and as a result the nucleus precesses around the axis of the external $\vec{B}_0$ field. The frequency of this precession is directly proportional to the strength of the field given by the Larmor frequency (ω)[85]. For constructing an image, the magnetic field is varied across the object by using a field gradient, so that different spatial locations become associated with different precession frequencies $(\omega = \gamma|\vec{B}_0 + \vec{G}(x, y, z)|)$. In this case a Fast Field Echo (FFE) pulse sequence is used to image the reactor. The intensity–time signal is detected by a coil in the MRI scanner and the signal is subsequently Fourier transformed to the frequency domain. Since frequencies are associates with spatial locations an image can be constructed. When the repetition time T_r is large enough compared to the spin-lattice relaxation time $(T_r > 4T_1)$, the spin-lattice relaxation time T_1 can be ignored[85]. The signal of water attenuates in an MRI experiment according to:

$$S(t_e) = \rho \exp(-t_e/T_2). \tag{4.4}$$

Herein ρ is the hydrogen density, t_e the echo time and T_2 the transversal relaxation time. Hence, it is possible to link the measured signal intensity of the MRI to the water density as the hydrogen density is directly related to the water density. As we used a medical scanner without Faraday coil inside, the coil detunes by variations in water content inside the coil. To counter for this effect, a reference sample is placed next to the sample to minimize the detuning and if necessary correct for signal variations as a result of detuning effects. In addition, signal variations as a result of temperature will be expected to be maximal 10%

according to Curie's law [86], based on a ΔT of $30K$. As a temperature correction is not performed these MRI measurements are semi-quantitative and the signal can slightly vary as a result of temperature variation.

4.4 Numerical Model

4.4.1 Transport Phenomena Equations

The simple reactor model discussed in section 2.4 is an one-dimensional model considering the heat losses from the side wall of the reactor by the heat resistances in radial direction (quasi 2D). In this section a two-dimensional model is developed. The equations which describe the dynamics of the system are formulated under the assumptions that: (a) the adsorbent beads have identical properties; (b) the bed properties are uniform; (c) the gas phase behaves as an ideal gas; (d) the gas and solid phases are in thermal equilibrium. The extended Darcy-Brinkman-Forchheimer equation (Equation 4.3) together with the effective viscosity (from Table 4.3) are used to model the fluid flow in the reactor. The Equation 4.5 and Equation 4.6 present the governing mass and heat balances inside the bed are presented along the vertical coordinate (z), the radial coordinate (r) and the time (t). These two PDEs contain accumulation, convection, radial and axial dispersion, and source terms.

Mass balance for water concentration in the gas phase (c):

$$\epsilon(r)\frac{\partial c}{\partial t} + u(r)\frac{\partial c}{\partial z} - \frac{1}{r}\frac{\partial}{\partial r}\left[rD_r(r)\frac{\partial c}{\partial r}\right] - D_z(r)\frac{\partial^2 c}{\partial z^2} + (1-\epsilon(r))\rho_p\frac{dq}{dt} = 0 \quad (4.5)$$

where D_z and D_r are the axial and radial mass dispersion coefficient, respectively, ρ_p is particle density and q water loading in the solid phase.

Heat balance for temperature of the gas and solid phases (T_b):

$$\overline{\rho C_P}\frac{\partial T_b}{\partial t} + \rho_g C_{P,g}u(r)\frac{\partial T_b}{\partial z} - \frac{1}{r}\frac{\partial}{\partial r}\left[r\Lambda_r(r)\frac{\partial T_b}{\partial r}\right] - \Lambda_z(r)\frac{\partial^2 T_b}{\partial z^2} - (1-\epsilon(r))\rho_p\frac{dq}{dt}\Delta H = 0$$
$$(4.6)$$

where Λ_z and Λ_r are the axial and radial heat dispersion coefficient, respectively. The heat capacity $\overline{\rho C_P}$ used in the accumulation term of the heat balance is the overall volumetric heat capacity for the gas and solid phases and can be estimated by Equation 2.11.

The source terms Equation 4.5 and Equation 4.6 include the reaction rate $\frac{dq}{dt}$ and the reaction enthalpy ΔH, which are evaluated from Equation 2.1 and Equation 2.8, respectively, based on the hydration reaction model of the zeolite material (section 2.3).

The wall temperature (T_w) in each layer is calculated by another PDE for conductive heat transport in a solid wall:

$$\rho_R C_{P,R}\frac{\partial T_R}{\partial t} - \frac{1}{r}\frac{\partial}{\partial r}\left[r\lambda_R\frac{\partial T_R}{\partial r}\right] - \lambda_R\frac{\partial^2 T_R}{\partial z^2} = 0 \quad (4.7)$$

This equation holds for all the layers in the wall, namely Teflon (tef), stainless steel (ss) and insulation (ins). Their characteristics, i.e. the density (ρ_R), heat capacity ($C_{P,R}$) and conductivity (λ_R), differ for each material. Cooling at the external surface of the outer layer (insulation) is calculated with $\dot{Q}_{loss} = h_o(T_R - T_{amb})$, where T_{amb} is the ambient temperature. The external heat transfer coefficient, h_o, can be calculated from a Nusselt number relation at the outside wall of the reactor for natural cooling[87].

4.4.2 Mass and Heat Dispersion Coefficients

In Equation 4.5 and Equation 4.6, the third and fourth terms represent the radial and axial dispersion, respectively. In reaction engineering, the topic of dispersion (longitudinal and lateral) is treated in detail, and it is generally observed that the data for liquid and gases do not overlap, even in the appropriate dimensionless representation . In addition, dispersion coefficients are a function of different parameters such as length and diameter of bed, particle size, and density and viscosity of fluid. Therefore, finding good representative correlations for dispersion coefficients is important. For very low fluid velocities, dispersion is the direct result of molecular diffusion. As the velocity is increased, the contribution of convective dispersion becomes dominant over that of molecular diffusion. It is commonly assumed that the diffusive and convective components of heat and mass dispersion are additive, in both axial and radial direction[40]. In this section, correlations for mass and heat dispersion coefficients in both axial and radial directions are presented.

Axial dispersion
The axial mass dispersion coefficient D_z and axial thermal dispersion coefficient Λ_z can be calculated by[88]:

$$D_z = \delta_{eff} + \frac{Pe_m}{K_z}\delta \tag{4.8}$$

$$\Lambda_z = \lambda_{eff} + \frac{Pe_h}{K_z}\lambda_g \tag{4.9}$$

where Pe_m and Pe_h are the Peclet numbers for mass and heat transfer, respectively:

$$Pe_m = \frac{\overline{u}d_p}{\delta} \tag{4.10}$$

$$Pe_h = \frac{\overline{u}d_p\rho_g C_{P,g}}{\lambda_g} \tag{4.11}$$

The effective diffusion coefficient of the packed bed can modeled by $\delta_{eff} = \delta(1 - \sqrt{1 - \epsilon(r)})$[89]; here δ is the diffusivity. The effective thermal conductivity of the packed bed without fluid flow, λ_{eff}, can be estimated based on the particle thermal conductivity λ_p and gas thermal conductivity λ_g by Equation 2.12.

In Equation 4.8 and Equation 4.9, the value $K_z = 2$ is used [90] and is estimated theoretically from the equivalence of the dispersion model to a CSTR-cascade by *Aris & Amundson (1957)* [91].

Radial dispersion

The radial mass dispersion and thermal dispersion coefficients can be presented as follow:

$$D_r(r) = \delta_{eff} + \frac{Pe_m}{K_{1,m}} \frac{u_c}{\bar{u}} f_m(R-r)\delta \tag{4.12}$$

$$\Lambda_r(r) = \lambda_{eff} + \frac{Pe_h}{K_{1,h}} \frac{u_c}{\bar{u}} f_h(R-r)\lambda \tag{4.13}$$

with

$$f_m(R-r) = \begin{cases} \left(\frac{R-r}{K_{2,m}d_p}\right)^{n_m} & ,0 < R-r \le K_{2,m}d_p \\ 1 & ,K_{2,h}d_p < R-r \le R \end{cases} \tag{4.14}$$

$$f_h(R-r) = \begin{cases} \left(\frac{R-r}{K_{2,h}d_p}\right)^{n_h} & ,0 < R-r \le K_{2,h}d_p \\ 1 & ,K_{2,h}d_p < R-r \le R \end{cases} \tag{4.15}$$

The functions mentioned in Equation 4.12 and Equation 4.13 have been proposed by *Cheng and Vortmeyer (1988)* [92] for fully developed forced convective heat transfer in a packed bed bounded between parallel plates and was experimentally approved by *Vortmeyer & Haidegger (1991)* [93] for both heat and mass transfer in a wall-cooled packed bed reactor in the presence of an exothermic chemical reaction. *Winterberg et al. (2000)* [62] have re-evaluated the functions and determined the parameters (presented in Table 4.4) by comparison of the model to the experimental data available from literature. They interpreted the quantities for the heat transfer case as follows (the parameters for the mass transfer case are analogous): $K_{1,h}$ determines the slope of rise in the effective thermal conductivity with flow velocity; $K_{2,h}$ sets the damping parameter after the coefficient begins to decline towards the wall; the exponent n_h determines the curvature of the damping function.

parameter	mass dispersion	heat dispersion
n	2	2
K_1	$8\left[1 + \frac{3}{Pe_c^{0.5}}\right]$	8
K_2	0.44	$0.44 + 4exp\left(-\frac{Re}{70}\right)$

Table 4.4: parameters of the radial mass and heat dispersion models

The complete model consists of four PDEs:

- Equation 4.5 for modeling the water concentration in the gas phase (c);

- Equation 4.6 for modeling the bed temperature (T_b);

- Equation 4.7 for modeling the wall temperature (T_R);

- Equation 2.1 for modeling the water loading in the solid phase (q).

The mass and heat balances are subjected to the corresponding boundary and initial conditions as follow based on the conditions in the experimental setup.

$$t = 0 \rightarrow T_b = T_{amb}, T_R = T_{amb}, c = 0, q = q_0 \tag{4.16}$$

$$z = 0 \rightarrow T_b = T = T_{in}, \frac{\partial T_R}{\partial z} = 0, c = c_{in}, \frac{\partial q}{\partial z} = 0 \tag{4.17}$$

$$z = H \rightarrow \frac{\partial T_b}{\partial z} = 0, \frac{\partial T_R}{\partial z} = 0, \frac{\partial c}{\partial z} = 0, \frac{\partial q}{\partial z} = 0 \tag{4.18}$$

$$r = 0 \rightarrow \frac{\partial T_b}{\partial r} = 0, \frac{\partial c}{\partial r} = 0, \frac{\partial q}{\partial r} = 0 \tag{4.19}$$

$$r = R \rightarrow T_b = T_R, \frac{\partial c}{\partial r} = 0, \frac{\partial q}{\partial r} = 0 \tag{4.20}$$

The complete model as presented, is developed and solved in COMSOL Multiphysics, which is a Finite Element Method (FEM) based program. The PDEs are discretized in space by Lagrange linear shape functions. Both the bed and wall domains are meshed with a physics-controlled mesh with a extremely-fine element size. The solver is a fully coupled time-dependant solver. A Backward Differentiation Formula (BDF) scheme (maximum order of 5 and a minimum order of 1) with an initial time step of $0.001s$ is used as the time stepping method. The relative, absolute and event tolerances are set to 1E-2.

4.5   Results and Discussion

The complete model as presented, is developed and solved in COMSOL Multiphysics, which is a Finite Element Method (FEM) based program. The PDEs are discretized in space by Lagrange linear shape functions. Both the bed and wall domains are meshed with a physics-controlled mesh with a extremely-fine element size. The solver is a fully coupled time-dependant solver. A Backward Differentiation Formula (BDF) scheme (maximum order of 5 and a minimum order of 1) with an initial time step of $0.001s$ is used as the time stepping method. The relative, absolute and event tolerances are set to 1E-2. The numerical results are compared with experimental results considering the pressure drop over the bed, velocity profile below the bed and temperature profile inside the bed. In addition,the profile of adsorbed water concentration in zeolite is compared with experimental results measured by MRI.

4.5.1 Pressure drop

The pressure drop over the bed of particles in the reactor setup is measured for glass particles of $1.5mm$ diameter and zeolite particles of 1.6 and $3.0mm$ average diameter, for a range of flow rate $0-150 \, l/min$ with increments of 5% (superficial velocity $0-0.65 \, m/s$). The measured pressure drop per unit of reactor length are compared to the one calculated using the relations discussed before.
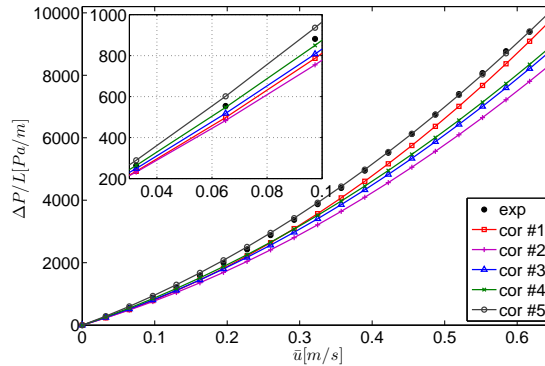
(a) glass particle $d_p = 1.5mm$ (correlations from Table 4.1)
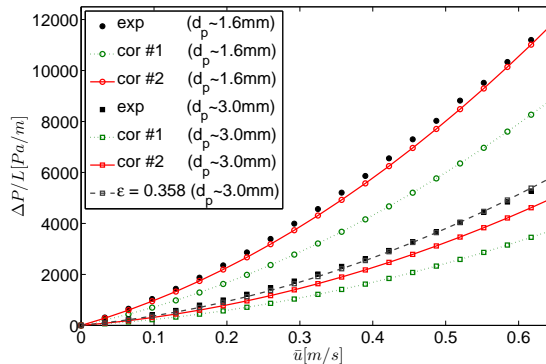
(b) zeolite particle (correlations from Table 4.2)

Figure 4.2: Pressure drop in the bed ($D = 0.07m$) filled with glass particles and two sizes of zeolite particles.

In Figure 4.2a, the pressure drop measured over the bed filled with glass particles is compared with the ones calculated by using different relations for friction factors α and β in the modified Ergun equation. It can be seen that using cor #5 from Table 4.1 (*Cheng (2011)*[71]) gives the best fit, for the whole range of flow rate. The estimated bed porosity is more accurate for the bed filled with glass particles, than for the one filled with zeolite particles, since the range of size distribution is wider for zeolite. The small and big zeolite particles are in a range

71

of $1.4 - 1.8mm$ and $2.5 - 3.5mm$ in diameter, while the glass particles are almost uniform in size. In addition, the lower sphericity of zeolite particles has an effect on both the porosity of the bed and the friction factors (α and β) in the modified Ergun equation. In Figure 4.2b, the effect of the average bed porosity on the calculated pressure drop over the bed is shown. For both small and big zeolite particles, cor # 2 from Table 4.2 (*Ribeiro et al. (2010)*[73]) gives a better estimation than cor # 1 (*Dixon (1988)*[72]). For large zeolite particles, the deviation is larger and a better fit is achieved by $\epsilon = 35.8\%$.

4.5.2   Velocity Profile

Measured radial velocity profiles below the bed filled with small and big zeolite particles for flow rate of 30, 60 and 120 l/min are shown in Figure 4.3. Maldistribution of the flow near the wall can be clearly seen for all the cases. Additionally, wall channelling becomes less pronounced for higher Reynolds numbers. Since the inertial term in the bed overrides the viscous term near the wall and results into more dispersion of momentum, thus the velocity profile becomes smoother. This effect is the same for both sizes of the zeolite particles. However, the peak in the velocity profiles for larger particle size is measured to be at a larger distance from the wall. Furthermore, the velocity peak near the wall is wider and of a smaller magnitude for the larger particle size. That is caused by the fact that the void space near the wall is larger for a pack of larger particles compare to one of small particles.

Different relations for effective viscosity are presented in Table 4.3. The different models for predicting effective viscosity result in a large spread in simulated velocity profile in packed bed. It confirms that the models should not be used outside the range over which they are measured. Therefore, the ones proposed by *Einstein*[74], *Brinkman*[75] and *Givler and Altobelli*[94] are not considered here. In addition, it can be concluded from the velocity profile measurements that the shape of radial profile depends on the Reynolds number (or superficial velocity) and the particle size (Figure 4.3). Therefore, the relation proposed by *Bey and Eigenberger (1997)*[76] gives a more general estimation of effective viscosity in pack bed compared to *Giese et al. (1998)*[63].

In Figure 4.4, the effects of the Reynolds number and particle size on simulated velocity profile are shown over a small region near the wall. Unfortunately, the velocity distribution in the bed itself could not be measured. It should be noted that the modeled velocity peak in the bed occurs in a very narrow region near the wall, while the velocity profiles measured below the bed show wider peaks. That is because the velocity profile changes rapidly from the shape in the bed (simulated velocity profile in the bed) to the shape related to flow in an empty pipe. *Vortmeyer and Schuster (1983)*[61] and *Bey and Eigenberger (1997)*[76] claimed that it is possible to calculate this effect by solving numerically the two-dimensional Navier-Stokes equation for the developing flow inside the empty tube with the artificial flow profiles of the packed bed as inlet condition. Despite the fact that the measured velocity profiles are in the transition state, the effects
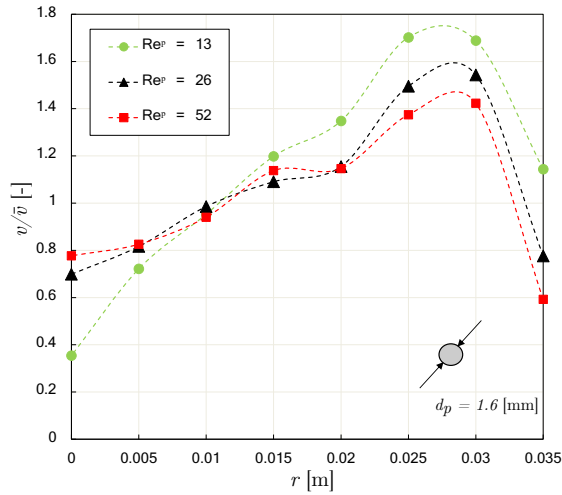
(a) small particle $d_p \approx 1.6mm$
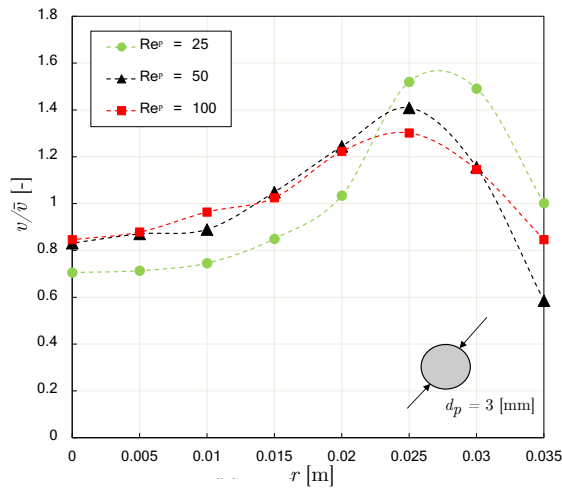
(b) large particle $d_p \approx 3.0mm$

Figure 4.3: Experimental velocity profile below the bed with $D = 0.07m$.

of the Reynolds number and particle size are still clear. These effects are similar between measurements below the bed and simulated velocity profiles, when the relation proposed by *Bey and Eigenberger (1997)*[76] is used for the effective viscosity.
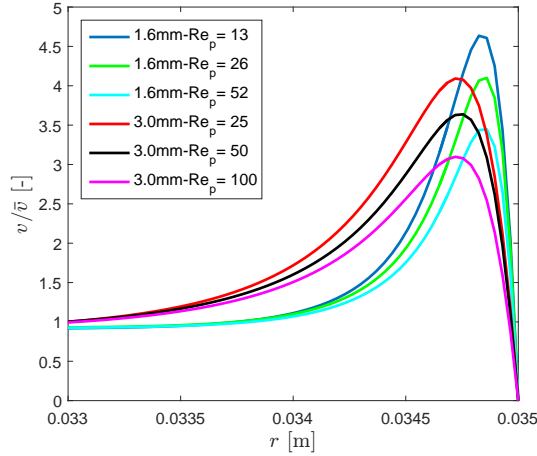
Figure 4.4: Numerical velocity profile in the bed with $D = 0.07m$ for small and large particle sizes, and different flow rates.

4.5.3 Moisture content

The MRI technique is used to investigate the moisture content q, in the zeolite bed. The MRI signal intensity in a cross section at a fixed height of the bed ($L_z = 90mm$) is shown in Figure 4.5a (at $t[s] = [1225, 2042, 2453, 3270, 3755, 4572]$ from top figure to bottom, respectively) and over a longitudinal section at the center of the bed is shown in Figure 4.5b (at $t[s] = [410, 1636, 2864, 4166, 5394, 6622]$ from top figure to bottom, respectively). The moisture content is indicated ranging from blue, low moisture content, to red, high moisture content. The earlier occurrence of the reaction in the wall region compared to the core region is clearly visible in the longitudinal section view. As can be seen also in the cross section view, the higher moisture content happens first in an annular region near the wall, and later in the core region.

The MRI experiment is performed for different flow rates and particle sizes. For each case, the normalized integration of the measured signal intensity over a cross sectional slice located at a fixed height (L_z) during time is calculated. The normalized signal intensity directly represents the total moisture content in the specific slice of the bed. In Figure 4.6, the total adsorbed moisture is shown vs. time $(t - t_0)$, where t_0 is calculated by $t_0 = (L_z/u)(\rho_b \Delta q / c_{in})$. The slope of the curves is an indication of the reaction front sharpness. For example, as an extreme case, if the curve was a step function it means that the reaction front is flat. It is observed that decreasing the flow rate promotes the wall channelling, and for a larger particle size the intensity increases slower compared to a smaller particle size.

The location of adsorbed moisture front can be extracted from the MRI experimental results. From each of the longitudinal section images presented in Fig-

(a)   **(b)**
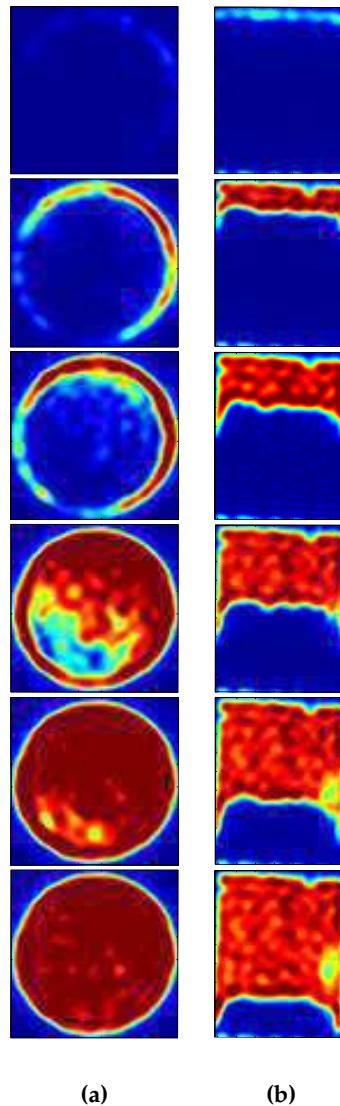
Figure 4.5: Moisture content during hydration time measured by MRI (flow direction from top to bottom of reactor), ranging from blue (low moisture content) to red (high moisture content): (a) Cross section; (b) Longitudinal section.

ure 4.5b, the location of the moisture front is extracted. Figure 4.7 shows the comparison between the extracted front from the MRI measurement and the one calculated by the numerical model. An excellent fit is found by choosing $K_{1,m} = 2$, $K_{2,m} = 0.44$ and $n_m = 2$ for parameters used in Equation 4.12 and Equation 4.14. However, in order to generalize this result measurements on more different con-
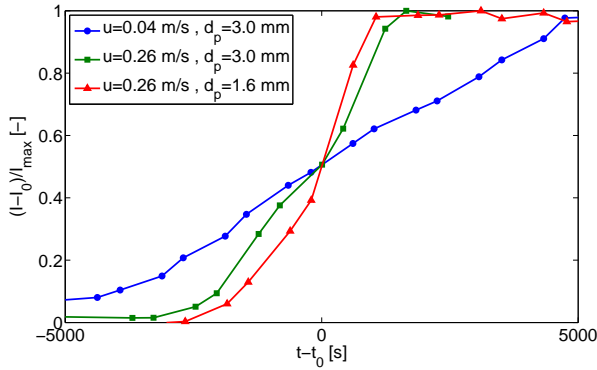
Figure 4.6: Normalized summation of the measured MRI signal intensity (related to the moisture content) in a slice located at a fixed height (L_z) vs. the time ($t - t_0$) in a bed with $D = 0.07m$.
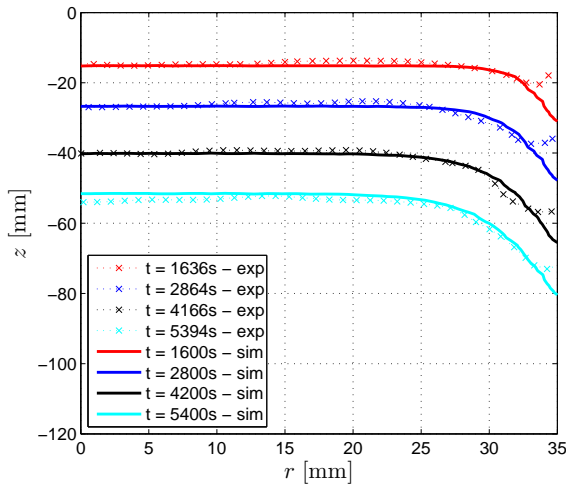
Figure 4.7: Adsorbed moisture front shape at different times during hydration. Flow from top to bottom with $u = 0.26m/s$ and $c_{in} = 0.34mol/m^3$, through zeolite bed with $D = 0.07m$ and $d_p = 1.6mm$.

ditions are needed. The amount of adsorbed water at different heights of the bed over time can also be derived from the cross section images presented in Figure 4.5a. Figure 4.8 shows the comparison between the experimental and numerical concentration of adsorbed water in the solid phase (q). The concentration at each height initially increases slowly due to the peak near the wall and later increases sharply due to the flat core region.
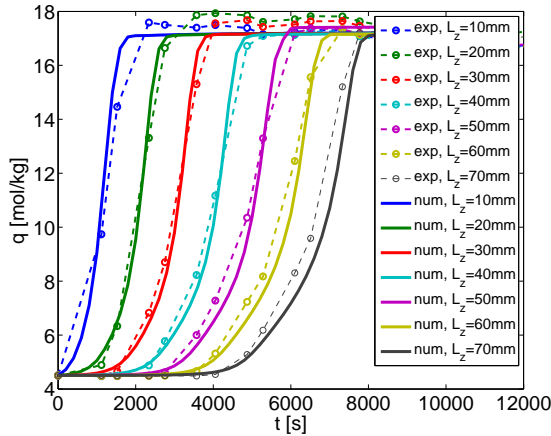
Figure 4.8: Adsorbed water concentration at different heights vs. time during hydration. Flow from top to bottom with $u = 0.26m/s$ and $c_{in} = 0.34mol/m^3$, through zeolite bed with $D = 0.07m$ and $d_p = 1.6mm$.

4.5.4 Hydration

The temperature measured and simulated at the location of M thermocouples at different heights of the bed during hydration of the bed is shown in Figure 4.9. In addition, the concentration of water at the outlet of the reactor is shown in Figure 4.10. The water introduced at the inlet of the reactor is adsorbed during hydration and the temperature increases as a result of released adsorption energy. When the reaction front passes the location of a certain thermocouple and the temperature drops to the temperature of the cold humid inflow air, the material at that location is completely hydrated, hence no further reaction occurs at that specific place in the reactor and no energy is released. The temperature at the outlet stays high till all material has reacted, after which the temperature at the outlet drops and the water concentration increases to the inlet concentration.

If the reaction front is flatter in the radial direction, it will lead to a sharper transition in the temperature and concentration at the outlet of the reactor. In Figure 4.11, the concentration of water in the gas and solid phases, and the temperature of the bed at a specific time (10000s) are shown. The fronts move through the bed and pass the bottom of the bed gradually, starting from the wall region to the core region. When the concentration (c) front passes the bottom, the water concentration of the outflow air start to increase. Conversely, when the temperature (T) front passes the bottom, the temperature of the outflow air start to decrease. The sharpness of this transition depends on the flatness of the fronts. Effects of different considered parameters on the transition are studied.
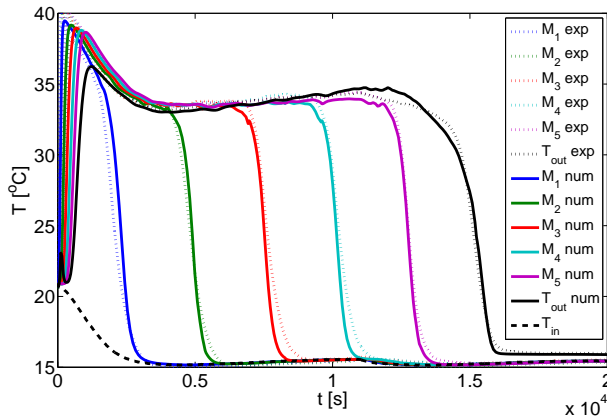
Figure 4.9: Measured and simulated temperature at the location thermocouples $M1 - 5$, T_{in} and T_{out} during hydration.
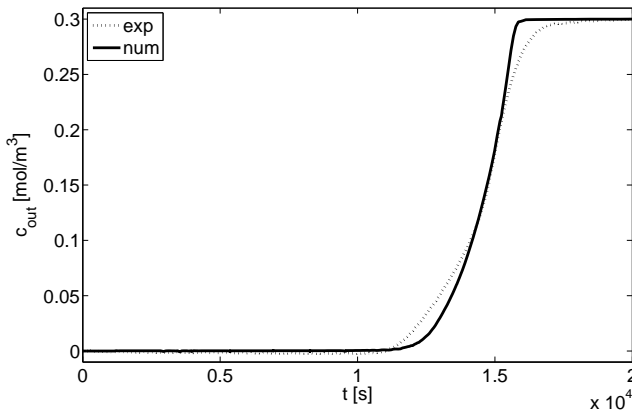
Figure 4.10: Measured and simulated water concentration at the outlet during hydration.

4.5.5 Dehydration

The bed is dehydrated in the reactor setup. The temperature program used for dehydration consists of a ramp from ambient temperature to 180^oC with a heating rate of $0.67^oC/min$, and a isotherm at 180^oC. The measured and simulated water concentration at the reactor outlet during $20000s$ dehydration are shown in Figure 4.12. As can be seen, the comparison between experimental and numerical curves is far from perfect. The experimental result shows a bimodal shape, while the numerical result shows only one peak. The first peak can be caused by escape of loosely bonded water molecules to zeolite at lower temperatures, and the second peak by release of strongly bonded water molecules to zeolite at higher
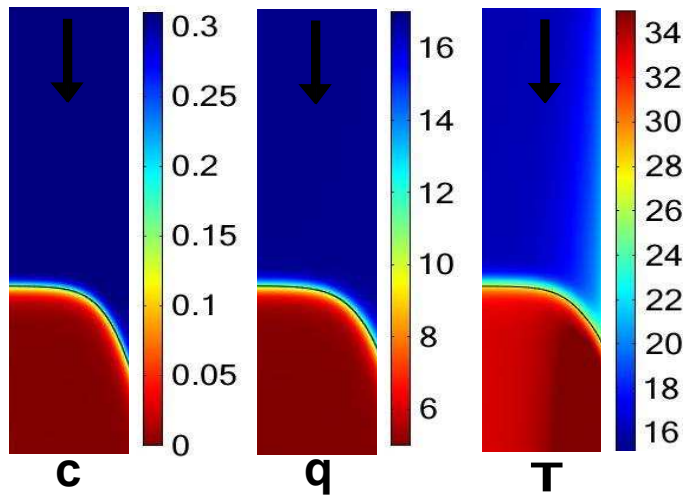
Figure 4.11: Water concentration in the gas phase ($c[mol/m^3]$) and in the solid phase ($q[mol/kg]$), bed temperatures ($T[^oC]$) during hydration with flow from top to bottom.
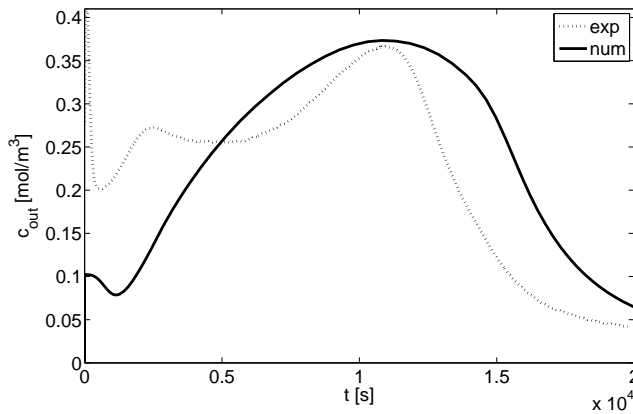
Figure 4.12: Measured and simulated water concentration at the outlet during dehydration.

temperatures. However, this should be investigated by measurements in small scale samples. In spite of different profiles from experiment and simulation, the total amount of desorbed water from the material over time is almost the same. After $20000s$ of dehydration, the total amount of desorbed water calculated from experimental and numerical results is $87.8g$ and $86.5g$, respectively. However,

the amount of desorbed water and the State of Charge (SoC) in the material are dependent on the duration of the charging process.

(a) $t = 16000$ [s]
$\bar{q} = 3.46$ [mol/kg]

(b) $t = 20000$ [s]
$\bar{q} = 1.74$ [mol/kg]

(c) $t = 24000$ [s]
$\bar{q} = 1.09$ [mol/kg]
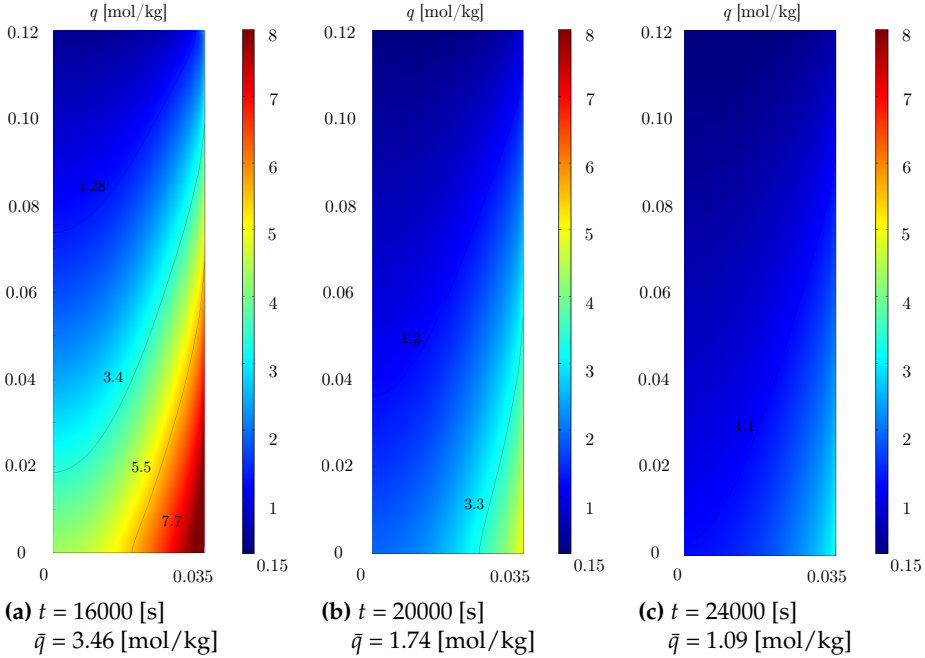
Figure 4.13: Moisture concentration of the zeolite bed q [mol/kg] in the reactor geometry (r,z) [m] at three different times during dehydration. Flow from top to bottom with $u = 0.26m/s$ and $T_{in} = 180^oC$, through zeolite bed with $D = 0.07m$ and $d_p = 3.0mm$.

In Figure 4.13, the SoC in the material as a function of time is shown. The SoC after $16000s$ is still high in the wall region at the bottom of the reactor, while it is getting drier after $20000s$. Finally, after $24000s$, the average water loading in the reactor is around $1.09 mol/kg$. It is almost the highest achievable SoC with this charging temperature (around 180^oC). As can be seen, the improvement in the SoC from $20000s$ to $24000s$ after the start of charging process is minor. Different duration of the charging process leads to a different final SoC for the charging process and, subsequently, a different initial SoC for the succeed discharging process. Therefore, the final state of charge of the zeolite bed as a function of the radial and axial coordinate obtained after a dehydration simulation is used as an initial condition of the subsequent hydration simulation, and contrariwise. It concludes the importance of the durations of the charging and discharging processes. The optimum durations of the charging and discharging processes are studied.

4.6 Parametric study

In the previous section, the model is validated by the results from different experimental techniques performed in the reactor setup with the characteristics presented in Table 2.1. In this section, the validated model is used to study the effects of different parameters on the performance of an up-scaled reactor. A segment of a large scale reactor with a segment volume of about $62.5L$ is defined in the model and a larger air flow rate (compared to the lab-scale case) is applied to get a high heating power in the order of 1 kW, corresponding to a full scale design. The inlet water vapor pressure is set at $13mbar$ and the whole reactor is initially at ambient temperature. The characteristics of this large scale reference case are presented in Table 4.5. In this section, the dimensionless time is used, which is defined as the time divided by the residence time ($\theta = t/\tau$), for dehydration and rehydration processes.

property	value [unit]
Bed height (H)	0.43 [m]
Reactor inner diameter (D)	0.43 [m]
Insulation thickness (t_{ins})	0.03 [m]
Wall thickness (t_{ss})	0.002 [m]
Particle diameter (d_p)	3.0 [mm]
Air flow rate (Q)	0.04 [m^3/s]
Inlet water concentration (c_{in})	0.57 [mol/m^3]
Rehydration temp. ($T_{in,reh}$)	40 [^oC]
Dehydration temp. ($T_{in,deh}$)	180 [^oC]

Table 4.5: Characteristics of the large scale reference case

4.6.1 Radial effects

In this section, the effect of different parameter settings in the model on the reaction front in the reactor are evaluated. The water concentration and temperature at the outlet of the reactor during the discharging process for the different cases are presented in Figure 4.14. Considered Cases are:

- case #0: original model (reference case)

- case #1: flat velocity profile

- case #2: flat initial SoC

- case #3: no heat loss through reactor wall

- case #4: combination of cases #1 and #2

(a) water concentration
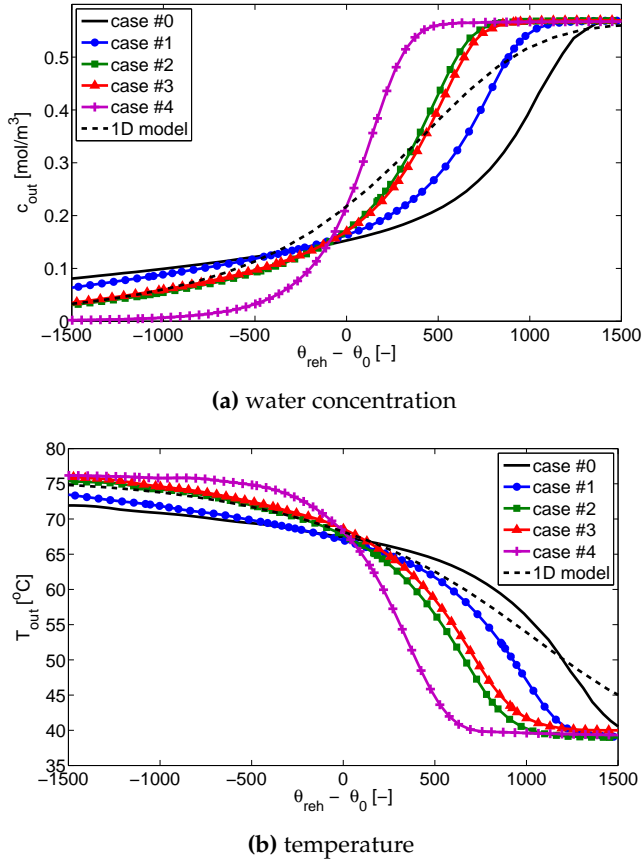
(b) temperature

Figure 4.14: Water concentration and temperature at the outlet of the reactor for the different cases.

By neglecting the radial dependencies of the velocity, initial SoC and porosity (case #4), the transition in the water concentration and temperature at the outlet of the reactor is sharper compared to the reference case (case #0). The cases #1, #2 and #3 show a intermediate transition compared to these two extreme cases. The cases #2 and #3 show a similar trend, which means that the main effect of decreasing the heat losses, is to obtain a flatter SoC during dehydration, and therefore a sharper transition compared to the reference case.

In addition, a comparison is done between the 2D model presented in this chapter and the 1D model (quasi 2D) presented in chapter 2. In the 1D model, the axial mass dispersion coefficient D_z used in the governing mass transfer PDE Equation 2.9 is calculated based on the mass Peclet number calculated based on Gunn's correlation (Equation 2.10). Here, the axial mass dispersion coefficient in the 1D model is changed to get the comparable results with the 2D model. By

comparing the the temperature at the outlet of the reactor during the discharging process for this case, the best representative modified axial dispersion coefficient is found to be 2 times larger than the normal axial dispersion coefficient calculated based on Gunn's correlation. Therefore, the influence of the radial effects presented in this chapter can be simulated by the 1D model using a modified axial mass dispersion coefficient. However, this is dependent on the characteristics of the bed and should be checked for other cases. Further study is needed in order to find a more general correlation for including the radial effects in the modified axial dispersion coefficient. As can be seen in Figure 4.14, for this case, the temperature at the outlet of the reactor can be simulated with a reasonable accuracy by the 1D model with the modified axial dispersion coefficient.

4.6.2 Duration of charging and discharging processes

The effect of the charging and discharging duration on average power (power per flow rate P/ϕ) during discharging and total efficiency ($\eta = \eta_{reh}.\eta_{deh}$) of the reactor are investigated (Figure 4.15). The power, energy and efficiency are calculated as follow:

$$P = \rho_g u A C_p (T_{out} - T_{in}) \tag{4.21}$$

$$E = \int_0^t P dt \tag{4.22}$$

$$\eta = -E_{reh}/E_{deh} \tag{4.23}$$

For $D/H = 1$ and $\tau = 1.56$, increasing the duration of charging process (t_{deh}) from $20000s$ to $30000s$ will increase the power, but the change in power by increasing t_{deh} form $30000s$ to $40000s$ is negligible. However, the efficiency will drop by increasing t_{deh}. The efficiency is generally increasing by increasing the duration of charging process (t_{reh}). However, the change is negligible for t_{reh} larger than $30000s$ ($\theta_{reh} \geq 19230$). For the case $t_{deh} = 30000s$, the maximum power is achieved by t_{reh} being between $30000s$ and $35000s$ ($19230 \geq \theta_{reh} \geq 22440$). The reaction front for this case at different rehydration times is shown in Figure 4.16. The low total efficiency is caused mostly by the heat losses during the dehydration process ($19.76MJ$) compared to the rehydration process ($1.47MJ$), for $t_{deh} = 30000s$ and $t_{reh} = 35000s$. The heat loss mechanisms are conduction through the walls (around 91% and 43% of the heat loss during the dehydration and rehydration processes, respectively) and sensible heat in the material (around 9% and 57% of the heat loss during the dehydration and rehydration processes, respectively).

For $D/H = 1$ and $\tau = 0.31$, both the efficiency and power per volumetric air flow rate are improved. This is caused by the fact that heat losses are less for this case with higher flow rate ($\tau = 0.31$) compared to the case with lower flow rate ($\tau = 1.56$), because the process is faster. The optimum for this case is also occurring for t_{reh} being between $6000s$ and $7000s$ ($19230 \geq \theta_{reh} \geq 22440$). However, the operating flow rates should be chosen based on the charging and
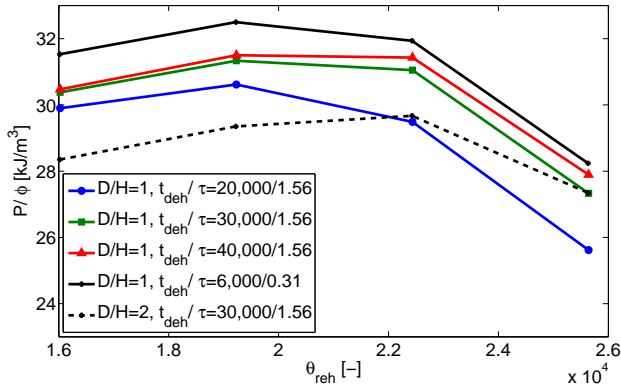
(a) average power per volumetric air flow rate
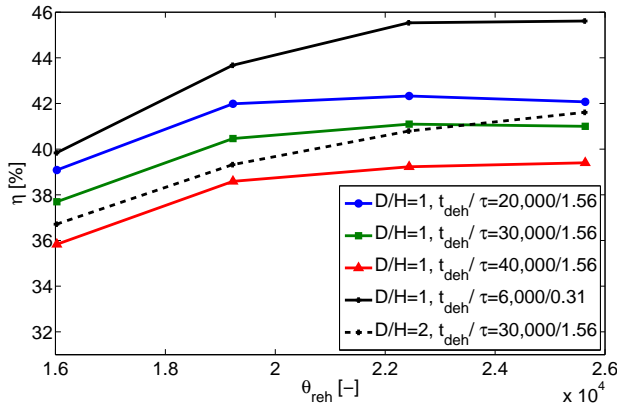
(b) total efficiency

Figure 4.15: Average power and total efficiency of the reactor for different durations of charging and discharging processes.

discharging strategy developed according to the heat supply and demand in the house.

For $D/H = 2$ and $\tau = 1.56$, both the efficiency and power per volumetric air flow rate decline. The efficiency is the highest for $t_{reh} = 40000s$ ($\theta_{reh} = 25640s$), while the power is at the lowest. The optimum power still occurs for t_{reh} being between $30000s$ and $35000s$ ($19230 \geq \theta_{reh} \geq 22440$). However, the reactor aspect ratio should be chosen based on the COP of the reactor, considering the pressure drop over the bed and the required fan power to blow air through the bed.

Considering both power and efficiency, the optimum suggested operating condition is to apply dimensionless duration of charging (θ_{deh}) of around 19230 and and dimensionless duration of discharging (θ_{reh}) between 19230 and 22440. Specifically, for a reactor with a bed volume of about 62.5L and air flow rate of

$0.04m^3/s$ ($\tau = 1.56s$), the optimum durations of charging and discharging processes are around $30,000s$ ($\sim 8.3h$) and $35,000s$ ($\sim 9.7h$), respectively.
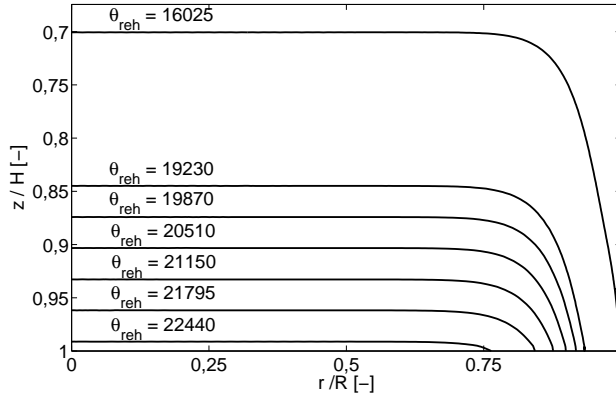
Figure 4.16: Reaction front at different rehydration times for $D/H = 1$ and $t_{deh}/\tau = 30000/1.56$. Flow from top to bottom with $Q = 0.04m^3/s$ and $c_{in} = 0.57mol/m^3$, through zeolite bed with $D = 0.43m$ and $d_p = 3.0mm$.

4.6.3 Aspect ratio

The effect of the reactor aspect ratio on the efficiency and COP of the reactor is studied in this section. Volume of the reactor and air flow rate are $62.5L$ and $0.04m^3/s$, respectively. The optimum durations of charging and discharging processes, concluded from previous section, are used here. The COP of the reactor is calculated as the total energy extracted during rehydration divided by the total required fan energy to blow air through the bed during rehydration and dehydration ($COP = E_{reh}/E_{fan}$). The total required fan energy is calculated as $E_{fan} = Q\Delta P(t_{reh} + t_{deh})/\eta_{fan}$, which is the required energy to overcome the pressure drop over the bed ΔP (estimated by the fluid flow model), for an air flow rate of Q, during rehydration and hydration processes, with a fan with an efficiency of $\eta_{fan} = 50\%$. Figure 4.17 shows the efficiency and COP of the reactor for different aspect ratios. The maximum efficiency of around 41.5% is achieved for the aspect ratio of 1.5, however the change in efficiency for the other aspect ratios (ranging from 0.5 to 3.0) is negligible (ranging from 40.5 to 41.5%). While, as expected, the COP increases continuously by increasing the aspect ratio.

4.7 Conclusions

A literature survey is done in order to find the best model to evaluate pressure drop and velocity profile in a packed bed of porous media, considering the radial effects, specifically the effect of the rigid wall of the reactor. By comparing
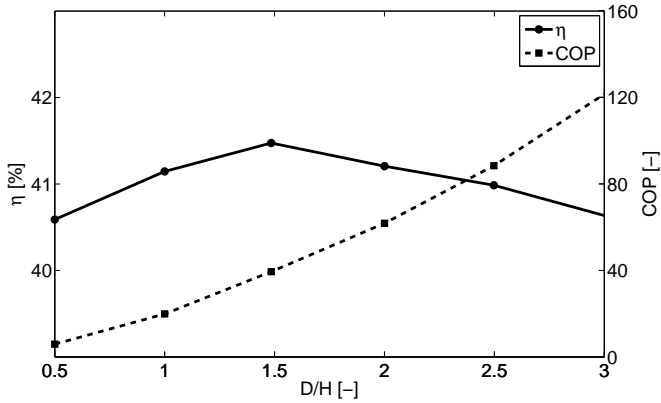
Figure 4.17: Efficiency and COP of the reactor for different reactor aspect ratios, for $Q = 0.04m^3/s$ and $d_p = 3.0mm$.

the measured pressure drop over the bed to the model results, good agreement is found for the Ergun equation with the modified constants presented by *Cheng (2011)*[71]. However, the particle diameter distribution must be taken into account, because a wider deviation from the average diameter results in a lower bed porosity and higher pressure drop. The velocity is measured and wall channelling is observed. An increase in wall channelling was found for low flow rates and smaller particle diameters. The best representative model for this behaviour is found to be the Brinkman extension to the Darcy–Forchheimer equation in combination with an effective viscosity expression by *Bey and Eigenberger (1997)*[76] and radial porosity profile by *Giese (1998)*[77].

A 2D mass and heat transfer model is developed by assuming a homogeneous temperature for the gas and solid phases, and the radial profile of the axial fluid velocity in the bed from the aforementioned velocity model. In addition, the heat transfer in the solid wall of the reactor is modeled and coupled to the bed model at the inside wall boundary. The model is validated using experimental thermal analysis from the reactor setup, and the moisture content results from the MRI setup.

The MRI technique is proven to be an excellent addition to the experimental research into the reactor. The moisture content in a reactor of up to 3 liters can be measured as a function of time with a spatial and time resolution of approximately 2mm and 2min (not simultaneously). The effects of flow rate and particle diameter on the shape of the moisture front is studied and compared to the numerical model for the benchmark case. From this analysis, the optimal value of the mass dispersion parameters presented by *Winterberg et al. (2000)*[62] are determined, and the dependence of the dispersion parameter $K_{1,m}$ on the Peclet number is validated. Further investigation is needed in order to generalize and quantify it for a range of conditions.

Reasonable agreements between the temperatures and concentrations from

the experiment and numerical model during hydration and dehydration are found. Measurements indicated that the influence of the dehydration cycle on the hydration cycle is significant. Therefore, the final state of charge of the zeolite bed as a function of the radial and axial coordinate obtained after dehydration simulation is used as an initial condition of the hydration simulation, and contrariwise. It concludes the importance of the durations of the charging and discharging processes.

Finally, the significance of each considered effect in the model on the performance of the reactor is assessed. An investigation is done on the effect of re/dehydration duration on the average power and total efficiency of the reactor. The optimum suggested operating condition for a reactor with a bed volume of about $62.5L$ and air flow rate of $0.04m^3/s$ ($\tau = 1.56s$) is to apply durations of charging and discharging processes of around $8.3h$ and $9.7h$, respectively. The aspect ratio of 1.5 leads to the highest efficiency in the reactor, however the change in efficiency for the other aspect ratios (ranging from 0.5 to 3.0) is negligible. While, as expected, the COP increases continuously by increasing the aspect ratio. The insight gained in this study on the influence of flow rate and tube-over-particle diameter ratio on the velocity, mass and heat transfer can be used in further studies to design an optimal reactor for a large scale storage system.

5

SYSTEM IMPROVEMENT

5.1 Introduction

The purpose of this chapter is to investigate the thermal performance of a complete thermochemical heat storage system with reference to its application in the built environment. An open system employing the gas-solid reaction of zeolite hydration-dehydration cycle is considered. In such a system, air is usually used as the carrier gas to carry water vapor as the sorbate into the reactor, and to transfer the released heat from the reactor by convection. Since the amount of water vapor in air (or any other gas) is limited by the saturation humidity, the temperature step obtained in the reactor is limited. In order to cover the domestic hot water demand in a house, it is necessary to improve the system to be able to achieve higher temperatures. For this purpose, energy should be recuperated in the system to achieve the required 60^oC for hot tap water, in spite of the limited temperature lift created by the reaction.

The reactor design plays a key role in the performance of a thermochemical heat storage system. The simplest open reactor concept is to pack the thermochemical material in a fixed bed reactor and blow the moist air through the whole bed. This requires to heat up the large thermal mass of the entire bed at once, which causes large thermal inertia in the system and makes the performance of such a system significantly less controllable, and heat losses become large, because the entire amount of storage material has to be heated at once. Therefore, it is important to keep the reaction zone (the part of the material which participates and/or is affected by the reaction) as small as possible. *Mette et al.*[95] realized a system with an external reactor concept which means that the TCM storage reservoir is separated from the reactor. This has the advantage that, at any time, the

amount of material in the reactor is reduced to only a limited small part of the total amount of the material. The disadvantage of this concept is the complexity of the reactor design and the energy needed to transport the material to the reactor. Another method to reduce the reaction zone, which is denoted here as the segmentation concept, is to pack the material in separate reactor segments and to run only one segment at a time. *Weber et al.*[96] realized a solar heating system including a segmented sorption store, to cover the space heating demand of an uninhabited small building with the living space of $43 m^3$. A thermal power output of around 0.6 to $0.8 kW$ is measured during the discharge phase, however the temperature level is below $60^o C$, because it is designed to cover only the space heating demand. The segmentation concept provides the simplicity and the low auxiliary energy need of the packed bed reactor design, and assures at the same time the limited reaction zone requirement. In this way, it is possible to run the segments in sequence with a constant power for providing the required average demand. The produced energy can be stored in a short-term heat storage water tank, and the peak demand can be shaved by the water tank.

As discussed in chapter 4, a disadvantage of the packed bed reactor design is the risk of formation of non-reactive zones, leading to a lower energy storage density. In literature, this problem is tackled with different approaches. In order to avoid the formation of non-reactive zones, *Zettl et al.*[97] realized a system with a rotating reactor of $50 kg$ of zeolite. This method is expensive and requires extra mechanical energy to revolve the reactor. *Johannes et al.*[98] realized a high power system with two packed bed segments, containing $80 kg$ of zeolite in total. A high power of around $2.25 kW$ is reported from their experiments by running the segments in parallel. Although the constant high power is achieved during most of the discharge phase, a considerable amount of energy is still produced during the period at the end of the process with a decaying power. *Michel et al.*[43] developed a large scale prototype using $400 kg$ of $SrBr_2$ salt hydrate packed in eight separate modules on top of each other. Each module has a reactive bed with a thickness of $7.5 cm$ and a diffuser with a thickness of $1.5 cm$. In order to maximize the reactor energy storage density, the number of modules and diffusers should be minimized by using thicker reactive beds. However, a larger thickness limits mass transfer and reduces the thermal power output.

The decaying power output at the end of the discharge process in a packed bed reactor, is caused by a non-flat reaction front in the bed. Based on chapter 4, this uneven progress of the reaction front through the bed is caused by radial effects in the material bed, because of the presence of the reactor wall. For instance, flow channelling happens near the wall because of a higher porosity in the near-wall region compared to the core of the bed. This causes faster propagation of the reaction front in the near-wall region compared to the center of the bed. When the reaction front reaches the bottom of the bed in the near-wall region (but not yet in the core, because of the higher core porosity), the output temperature starts to reduce gradually, until also the core has completely reacted. During this period, which is denoted here as the "tail period", a lower reaction power is produced compared to the average power of the reactor. The energy present in the tail pe-

riod of the discharge phase cannot be utilized because of the lower power, which leads to a lower energy storage density of the system. However, it would be possible to recover this amount of energy and increase the energy storage density by developing innovative strategies.

In this chapter, a system setup is designed, constructed and tested to produce hot tap water. With implementing recuperation in the system, in order to preheat the inflow air, the required domestic hot tap water temperature is achieved. In addition, for better understanding of the thermal performance of the complete thermochemical heat storage system a numerical model is developed and validated with the experimental results. The model is used to establish an energy map for an up-scaled system. The segmentation concept is suggested to reduce the size of the reaction zone, in order to improve the system performance. Furthermore, a strategy is proposed to recover the produced heat with a lower power in one segment during the tail period for usage in the subsequent segment. This strategy is denoted here as Subsequent Heat Recovery (SHR) strategy. With the aid of the model the added value of the proposed strategy is assessed for a large scale system.

5.2 Experimental system setup

An open sorption heat storage system for application in the built environment generally consists of a solar collector as the heat source, a borehole system as the humidifier, a sorption reactor for long term energy storage and a water vessel for short term energy storage. In order to simulate the thermochemical heat storage system in the lab, a test setup is designed. A schematic illustration of the system setup is shown in Figure 5.1. Compressed air is delivered to the setup and the flow rate is regulated by a Mass Flow Controller (MFC). During the hydration phase, a bubble column is used as humidifier. Air blows from the bottom of the bubble column and humid air is collected at the top. The bubble column is filled with $1l$ of water and the water level in the column is automatically maintained with a Pharmacia LKB Pump P-500. After the bubble column, a collecting vessel is embedded in order to separate water droplets in the air flow. The produced humid air in the bubble column reacts with the material in the reactor and heat is released. The same Zeolite 13XBF material, that is investigated in chapter 2, is used as sorbent here. An air-to-water heat exchanger is placed after the reactor in order to extract the heat from the hot outflow air of the reactor to simulate the heat sink in the demand side. The heat in the hot outflow air from the reactor is used to heat up water in the water vessel. The water vessel simulates a short-term storage tank, which can be used directly for space heating and/or domestic hot water. The achievable temperature lift in the reactor is limited, hence, it is needed to preheat the the cold humid inflow from the bubble column into the system. An air-to-air heat exchanger is implemented to recuperate the available residual heat in the outflow of the system to preheat the inflow air, in order to achieve the required temperature for domestic hot tap water. During the dehydration phase, a heater is used in order to simulate the solar collector in the setup. An Omega

heater AHPF-122 with a power of 1200W is used, and is controlled by a West Control Solution controller (West 6100 Digital Temperature Controller).
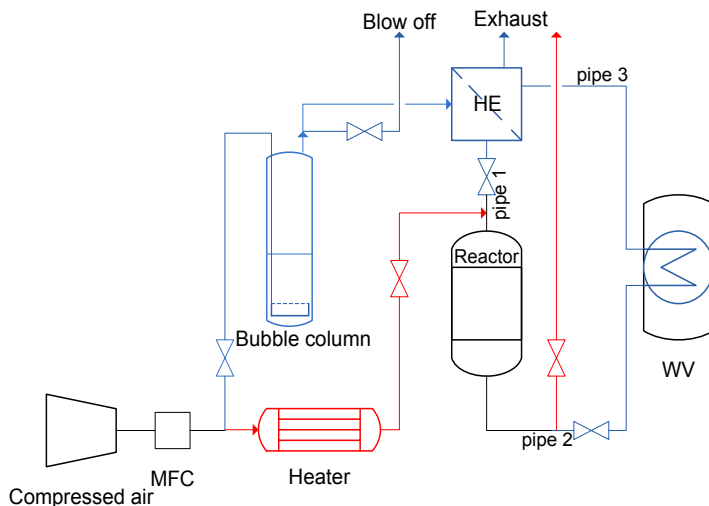
Figure 5.1: Schematic view of the system setup.

A detailed view of the reactor as the main part of the setup is shown in Figure 5.2. The reactor has two separate material bed sections packed on top of each other with 10mm distance in between. At the top and bottom of each section, a wire mesh (with a wire thickness of 450μm and a mesh opening of 820μm) is used to hold the material in place. Each wire mesh is constructed in a stainless steel ring frame with six ribs to support it, and is fixed at a vertical rod at the center of the reactor. The rod is fixed at the top and bottom caps of the reactor. The reactor is designed in a way to secure a modular flexible yet stable configuration. The reactor provides the possibility of running the two sections of the material bed in different operating configurations and flow directions, and also the distance between the sections is adjustable. In this work, the two sections are run in series and the flow direction is from bottom to top, as shown in Figure 5.3. The entire reactor is insulated with 25mm of glass wool insulation (Isover ML3/H). The insulation can resist temperatures up to 260$^o C$ which is higher than the maximum operating temperature.

A plate counter flow Heat Exchanger (HE) is used as the recuperator, with a width of 120mm, height of 116mm and length of 526mm, and consisting of 40 stainless steel plates with a thickness of 0.5mm, with a total heat transfer area of 2.4m^2 and a total mass of 13.4kg. The HE is insulated with 50mm of glass wool insulation (Isover ML3/H). Another plate counter flow heat exchanger is used in the Water Vessel (WV), with a width of 73mm, height of 119mm and length of 191mm, and consisting of 50 stainless steel plates with a thickness of 0.5mm, with a total heat transfer area of 0.6m^2 and a total mass of 2.23kg. The WV is insulated with 20mm of PUR rigid foam insulation. All the components in the
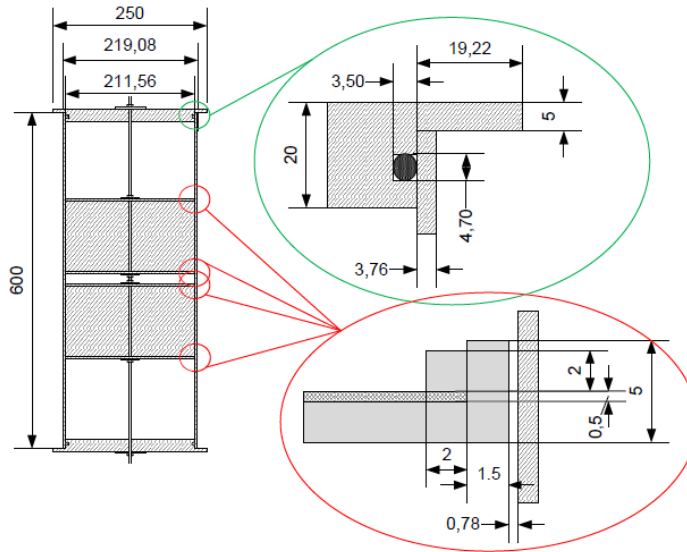
Figure 5.2: Detailed view of the reactor.
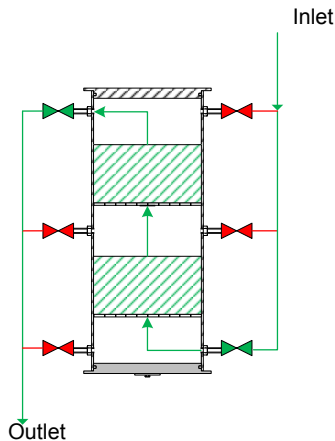
Figure 5.3: Experimental operating configuration and flow direction in the reactor; red valves are closed and green valves are open.

system are connected with three pipes with $8mm$ inner diameter and $1mm$ wall thickness. The pipes are tagged as: pipe 1 between the HE and the reactor ($2.61m$); pipe 2 between the reactor and the WV ($1.96m$); and pipe 3 between the WV and the HE ($0.77m$). The piping is insulated with Armacell Armaflex HT piping insulation with $19mm$ thickness. The general characteristics of the lab scale setup are presented in Table 5.1.

In the experimental setup, water is stagnant in the WV and the water side of the air-to-water heat exchanger is used as the water reservoir. Therefore, the water flow rate in the WV ϕ_w is 0 where the experimental setup is considered (section 5.4). But in the further study on the thermal analysis of the up-scaled system in section 5.5 and section 5.6, a water flow rate of $200l/day$ is applied.

property	value [unit]
Volume of bed (V_b)	$8.78[l]$
Air flow rate (ϕ_a)	$5[l/s]$
Volume of water in WV (V_{water})	$0.45[l]$
Inlet water concentration (c_{in})	$0.57[mol/m^3]$
Heat transfer surface in HE (S_{HE})	$2.4[m^2]$
Heat transfer surface in WV (S_{WV})	$0.6[m^2]$
Length of HE (L_{HE})	$0.526[m]$
Length of WV (L_{WV})	$0.191[m]$
Bed density (ρ_b)	$690[kg/m^3]$
Bed porosity (ϵ_b)	$0.4[-]$
Bed heat capacity ($C_{P,b}$)	$880[J/kg.K]$

Table 5.1: Characteristics of the lab scale system setup.

5.3   Numerical system model

In order to get more insight into the process, a mathematical model is developed for the complete system. The system consists of three main components (heat exchanger, reactor and water vessel) and the pipes connecting these components as depicted in Figure 5.1.

In section 2.4, a model including mass and energy transfer in a thermochemical heat storage reactor is developed and validated, which is also used as the reactor model here. The mass and heat transfer problem in the reactor is described by a set of four PDEs, along the axial coordinate (z) and the time (t):

- Equation 2.9 for modeling the water concentration in the gas phase (c);

- Equation 2.11 for modeling the bed temperature (T_b);

- Equation 2.14 for modeling the wall temperature (T_R);

- Equation 2.1 for modeling the water loading in the solid phase (q).

A modified axial mass dispersion coefficient is used in the model, as discussed in subsection 4.6.1, in order to include also the presented radial effects in chapter 4 into the model.

The heat transfer problems in the air-to-air heat exchanger (HE) can be described by three PDEs as depicted in Figure 5.4. Three entities are considered:
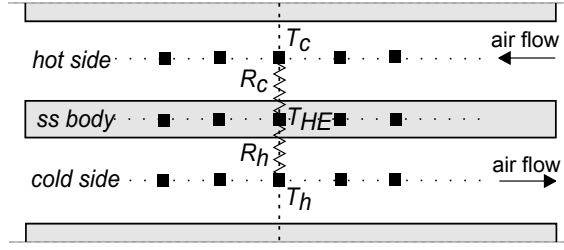
Figure 5.4: Schematic view of the model describing the air-to-air heat exchanger.

the hot flow of the HE; the cold flow of the HE; and the stainless steel body of the HE. The temperature of each of the entities is governed by a one-dimensional heat balance PDE along the axial coordinate (z) over time (t). It is assumed that the cold and hot sides of the HE are in thermal contact with each other and with the ambient only through the stainless steel body of the HE. The heat conduction in the fluid phases in the cold and hot sides of the HE (air in both sides, here) is neglected.

The heat balance governing the temperature of the flow at the hot side in the HE (T_h) is given by:

$$\rho_g C_{P,g} \frac{\partial T_h}{\partial t} + \rho_g C_{P,g} \frac{\phi_a}{A_h} \frac{\partial T_h}{\partial z} = -\frac{(T_h - T_{HE})}{R_h A_h} \tag{5.1}$$

where $C_{P,g}$ and ρ_g are the gas heat capacity and density, ϕ_a is the air flow rate, A_h is the cross sectional area and R_h is the heat transfer resistance at the hot side of the HE. The heat transfer resistance at the hot side of the HE is defined as $R_h = (\frac{1}{h_h}).(\frac{L_{HE}}{S_{HE}})$, where h_h is the heat transfer coefficient at the hot side of the HE, and S_{HE} is the internal heat transfer surface between the cold and hot sides of the HE (Table 5.1).

The governing heat balance equation for the temperature of the flow at the cold side in the HE (T_c) is given by:

$$\rho_g C_{P,g} \frac{\partial T_c}{\partial t} + \rho_g C_{P,g} \frac{\phi_a}{A_c} \frac{\partial T_c}{\partial z} = \frac{(T_{HE} - T_c)}{R_c A_c} \tag{5.2}$$

where A_c and R_c are the cross sectional area and the heat transfer resistance at the cold side of the HE, respectively. The heat transfer resistance at the cold side of the HE is defined as $R_c = (\frac{1}{h_c}).(\frac{L_{HE}}{S_{HE}})$, where h_h is the heat transfer coefficient at the cold side of the HE.

The governing heat balance equation for the temperature of the stainless steel body in the HE (T_{HE}) is given by:

$$\rho_{ss} C_{P,ss} \frac{\partial T_{HE}}{\partial t} - \lambda_{ss} \frac{\partial^2 T_{HE}}{\partial z^2} = \frac{(T_h - T_{HE})}{R_h A_{HE}} - \frac{(T_{HE} - T_c)}{R_c A_{HE}} - \frac{(T_{HE} - T_{amb})}{R_{loss,HE} A_{HE}} \tag{5.3}$$

where A_{HE} is the cross sectional area of the HE, and ρ_{ss}, $C_{P,ss}$ and λ_{ss} are

the density, heat capacity and thermal conductivity of stainless steel, respectively.. The heat loss resistance of the HE to the ambient temperature T_{amb} is defined as $R_{loss,HE} = (\frac{d_{ins}}{k_{ins}}).(\frac{L_{HE}}{S_{loss,HE}})$, where d_{ins} and k_{ins} are the thickness and conductivity of the insulation, respectively, and the heat transfer surface for the heat loss from the HE is the external surface of the HE and is calculated as $S_{loss,HE} = 2 \times (width \times height + heigh \times length + length \times width)$.

The heat transfer problems in the air-to-water heat exchanger in the water vessel (WV) can also be described by three PDEs along the axial coordinate (z) and the time (t). The same model with different coefficients can be used for the WV. The heat transfer coefficient in the WV model is calculated by the similar correlations as the HE, but then with the corresponding parameters for the WV.

The governing heat balance equation for the temperature of the water flow in the WV (T_w) is given by:

$$\rho_w C_{P,w} \frac{\partial T_w}{\partial t} + \rho_w C_{P,w} \frac{\phi_w}{A_w} \frac{\partial T_w}{\partial z} = \frac{(T_{WV} - T_w)}{R_w A_w} \tag{5.4}$$

where A_w and R_w are the cross sectional area and the heat transfer resistance at the water side of the WV, respectively, and ϕ_w is the water flow rate.

The governing heat balance equation for the temperature of the air flow in the WV (T_a) is given by:

$$\rho_g C_{P,g} \frac{\partial T_a}{\partial t} + \rho_g C_{P,g} \frac{\phi_a}{A_a} \frac{\partial T_a}{\partial z} = -\frac{(T_a - T_{WV})}{R_a A_a} \tag{5.5}$$

where A_a and R_a are the cross sectional area and the heat transfer resistance at the air side of the WV, respectively, and ϕ_a is the air flow rate.

The governing heat balance equation for the temperature of the stainless steel body in the WV (T_{WV}) is given by:

$$\rho_{ss} C_{P,ss} \frac{\partial T_{WV}}{\partial t} - \lambda_{ss} \frac{\partial^2 T_{WV}}{\partial z^2} = \frac{(T_a - T_{WV})}{R_a A_{WV}} - \frac{(T_{WV} - T_w)}{R_w A_{WV}} - \frac{(T_{WV} - T_{amb})}{R_{loss,WV} A_{WV}} \tag{5.6}$$

where A_{WE} is the cross sectional area of the WV and $R_{loss,WV}$ is the heat loss resistance of the WV to the ambient temperature T_0.

It is assumed that in each point in the pipes, the air flow in the pipe and the stainless steel body of the pipe are in thermal equilibrium. Therefore, the governing heat balance equation for the temperature of the air flow in the pipes and the body of the pipe (T_p) can be written as:

$$(\rho_g C_{P,g} + \rho_{ss} C_{P,ss} \frac{A_{ss,p}}{A_p}) \frac{\partial T_p}{\partial t} + \rho_g C_{P,g} \frac{\phi_a}{A_p} \frac{\partial T_p}{\partial z} - \lambda_{ss} \frac{A_{ss,p}}{A_p} \frac{\partial^2 T_p}{\partial z^2} = \frac{(T_p - T_{amb})}{R_p A_p}$$
$$\tag{5.7}$$

where A_p and $A_{ss,p}$ are the cross sectional area of the inside and stainless steel body of the pipe, and R_p is the heat loss resistance from the pipes to the ambient.

The heat exchanger model is validated with the analytical solution of the set of PDEs for a simplified steady state case for the WV, and analogically for the
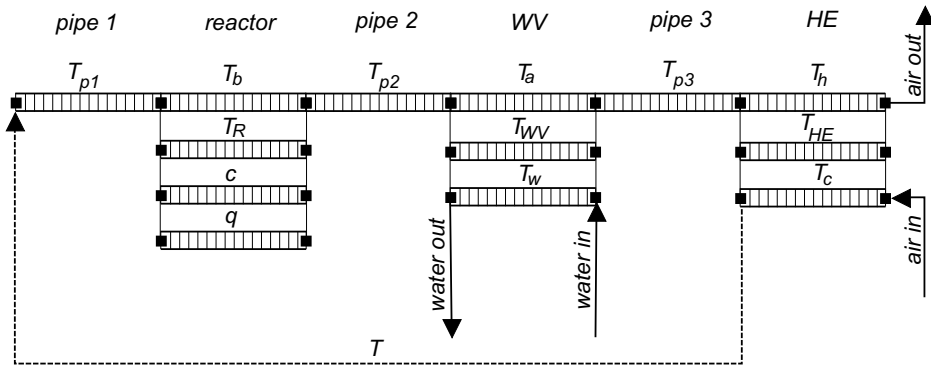
Figure 5.5: Schematic view of the complete system model.

HE. The same characteristics as for the WV heat exchanger in the experimental setup are used. A water flow rate of $0.001 l/s$ is applied with an inlet temperature of $20^o C$. The air flow rate is similar to the experimental condition ($5 l/s$) with a pre-defined inlet temperature of $70^o C$. The stainless steel body is assumed to be negligibly thin, and the heat losses are neglected. The conductive heat transfer in the air and water sides of the air to water heat exchanger are also neglected. For this simplified case, the numerical and analytical solutions perfectly match.

The complete model as presented above, is developed and solved in COMSOL Multiphysics, which is a Finite Element Method (FEM) based program. The PDEs are discretized in space by Lagrange linear shape functions. Both the bed and wall domains are meshed with an element size of 1 mm, chosen based on a mesh convergence study for the reactor model, and the same element size is used for the other domains as well for simplicity, since the model is reasonably fast. The solver is a fully coupled time-dependant solver. The Backward Differentiation Formula (BDF) scheme (maximum order of 5 and a minimum order of 1) with an initial time step of 0.001 s is used as the time stepping method. The relative, absolute and event tolerances are set to 1E-2. The initial conditions are set as $T_{amb} = 22[^o C]$, $c_0 = 0[mol/m^3]$ and $q_0 = 3.5[mol/kg]$. The schematic view of the complete system model is presented in Figure 5.5. The model is validated by means of comparing the numerically calculated and the experimentally measured temperature profiles in the next section.

5.4 System Performance

The lab scale test rig described in section 5.2 is used for the experimental investigation on hot tap water production by employing the thermochemical heat storage. It is shown experimentally that by implementing the recuperator, it is possible to produce water with a temperature of at least $60^o C$, as required for hot tap water. Figure 5.6 shows the inlet and outlet temperature of the reactor. The pre-heated humid air in the cold side of the heat exchanger flows into the reactor
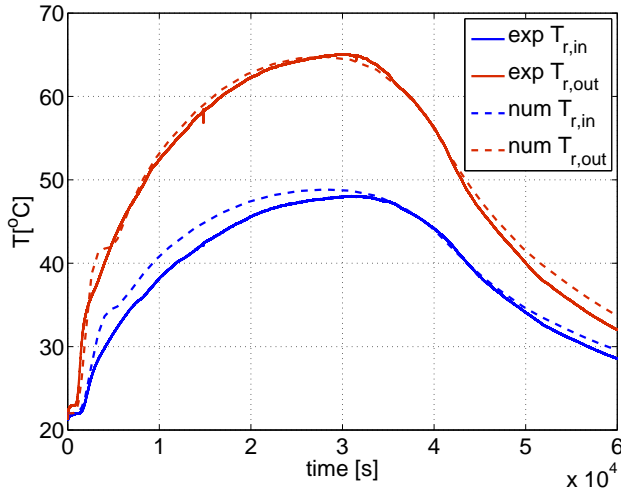
Figure 5.6: Air temperature at the inlet and outlet of the reactor.
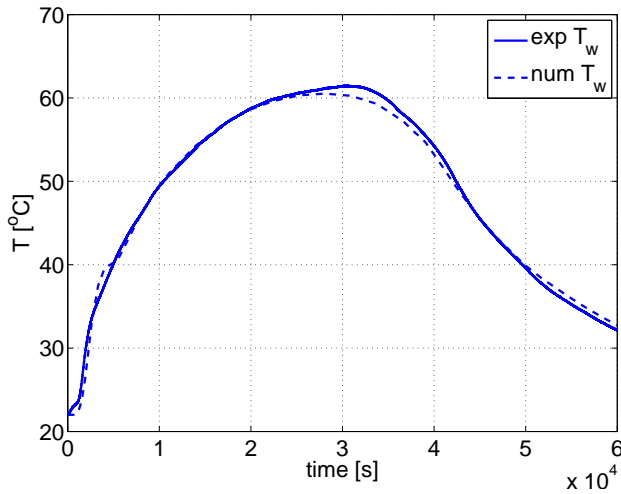
Figure 5.7: Water temperature at the water side of the air-to-water heat exchanger in the water vessel.

and reacts with the thermochemical material packed in the reactor. In this experiment, the maximum temperature step achieved between the outflow and inflow of the reactor is about $18^o C$. The experimental results are also used to validate the model, by comparing the temperature measured and simulated in different locations of the system. A good match is found in the comparison between the numerical and experimental results.
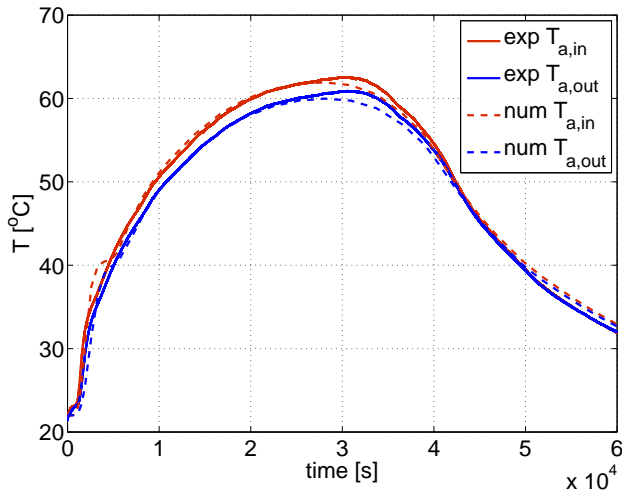
Figure 5.8: Inlet and outlet temperature of the air side of the air-to-water heat exchanger in the water vessel.
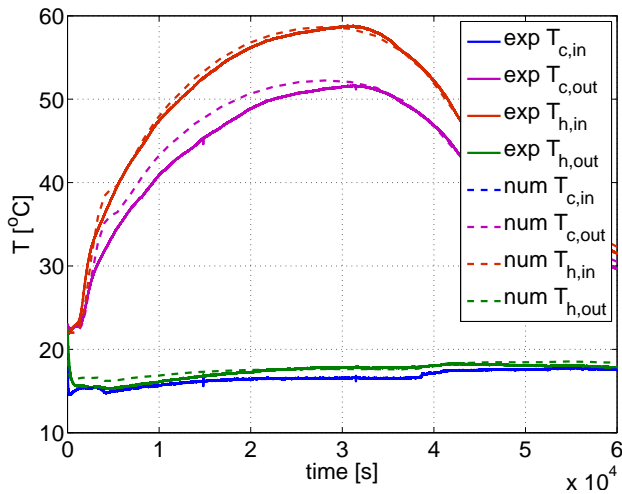
Figure 5.9: Inlet and outlet temperature of the hot and cold sides of the air-to-air heat exchanger.

The measured temperature of water in the WV is shown in Figure 5.7. In the experimental setup, there is no water flow in the water side of the air-to-water heat exchanger and water is stagnant. However the temperature of the water is measured at two locations tagged as inlet and outlet of the WV. The temperature measured in the two locations are almost similar during the whole process.

In the experiment, the water reaches the average temperature of 60^oC at around $23000s$ and stays above 60^oC till around $35000s$. The numerically calculated water temperature is also almost uniform over the length of the WV. The average calculated temperature of the water is shown in Figure 5.7 and is compared with the experimental one, indicating a good match. Figure 5.8 shows the experimental and numerical temperature of the inflow and outflow air of the air-to-water heat exchanger in the water vessel.

Figure 5.9 shows the inlet and outlet temperature of the hot and cold sides of the air-to-air heat exchanger. The cold side inflow is the humid air provided by the humidifier, and the temperature is the equilibrium temperature attained in the humidifier. In the counter flow air-to-air heat exchanger, the warm air from the water vessel flows to the hot side of the heat exchanger, and the heat is transferred to the heat exchanger body and subsequently to the cold side flow or is lost to the ambient through the insulation on the heat exchanger. Since the flow rates of both sides are the same, the total efficiency of the heat exchanger can be defined as $(T_{c,out} - T_{c,in})/(T_{h,in} - T_{h,out})$, and is calculated to be around 88%. It can be concluded that the heat transfer area of the heat exchanger is large enough because the temperature of the hot side at the outlet is dropped to the temperature of the cold side inflow. The heat loss observed here can be caused by heat loss from the heat exchanger or by air leakage. However, the setup is inspected by foaming agent, and leakage is considered to be unlikely. Therefore, the only way to improve the efficiency of the HE is by improving the insulation.

5.5 Thermal analysis

In the previous section, the model is validated by the results from experiments performed in the lab scale system setup with the characteristics presented in Table 5.1. In this section, the validated model is used to study the performance of an up-scaled system. The volume of a reactor segment (filled with the same zeolite 13XBF as before) and the air flow rate in a large scale system are implemented in the model. The inlet water concentration is chosen at $13mbar$ water vapor pressure. A water flow (based on the typical average DHW demand in the built environment[99]) with the inflow temperature of 20^oC is applied in the water side of the WV, in order to extract the heat continuously by water. The characteristics of this large scale reference case are presented in Table 5.2. The the air-to-air heat exchanger HE (recuperator) and the air-to-water heat exchanger WV are up-scaled compared to the lab scale setup. The heat transfer surface of the HE is sized in a way that can provide the efficiency of around 90% at the maximum temperature. The heat transfer surface of the WV is sized such that the average water temperature of 60^oC is maintained. The volume and mass of the HE and WV are assumed to be linearly proportional to the heat transfer surfaces of the heat exchangers. Further study should be done on the optimized sizing of the heat exchangers. The length and diameter of the pipes and the level of insulation on the components is doubled compared to the experimental setup.

In order to investigate the thermal performance of the system, energy flows

property	value [unit]
Volume of bed (V_b)	62.5$[l]$
Air flow rate (ϕ_g)	40$[l/s]$
Water flow rate in WV (ϕ_w)	200$[l/day]$
Inlet water concentration (c_{in})	0.57$[mol/m^3]$
Heat transfer surface in HE (S_{HE})	5.9$[m^2]$
Heat transfer surface in WV (S_{WV})	1.2$[m^2]$

Table 5.2: Characteristics of the large scale reference case.

are calculated based on temperatures in different locations of the system. Figure 5.10 shows a schematic view of the energy flows in the system, and the equations used to calculate them are presented in Table 5.3.
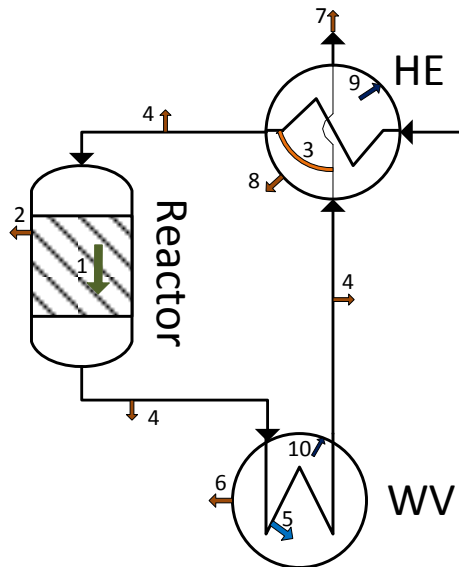
Figure 5.10: Illustration of the energy flows in the system, numbered as presented in Table 5.3.

Term #1 is the reaction thermal power produced in the reactor which is estimated based on the reaction rate dq/dt and the reaction enthalpy ΔH calculated in the model, and integrated over the length of the reactor. Term #2 represents the heat loss from the reactor and is calculated based on the difference between the bed temperature (T_b) and the reactor wall temperature (T_r), and integrated over the length of the reactor. Term #3 is the energy recuperated per unit of time in the HE, which is the energy gained in the cold side flow, appearing as temperature increase between the cold side inflow ($T_{c,in}$) and outflow ($T_{c,out}$). Term #4 is the

heat loss from the pipes, which is proportional to the difference between the pipe temperature (T_p) and the ambient temperature (T_0), integrated over the lengths of the pipes. Term #5 is the extracted thermal power by water in the WV. This term is a combination of the energy removed from the system by the water flow in the WV and the sensible energy stored in the water inside the WV at each time; the former one appears in the temperature lift between the inlet and outlet of the water flow ($T_{w,out} - T_{w,in}$), and the latter one in the temperature gain in the contained volume of water inside the WV heat exchanger itself (dT_w/dt). Term #6 is the heat loss from the WV, and is calculated based on the difference between the WV body temperature (T_{WV}) and the ambient temperature (T_0), integrated over the length of the WV. Term #7 is the energy lost by blowing off the outflow air to the ambient. Term #8 is the heat loss from the HE, and is calculated based on the difference between the HE body temperature (T_{HE}) and the ambient temperature (T_0), integrated over the length of the HE. Terms #9 and #10 are the sensible heat stored in the body of the WV and HE, respectively.

#	term			
1	Reaction power	$P_{reaction}$	$=$	$\int_0^{L_R} \rho_b A_b \frac{dq}{dt} \Delta H dz$
2	Loss from reactor	$P_{loss,r}$	$=$	$\int_0^{L_R} \frac{T_b - T_R}{R_i} dz$
3	Recovered in HE	P_{recup}	$=$	$\rho_g C_{P,g} \phi_g (T_{c,out} - T_{c,in})$
4	Loss from pipes	$P_{loss,p}$	$=$	$\int_0^{L_p} \frac{T_p - T_0}{R_p} dz$
5	Extracted by water	P_{water}	$=$	$\rho_w C_{P,w} \phi_w (T_{w,out} - T_{w,in})$
				$+ \int_0^{L_{WV}} \rho_w C_{P,w} A_w \frac{dT_w}{dt} dz$
6	Loss from WV	$P_{loss,WV}$	$=$	$\int_0^{L_{WV}} \frac{T_{ss,WV} - T_0}{R_{loss,WV}} dz$
7	Loss by the outflow	P_{out}	$=$	$\rho_g C_{P,g} \phi_g (T_{h,out} - T_{c,in})$
8	Loss from HE	$P_{loss,HE}$	$=$	$\int_0^{L_{HE}} \frac{T_{ss,HE} - T_0}{R_{loss,HE}} dz$
9	sensible in HE	$P_{sens,WV}$	$=$	$\int_0^{L_{WV}} \rho_{ss} C_{P,ss} A_{ss,WV} \frac{dT_{ss,WV}}{dt} dz$
10	sensible in WV	$P_{sens,HE}$	$=$	$\int_0^{L_{HE}} \rho_{ss} C_{P,ss} A_{ss,HE} \frac{dT_{ss,HE}}{dt} dz$

Table 5.3: Equation used to calculate different energy flows considered in the system.

In order to compare the importance of different terms, the calculated powers are summarized in following categories:

- convection ($P_{conv} = P_{reaction} - P_{loss,r}$): extracted energy from reactor

- water (P_{water}): energy stored in water

- loss ($P_{loss} = P_{loss,pipe} + P_{loss,HE} + P_{loss,WV}$): heat loss through walls

- sensible ($P_{sens} = P_{sens,HE} + P_{sens,WV}$): sensible heat stored in HE and WV

- outflow (P_{out}): heat loss by outflow air

- recuperate (P_{recup}): heat recuperated in HE

The powers are calculated over time and presented in Figure 5.11. The total energies can be calculated by integration of powers from the start of the hydration
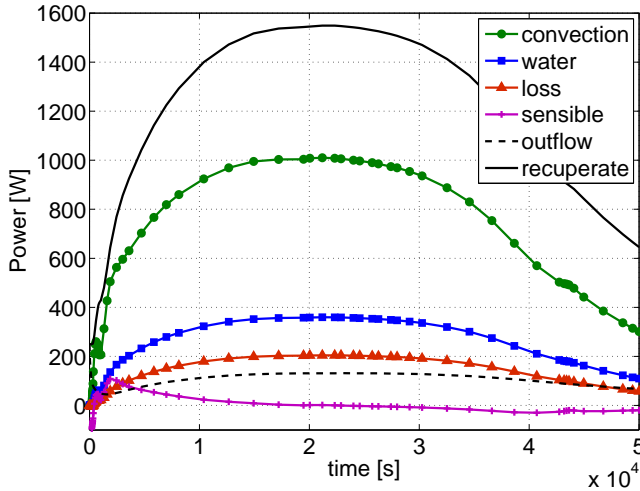
Figure 5.11: Energy flows in the system during the discharge phase.

till a certain time as $E = \int_0^t P dt$. In this case, the tail period of the discharge phase is between 30000 to 40000 s, as can be seen in Figure 5.11. The energies are calculated till $35000s$ and presented as a sankey diagram in Figure 5.12. As can be seen, around $30MJ$ of energy is produced in the reactor and transferred by convection, from which around $20MJ$ is extracted by water in the WV. It means a system efficiency (E_{water}/E_{conv}) of about 67%. The rest is lost to the ambient by three different mechanisms: (1) conductive heat loss through the walls of the system; (2) convective heat loss by the outflow air; and (3) sensible heat loss in the thermal mass of the system. The conductive heat loss through the walls of the system is around 70% of the total heat loss, from which around 70% is lost in the pipes. It shows the importance of the system compactness and reducing the length of the required piping. In addition, the insulation level used on the pipes seems to be insufficient.

5.6 Heat recovery

In a thermochemical heat storage reactor, the presence of the reactor wall surrounding the material bed creates radial effects in the reactor. These effects can be caused by (i) heat losses to the ambient through the wall, (ii) a higher porosity in the wall region, resulting in flow channelling, and (iii) non-uniform initial state of charge near the wall due to an inhomogeneous charging temperature (due to wall heat loss). The flow channelling in the reactor can cause faster propagation of the reaction front in the near-wall region of the bed, compared to the center of the bed. It means that when the reaction front in the near-wall region reaches the bottom of the bed, the reaction in the center of the bed is still ongoing. This causes
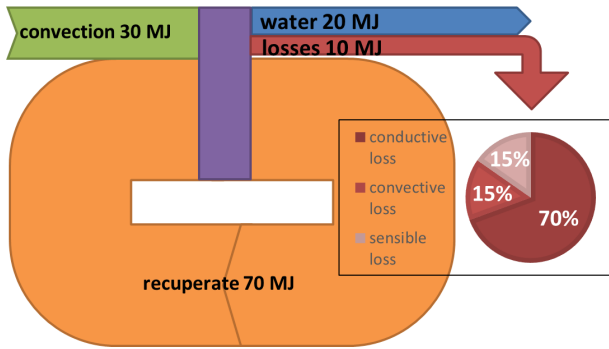
Figure 5.12: Sankey digram for the energy terms.
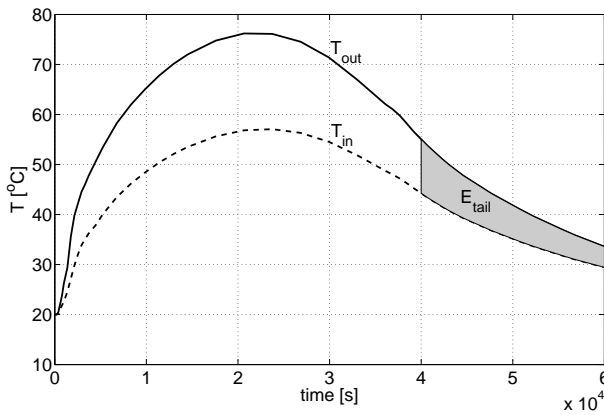
Figure 5.13: Temperature at the inlet T_{in} and outlet T_{out} of the reactor segment N for DS, and the energy associated to the tail period E_{tail}.

a tail period at the end of discharge phase which has a lower reaction power compared to the average power of the reactor, and leads to a gradual decrease in the temperature of the reactor outlet and a gradual increase in the outflow water concentration. This phenomenon is extensively investigated in chapter 4. In this section, the effect of this tail period is studied for the up-scaled system with the characteristics presented in Table 5.2.

The energy associated with the tail period of the discharge phase can not be utilized because of the lower power. The normal strategy for shifting to the subsequent segment is denoted here as Discrete Shift (DS). It simply means to stop the running segment when its tail period starts, and start the next segment. The model is used in order to simulate the reference up-scaled system (characteristics in Table 5.2) with the DS strategy. Based on the result from the model, the average water temperature by utilizing the energy during the whole discharge phase from the beginning till the end ($0 - 60000s$) is 55.9^oC. To avoid a lower

temperature than the required hot tap water temperature, the process should be stopped at the start of the end tail ($0 - 40000s$). In that case, a higher temperature of around 63.2^oC can be achieved. However, the energy associated with the tail period of the discharge phase is calculated to be around $7MJ$ which is around 20% of the total extracted convection energy (Figure 5.13). This energy can not be utilized, which leads to a decrease in the energy density of the system. Additional heat loss from the system (not considered here) is caused by blowing off the humid outflow air during the tail, caused by the fact that water evaporation is an energy consuming process which happens prior to the system and leads to a temperature drop over the humidifier.
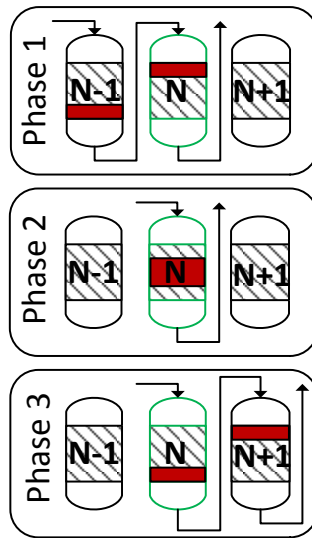
Figure 5.14: Schematic view of three phases of the process with subsequent heat recovery.

An alternative strategy, denoted here as Subsequent Heat Recovery (SHR), is proposed in order to avoid the above mentioned heat losses. The concept is based on the heat recovery from one segment to the subsequent segment, as depicted in Figure 5.14. For the segment N, the process with SHR consists of three phases:

1. Phase 1: recovering heat from previous segment ($N - 1$) to next segment (N) by running the two segments in series during the tail period of the segment $N - 1$

2. Phase 2: normal discharge of the singular segment N

3. Phase 3: depleting heat from the running segment N during its tail period to the next segment $N + 1$ by running them in series

By employing the SHR strategy, the energy associated to the tail period of the segment N can be utilized by transferring it to the subsequent segment $N + 1$.

This way the energy storage density can be improved by around 20%. However, this still needs to be checked in more details. In addition, the humidity available in the outflow of segment N will be reacted in the segment $N + 1$ during this period. This also helps to improve the energy density.

According to the numerical result from the model, there is still around $5MJ$ (13%) energy left in the segment after $60000s$ of discharging the segment. But, it can be extracted in case the process last for almost double the time ($34h$), which is not feasible. In addition, because of the low power the energy is not useful. Therefore, it is decided to stop the process for each segment after around $17h$. However, the shift times should be optimized in future works. Running two segments in series increases the required fan power to blow air through the beds. However, the pressure drop over the bed is negligible compared to the other pressure drops in the system, such as pressure drops in the piping and heat exchangers.

5.7   Conclusion

An open sorption heat storage system based on segmented packed beds of zeolite is developed in order to provide hot tap water. The system consists of a bubble column humidifier, a sorption reactor, an air-to-water heat exchanger in a water vessel and an air-to-air heat exchanger as recuperator. The system setup is tested experimentally and modelled numerically. The model is validated by the experimental results. By implementing the air-to-air heat exchanger in order to recuperate the heat in the outflow of the system to preheat the inlet humid air, the 60^oC temperature as required for hot tap water is achieved. The total efficiency of the recuperator is calculated to be around 88%. The heat transfer surface of the heat exchanger is large enough since the outflow hot temperature is almost equal to the cold inflow air. However, the recuperator can be improved by reducing the heat loss through the insulation.

The model is used to establish a complete energy map of an up-scaled thermochemical heat storage system by a reactor segment size of $62.5L$. It is shown that the largest heat loss from the system (70%) is by the conductive heat loss through the walls of the system, from which around 70% is lost in the pipes. It shows the importance of the system compactness and reducing the length of the required piping.

The system efficiency during the discharge is calculated to be 67%, in case the process stops before the tail period (in this case $35000s$). However, stopping the discharge of a segment before the tail means losing the energy associated with the tail period, which is around 20% of total extracted energy from the segment. This leads to a lower energy density for the system. The Subsequent Heat Recovery (SHR) strategy is proposed in order to recover the heat produced in one segment during its tail period to the subsequent segment by running them in series.

6

PILOT REALIZATION

6.1 Introduction

In recent years, intense research was performed on innovative system designs to integrate the thermochemical concept into an overall system, and lab or pilot scale setups are developed and tested. Table 6.1 presents some of the reported prototypes working with the zeolite material in fixed bed reactors as open systems. Operating conditions, reactor energy densities and maximum thermal power output are also presented.

project	material	charge temp. $[^oC]$	discharge temp. $[^oC]$	energy density $[kWh/m^3]$	max. power $[kW]$
MONOSORP[100]	70 kg zeolite 4A	170	20	120	1.5
STAID[98]	80 kg zeolite 13X	180	20	114	2.25
E-HUB/ECN[101]	150 kg zeolite 13X	185	25-60	58	0.4

Table 6.1: Prototypes along with operating conditions for open and closed systems.

The *MONOSORP*[100] prototype is developed based on zeolite honeycomb structures called monoliths instead of the ordinarily employed packed beds. The monoliths are made by extrusion of zeolite 4A into integrated shaped bodies with a large number of small straight channels inside. The main advantage of using such a material bed is low pressure drop. However, the monolith production adds up to the material cost. With an inlet temperature of about 20^oC and a

humidity of $6g/kg$ (gram of water to kilogram of air) a maximum temperature lift of around 22^oC is achieved.

The $STAID$[98] prototype is a system consisting of two reactor segments, where zeolite 13X spherical particles are packed. The system can provide a maximum thermal power output of around $2.25kW$ during $6h$, with a maximum instantaneous COP (considering only electrical consumption during the hydration process) of 6.8. The inflow air has a relative humidity of around 70% at 20^oC, which corresponds to a water vapor pressure of about $16mbar$ or an absolute humidity of about $10g/kg$. This high value for the inlet humidity is the reason for the achieved high power.

The E-HUB/ECN[101] prototype is a system consisting of two packed bed reactor segments working with zeolite 13X. This system is developed such that it can provide thermal power at higher temperature compared to the above-mentioned systems. In this setup, an air-to-air heat exchanger is employed in order to preheat the inflow air by the residual heat in the outflow air. An inlet humidity of $12mbar$ water vapor pressure is applied. Air leakages inside the system lead to a low thermal power output from the system.

In this chapter, the implementation of thermochemical heat storage in the built environment utilizing solar thermal heat is investigated. Therefore, the operating conditions are chosen based on the application. Specifically, the inflow air should be conditioned carefully regarding the humidity, because the inflow humidity has a large effect on the output of the system. The segmentation concept (introduced in chapter 5) is used in order to reduce heat losses. A large scale high power pilot is realized, consisting of four segments. Each reactor segment contains a $62.5L$ packed beds of the material, which is zeolite 13XBF (introduced in chapter 2) in the form of spherical particles. The packed bed reactor design is chosen because of its simplicity and low cost, while the pressure drop over the bed is reduced by reducing the height-to-width ratio of the bed (discussed in chapter 4). The reactor segments are placed in a system with other components. Air leakage and high pressure are tried to be avoided in different parts of the system. Experiments are performed on the pilot in order to determine the energy storage density, demonstrate the power and calculate the COP. Recommendations are given for further studies on the pilot and for improvements.

6.2 Thermochemical heat storage in the built environment

Before a heat storage strategy is devised it is important to present an overview of the system being developed. Figure 6.1 shows the system overview for the charging and discharging processes. During the charging process in summer, air is blown through a heat exchanger to heat up to the desired temperature by the solar collector. During the discharge process in winter, humidified air from a borehole (i.e. $1300Pa$ water vapor pressure at 10^oC) gets preheated in an air-to-air heat exchanger by the outflow of the reactor and then passes through the reactor.
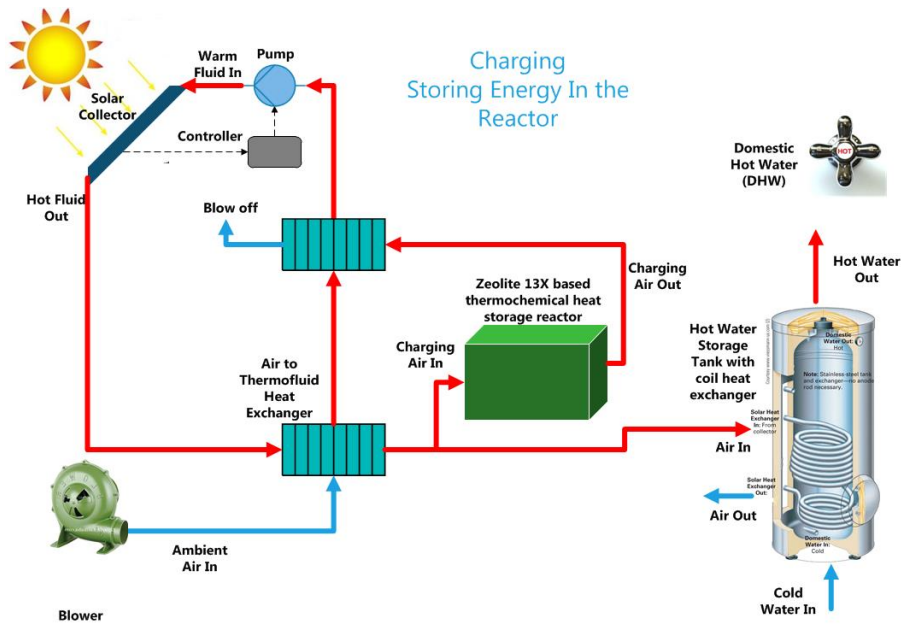
(a) charging process
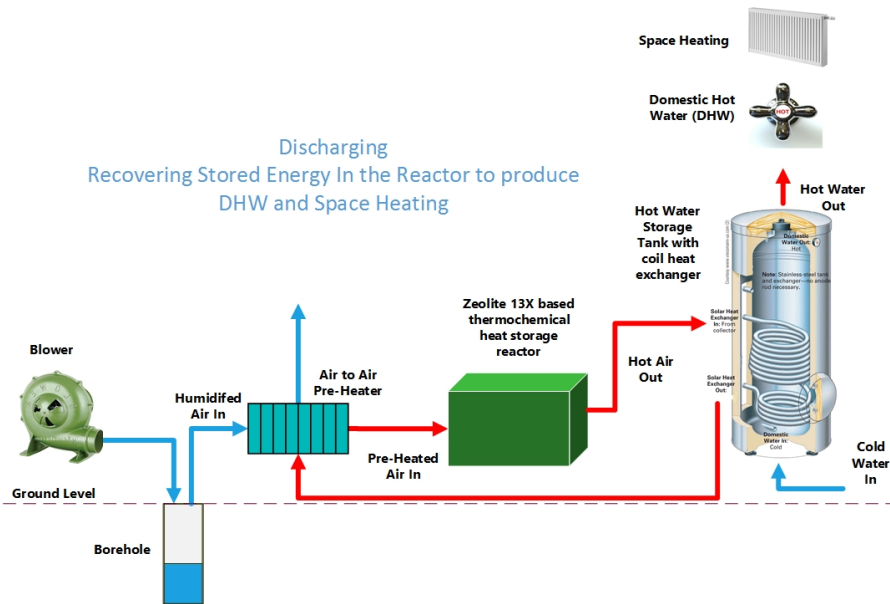
(b) discharging process

Figure 6.1: Implementation of thermochemical heat storage system in residential building

As a reference for energy demand in buildings, the passive house standard is considered. For passive houses, the peak daily average heating and cooling loads are typically below $10W/m^2$ and annual useful energy demands are below $15kWh/m^2$ [102]. Considering a passive house with a floor area of $100m^2$, the total heat demand would be $1500kWh/year$ (which is in relatively low for average houses), and assuming an energy density of $180kWh/m^3$ for storage material, more than $8m^3$ of material is required to store the complete heat demand of the household.

If all the material is packed in a single reactor, the large thermal mass of the entire bed has to be heated up at once, which makes the performance of such a system (with all material packed in one reactor) slow, less controllable, and heat losses become large. Therefore, it is important to keep the reaction zone (the part of the material which participates in and/or is affected by the reaction) as small as possible. A method to reduce the reaction zone, which is denoted here as the segmentation concept, is to pack the material in separate reactor segments and to run only one segment at a time. The segmentation concept provides the simplicity and the low auxiliary energy need of the packed bed reactor design, and meets the limited reaction zone requirement. In this way, it is possible to run the segments in sequence with a constant power, while providing the required average demand. The produced energy can be stored in a short-term heat storage water tank, and the peak demand can be shaved by the water tank.

A monthly strategy can be developed, based on available solar energy, to calculate the number of segments that can be charged per day in a particular month. In addition, different strategies can be used in order to recover heat from one segment to another, as discussed in chapter 5. By choosing a segment size of about $10kWh$, 200 segments would be needed to cover the complete annual heat demand of the house. However, the segment size needs to be optimized based on charging/discharging strategies.

The strategy which is chosen here for discharging is based on the average daily demand. In this way the thermochemical storage system operates continuously and the produced heat is stored in a short term storage tank. The short term hot water storage tank should be large enough to be able to cover the peak demand, while it is continuously charged by the thermochemical storage system. Considering a passive house with an average daily demand of $24kWh/day$, the required average power from the thermochemical reactor would be $1kW$. Assuming a temperature step of 20^oC in the reactor (based on experiments in a small scale setup [103]), an air flow rate of $50g/s$ is calculated for discharging the reactor.

6.3   Realization

At the Eindhoven University of Technology, a pilot setup is realized consisting of four segments. The pilot is designed to be able to provide $1kW$ thermal output per segment and $4kW$ combined, lasting for at least 10 hours. In this section, the realization of the pilot is explained at material, reactor and system level.

6.3.1 Material

The material zeolite 13XBF (CWK Chemiewerk Bad Köstritz GmbH) is used as thermochemical material consisting of spherical beads with an average diameter of 3.5mm. An extensive discussion on the performance of the material is presented in chapter 2. In each segment, 62.5L (42.5kg) of material is packed, with the possibility to increase it to 83.3L by adding more material in the top layer of the reactor.

6.3.2 Reactor

For the reactor segments a square prism (cuboid) shape is chosen, because of practical considerations in the realization of the pilot, as well as of a real system. Building the segments is practically much easier and cheaper with this shape. In addition, in a real system, segments can be stacked besides each other in a more compact way. In chapter 4, an optimum diameter-to-height ratio of 1.5 is found for a cylindrical reactor. However, for a reactor with square cross-section, this ratio might be different. In this pilot, the aspect ratio is 2:1 (Width : Height). A detailed view of the designed reactor segment is shown in Figure 6.2. Two empty spaces, one at the top and one at the bottom of the material bed are embedded in each segment, as headers to ensure a uniform pressure drop over the bed, and hence, a uniform flow through the bed. The volume of each reactor segment (including empty spaces) is 114.75L.

A stainless steel rectangular casing is realized as shown in Figure 6.3. The casing has a stainless steel cover which is bolted on the top side, and is made air tight with a sealant. The air inlet and outlet connections are on the top left and bottom right of the casing, respectively. The wall thickness of the casing is 2mm, which forms a good balance between high mechanical strength and low thermal mass. A perforated sheet is used to hold the material bed in place at a certain height inside the reactor. The sheet is spot welded on top of a support structure placed at the bottom of the segment, in a way that the outlet is placed below the perforated sheet and the support. Another perforated sheet is used on top of the material to help the air distribution. An insulation layer made of glass wool with a thickness of 50mm is used on all sides of the casings.

As can be seen in Figure 6.2, each segment consists of four height levels which can be filled with material. However, in the present configuration that is used in this study, material is filed in the first three levels only (62.5L of material). In future studies, the material can be also filled up to the fourth level, which leads to having 83.3L of material in each segment. Inside one of the segments (denoted as segment 1), thermocouples are placed in order to analyze the internal behavior of the packed bed. The location of the thermocouples is chosen in a way that the effect of the flow distribution in the bed can be analyzed. By placing thermocouples in the corners of the packed bed, formation of any non-reactive zones inside the bed can be identified. The thermocouples are positioned at four different heights inside the reactor, and at each height there are six thermocouples.
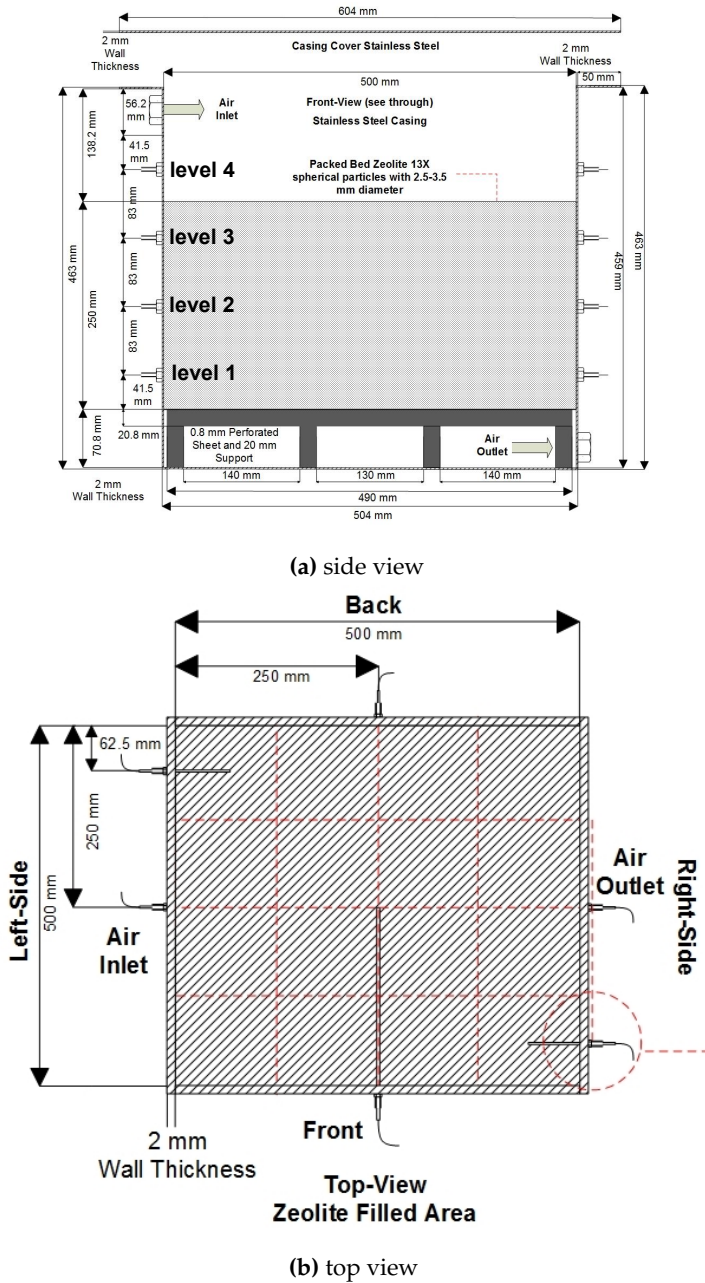
(a) side view

(b) top view

Figure 6.2: Detailed view of reactor

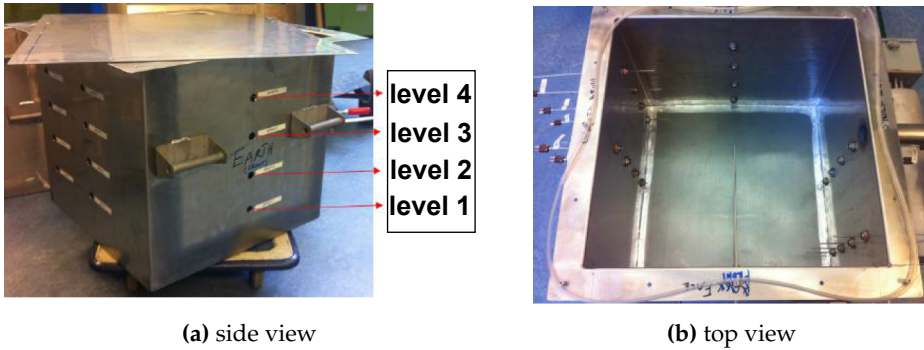**(a)** side view   **(b)** top view

Figure 6.3: Pictures of realized reactor

6.3.3 System

A system is developed to accommodate the four reactor segments in the setup simulating the real thermochemical heat storage system for household application. A schematic view of the complete system is shown in Figure 6.4. In order to have flexibility in the operation of multiple segments, each segment is connected to an individual pipeline. Air flows into the system from the main inlet pipe, and then is divided over four paths. In each path, the air flow can be conditioned for either charging (dehydration) or discharging (hydration). The pressure and temperature of the flow are measured in the main pipe.

In each path, the flow rate is controlled and measured by a Mass Flow Controller capable of handling $50g/s$ flow with an accuracy of $\pm 0.4\%$. A 3-way valve is used in order to direct the flow to the humidifier for the hydration process or bypass it for the dehydration process. During the hydration process the flow is humidified in a bubble column. The humidity of the flow is measured after the humidifier by a humidity-temperature sensor with a humidity accuracy of $\pm 1.25\%$ RH at $23^{o}C$ and temperature accuracy of $\pm 0.2^{o}C$. After the humidifier, another 3-way valve is used in order to blow off the flow during the stabilization time required for the humidifier. The temperature of the flow is measured after the valve by a Type T thermocouple with Stainless steel protective jacket with a thickness of $3.0mm$. The flow passes through a moisture-resistant heater with $7.7kW$ power and $300^{o}C$ maximum temperature, in order to heat up the dry air during the dehydration process or to preheat the humid air during the hydration process. After the heater, the pressure of the flow is measured by a pressure sensor with an accuracy of $\pm 0.5\%$. Temperature is also measured at the inlet and outlet of the reactor with the same T-type of thermocouple as mentioned before. At the outlet, the humidity is measured by the same type of humidity sensor as at the inlet. The outlet of each reactor segment is connected to a check valve and then to the exhaust vent. The purpose of these check valves is to close the outlet when there is no flow after the experiments, to prevent any moisture being exchanged between the surroundings and the reactor segments via the outlet. A
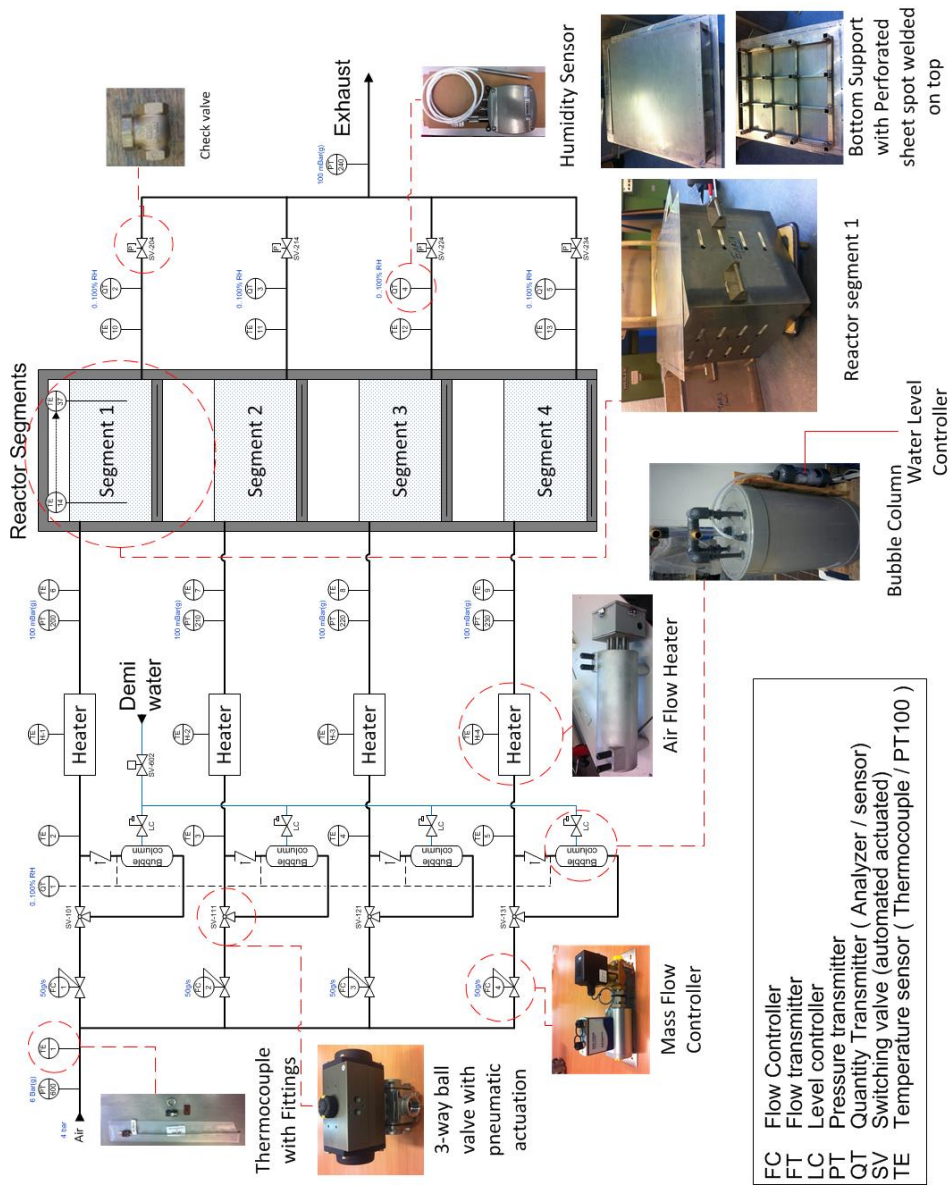
Figure 6.4: Schematic view of system.

picture of the realized setup is shown in Figure 6.5.

A bubble column is designed and built in the TUe workshop to humidify the inlet air to the reactor during the discharge process. The water level is set and maintained in order to achieve the desired relative humidity at the outlet. The water level inside the tank can be maintained with a floater valve. The valve is

Figure 6.5: Picture of realized system.

connected to a water supply system, which consists of a pump connected to a demineralized water tank. The bubble column can humidify an air flow rate of $50g/s$.

6.4 Experiments

The experiments are carried out with the pilot setup for de/re-hydration of the material beds in the segments. The experimental results of one dehydration (charging mode) and one rehydration (discharging mode) are discussed in this section. The experimental conditions for these two experiments are presented in Table 6.2.

parameter	unit	dehydration	rehydration
air flow rate	$[g/s]$	33	50
heater temperature	$[^oC]$	190	off
duration	$[h]$	7	18

Table 6.2: Operational conditions for the de/re-hydration experiments (values are for each segment).

The temperatures inside the bed and at the inlet and outlet of segment 1, mea-

sured during the dehydration, are shown in Figure 6.6a. As can be seen, the temperature front proceeds through the bed from the top (level 4) to the bottom (level 1). Because there is no material in level 4, the temperature follows the exact same trend as the inlet temperature, and no endothermic reaction is observed. In other levels, steps can be seen in the temperature curves, which are caused by the energy used to dehydrate zeolite and release water.
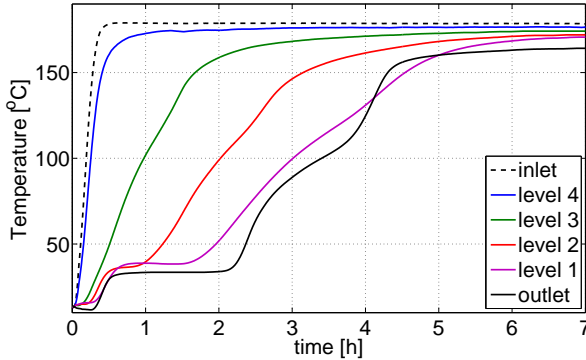
(a) Temperature at the inlet, outlet and center
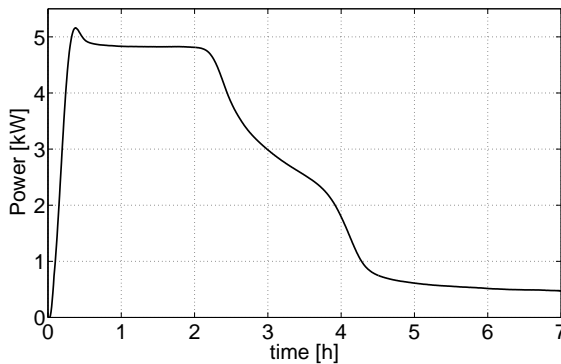
(b) Thermal power transferred to the reactor.

Figure 6.6: Results of the dehydration experiment in segment 1.

The thermal power transferred to the reactor is calculated based on $\dot{Q} = \dot{m}C_p(T_{out} - Tin)$ and is shown in Figure 6.6b. The average thermal power during 7 hours is around $2.47kW$, and the total energy is $17.29kWh$. As can be seen, most of the reaction is finished after 5 hours. The average power and total energy transferred to the reactor during the first 5 hours are $3.25kW$ and $16.24kWh$, respectively. Therefore, it is more efficient to stop the reaction after 5 hours.

The reactor is cooled down to the ambient temperature in the lab after the dehydration experiment, while the energy remains stored in the material. During the subsequent rehydration experiment in the pilot setup, air is directed to the

humidifier to provide humid air. The humid air flows through the bed in order to rehydrate the material bed, release the stored energy and extract it in the form of thermal energy. The temperatures measured inside the bed and at the inlet and outlet of segment 1 during hydration are shown in Figure 6.7. As can be seen, the inlet temperature drops to around $10^o C$ because of the evaporation in the bubble column. The inlet humid cold air reacts with the charged material and releases heat. This can be seen in the form of a temperature rise in the bed. The reaction front passes through the bed as time passes. When the reaction is complete the temperature drops to the temperature of the cold inlet air.
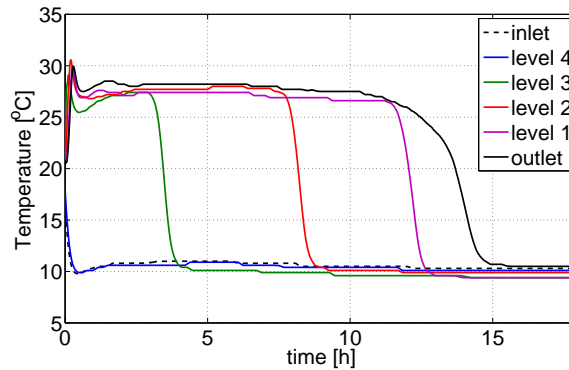
Figure 6.7: Temperature at the inlet, outlet and center of the reactor segment 1 during the hydration experiment.

The same rehydration experiment is performed in the other segments in parallel with segment 1. The inlet and out temperature of the four segments are measured and shown in Figure 6.8a. The inlet temperature is the average of the measured temperatures at all inlets of the segments, which are almost equal and are around $10^o C$. During hydration, humid air produced in the humidifier goes through the heater before entering the reactor. The system is designed in this way to provide the possibility of performing hydration experiments at an elevated inflow temperature. However, such experiments are not done in this work. In the present hydration experiment, the temperature increase in the segments is around $18^o C$. This temperature increase is lower than what is expected (around $20^o C$), which is probably because of a lower humidity generation in the bubble columns.

The humidity is also measured at the inlet and outlet of the four segments. The results are shown in Figure 6.8b. The measured humidity at the outlet of each segment is almost zero during the first 10 hours, since the entire water content in the inflow humid air is adsorbed by the material bed. After 10 hours, the humidity rises gradually to the same humidity as the inlet. The average inlet humidity is around $5.2g$ of water per kg of air. However, a higher humidity of around $7g/kg$ is expected at the inlet. This could be caused by a higher absolute pressure inside the humidifiers, which leads to a lower water content in the

provided humid air.
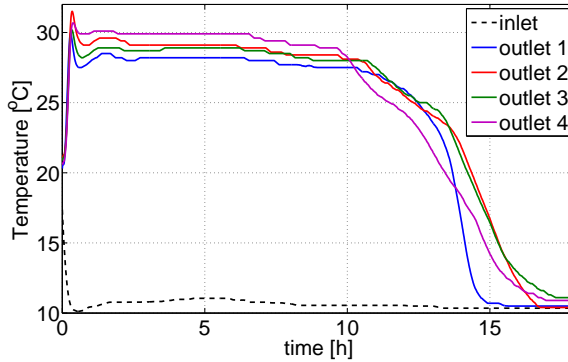
(a) temperature
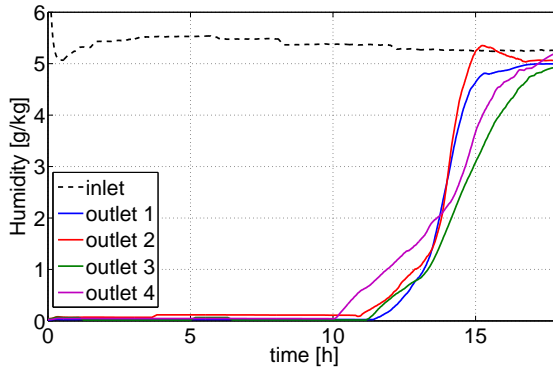
(b) humidity

Figure 6.8: Temperature and humidity at the inlet and outlet of the four reactor segments during the hydration experiment.

Pressure is measured at the inlet and outlet of the four segments, and results are shown in Figure 6.9. The pressure is also measured at the exhaust of the segments, and almost equals atmospheric pressure. Note that the pressure drop stays almost constant during the experiment, which means that swelling of the zeolite particles does not occur. The measured pressures slightly drop at the end of the experiment which can be related to the temperature drop at the end of the run. The average pressure drop over the bed in each segment is around $30Pa$. However, the biggest pressure drop in the system is over the heater. The pressure before the heater is measured and it is around $0.2bar$ at an air flow rate of $50g/s$. This large pressure can explain the lower humidity provided by the bubble column as observed. In addition, the weakest point of the pilot, which prevents us from boosting the flow rate and subsequently the power, is the bubble column. The bubble column is the component which needs to handle the highest pressure,

but seems not safe for that. For future research, it is important to strengthen the bubble columns.
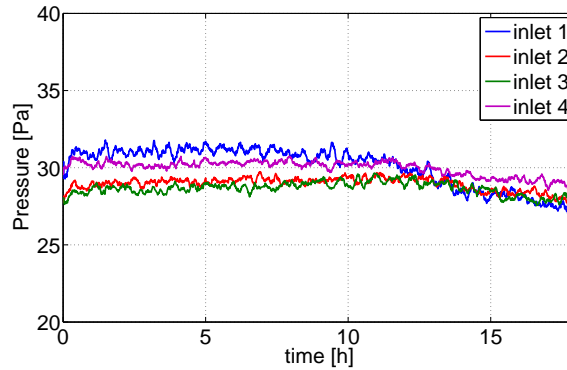
Figure 6.9: Pressure at the inlet of the four segments during the hydration experiment.

The released power from the segments during the rehydration experiment is calculated based on $P = \dot{m}C_p(T_{out} - Tin)$. The results are shown in Figure 6.10. As can be seen, A high constant power of around $0.9kW$ is generated by each segment during the first 10 hours of the experiment. After that, the powers drop gradually, and they reach zero at around 17.5 hour. The power for segment 1 drops sharply and is back to zero after around 15 hours, which is the fastest among all the segments. The reproducibility of these results still needs to be investigated. The total maximum power generated by the pilot is around $3.6kW$, which lasts for almost 10 hours.
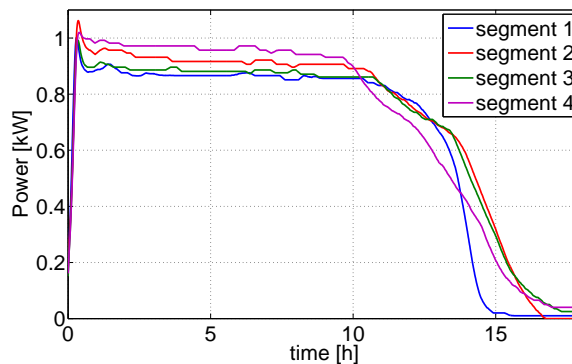
Figure 6.10: Thermal power released from the four segments during the hydration experiment.

The released energy and average power of each segment are calculated from the results presented in Figure 6.10. These terms are calculated for two time in-

tervals: from the start till 18 hours (the end) and from the start till 10 hours. The results are presented in Table 6.3. Almost 70 to 75 % of the total energy is released during the first 10 hours with high constant power (around $0.9kW$). In a real system, each segment should run for 10 hours individually to provide a constant power, and the energy associated with the last 5 to 8 hours can be recovered to the subsequent segment by running them in series. In addition, by considering the total energy supplied to segment 1 during the dehydration experiment (about $17.29kWh$ as discussed previously in this section), a total efficiency (energy released during rehydration divided by energy supplied during dehydration) of around 67% can be calculated.

parameter	unit	1	2	3	4	average
released energy until 18 h	$[kWh]$	11.69	12.86	12.44	12.74	12.43
average power until 18 h	$[kW]$	0.65	0.71	0.69	0.71	0.69
released energy until 10 h	$[kWh]$	8.63	9.15	8.75	9.50	9.01
average power until 10 h	$[kW]$	0.86	0.91	0.87	0.95	0.90
Energy density of material	$[kWh/m^3]$	187	206	199	203	198
Energy density of reactor	$[kWh/m^3]$	102	112	108	111	108

Table 6.3: Energy content and energy density of the segments.

Based on the total released energy and the volume of the material bed and the reactor segment, the energy densities on basis of the material and the reactor are calculated. An average energy density of $198kWh/m^3$ and $108kWh/m^3$ are calculated for material and reactor, respectively. The energy density of the reactor can be improved to almost $145kWh/m^3$, by filling more material in the top layer of the reactor. This means that the empty space at the top of the reactor, which is placed as the header distributor, will shrink, but this probably would not lead to less uniform flow through the bed. A much higher reactor energy density (close to the material energy density) will be ultimately achieved by removing the both empty spaces at the top and bottom of the reactor, in case the formation of non-reactive zones in the reactor can be avoided.

6.5   Conclusion

A large scale high power pilot is realized, consisting of four segments. The volume of each reactor segment (including empty header spaces) is $114.75L$, and each segment contains $62.5L$ of material. The total amount of zeolite 13XBF material in the segments is about $170kg$ ($250L$). Experiments are performed on the pilot in order to determine the energy storage density and to measure the power. For the charging process an inlet temperature of around 190^oC is used, and for the discharging process a water vapor pressure of around $1kPa$ ($5g$ of water per kg of air) at a temperature of about 10^oC is used. Average energy densities of $198kWh/m^3$ and $108kWh/m^3$ are calculated for material and reactor, respectively.

Each segment can be charged with about $17kWh$ (including losses) during 7 hours. Reducing the charging period to 5 hours, each segment is charged with $16kWh$, approximately, which is reasonably close to its maximum charging capacity. The total energy released during the discharge process is about $12kWh$, which is almost 70% of the supplied energy during 7 hours of charging process.

A maximum power of $0.9kW$ is achieved by each segment, which leads to a combined power of about $3.6kW$ lasting for almost 10 hours. This power can be improved by reducing the pressure drop over the system, and hence, increasing the humidity generated in the humidifier. During the first 10 hours of the discharge process, 70 to 75% of the total energy is released with a constant high power, and the rest is released during the final 5 to 8 hours of the discharge process where the power is gradually declining.

The pressure drop over the bed is only $30Pa$. Since the pressure drop over the bed is found to be small, the pressure drops in piping and over heat exchangers seems to be critical, in a real system. The largest pressure drop in the pilot setup is over the heater, which would not be part of a real thermochemical heat storage system.

7

ACCOMPLISHMENTS AND CONCLUSIONS

7.1 Multi-level approach

A lab-scale reactor setup is realized, which is an open system working with a packed bed reactor filled with zeolite 13XBF as Thermochemical Material (TCM). The adsorption reaction between water vapor in gas phase and zeolite 13XBF in solid phase is modelled by a Linear Driving Force (LDF) model, in combination with a Langmuir-Freundlich expression for the equilibrium isotherm. The parameters of the material model are determined from experimental data, and the enthalpy of the reaction is derived by using the van't Hoff equation.

A numerical reactor model is developed to simulate the test setup, incorporating the material model, and considering the heat losses from the side wall of the reactor by heat resistances in the radial direction. The calculated heat fluxes based on the experimental and numerical results are in good agreement, except for some deviations for the thermal output power at the end of the discharge process. The numerically calculated power decreases faster than the experimentally determined power. The same happens for the difference between the calculated and measured water vapor concentrations at the outlet of the reactor. This effect is related to a faster completion of the reaction in the near wall region than in the center of the reactor in the experiments, allowing vapor to pass in the near-wall region, while the reaction in the center is still ongoing. This shows that the radial effects at the inside wall of the reactor play an important role in predicting proper values for the dynamic thermal performance.

By the help of the model, the effects of the material performance and reactor design on the performance of an up-scaled system are studied. It is found that a larger kinetics coefficient leads to a higher efficiency. However, this effect is only significant below a threshold value of the kinetics coefficient, which for the case under study is found to be about $0.001 s^{-1}$. For slow reactions (smaller values of the kinetics coefficient), the residence time should be increased (and hence the

flow rate should be decreased) to achieve a higher efficiency.

7.2 Material Performance

Attempts have been made to stabilize calcium chloride, as a promising TCM, against overhydration and associated loss of porosity caused by agglomeration, during the hydration. The applied stabilization methods are impregnation in expanded natural graphite and in vermiculite, and encapsulation with ethyl cellulose. Degradation of the other features of the salt, such as fast kinetics and high energy storage density, caused by the applied stabilization methods is studied. Characterization of the calcium chloride-based TCMs is carried out by Thermo-Gravimetric Analysis (TGA) and Differential Scanning Calorimetry (DSC) methods in a Simultaneous Thermal Analysis (STA) apparatus.

In general, a strong relation between conversion rate and sample mass is observed. This suggests that the hydration reaction of calcium chloride is a diffusion-limited process. The hydration reaction rate for impregnated materials is similar to that of pure salt. Interestingly, the encapsulated material shows the fastest rehydration among all the materials.

Sample size is an important parameter for the performance of the material, specifically the kinetics of the reaction. Since the kinetics is important to the global performance of the thermochemical heat storage system (chapter 2), it is important to find the optimum pellet size for the material being used in the system. A small pellet size leads to a fast reaction in the material bed, and hence, higher power and efficiency. A large pellet size leads to a lower pressure drop over the material bed, and hence, higher COP. The average kinetics coefficient of the reaction is calculated for the pure and encapsulated materials based on the LDF model. The kinetics coefficient shows dependency on the sample mass. This dependency is smaller for larger samples. The average kinetics coefficient is roughly in the order of $10^{-3}s^{-1}$ and $10^{-4}s^{-1}$ for small (about $2mg$) and large (about $20mg$) sample masses, respectively. In general, it seems that the kinetics of the hydration reaction of the calcium chloride based materials can be expressed by the LDF model for samples larger than $10mg$.

The energy density of the encapsulated material is about 24% of the pure material, which is the lowest among all the materials. This low energy density is caused by the low density of the inert material. The energy densities of the impregnated graphite and vermiculite are, respectively, around 35% and 30% of the pure salt. The salt content (salt to sample mass ratio) of the impregnated vermiculite material is improved from $68wt\%$ to $86wt\%$ by a second impregnation. That leads to an energy density of about $1.2GJ/m^3$ (for a water vapor pressure of $1.3kPa$ and temperature of 20^oC), which is about 70% of the pure salt (with $60-70\%$ void fraction). The energy density of the twice impregnated graphite material is not measured experimentally, but it is expected to be the highest among all the materials, since the salt content is around $87wt\%$.

The impregnated samples show overhydration, allowing the contained salt to be washed out. Subsequent dehydration of the sample leads to an agglomer-

ated structure similar to the dehydrated pure salt, which reduces vapor transport through the structure. The structure of the graphite host matrix (probably with a part of the salt content still inside) is left intact, unlike the vermiculite sample, which distorted after hydration and a paste-like mixture is formed. It has been seen that the agglomeration is avoided in the encapsulated material.

However, the stability of materials at low temperatures around ambient temperature (for example 20^oC, which is used here) is only an issue during the initial part of the discharge process. For a system intended for domestic purposes, the inflow temperature needs to be increased to above 40^oC in order to achieve the required outflow temperature which is realized by the air-to-air heat exchanger in the system(chapter 5). For calcium chloride, the overhydration, and hence, the agglomeration is not an issue at temperatures above 40^oC (and water vapor pressure of $1.3kPa$). Having an elevated inlet temperature to the reactor means that the material bed reacts at the elevated temperature, during most of the discharge process. Only during the initial part of the discharge process, the temperature is below the elevated inlet temperature, when the material bed still needs to be heated up. This period is in the order of hours depending on the configuration of the system, while the overhydration of the material is much slower. This suggests that the overhydration problem can be tackled with innovative solutions. For instance, the inflow can contain less humidity during this starting period or a more stable material can be placed at the top layer of the reactor. Nevertheless, these measures might lead to a more complicated and more expensive system. In addition, it should be noted that the material might face the overhydration condition anyway, if a failure such as leakage occurs in the system.

7.3   Reactor design

For the detailed analysis of the reactor including the radial effects at the inside wall, a sophisticated 2D model of the transport phenomena occurring in the reactor is developed. The model is validated using experimental thermal analysis from a lab-scale reactor setup. The distribution of moisture content in the material is determined by an MRI setup. By comparing the measured pressure drop over the bed to the model results, good agreement is found for the Ergun equation with modified constants. However, the effect of particle size distribution on the average bed porosity must be taken into account.

The velocity is measured below the bed and wall channelling is observed. An increase in wall channelling was found for low flow rates and smaller particle diameters. The best representative model for this behaviour is found to be the Brinkman extension to the Darcy–Forchheimer equation in combination with an effective viscosity expression (dependent on both reactor Reynolds number and particle Reynolds number) and a radial porosity profile.

The moisture content in the material bed is measured by the MRI technique as a function of time and position in the reactor. The effects of flow rate and particle diameter on the shape of the moisture front are studied and compared to the numerical model for the benchmark case. From this analysis, the optimal values

of the mass dispersion parameters are determined. Dependence of the dispersion parameters on the Peclet number is validated. Further investigation is needed in order to generalize and quantify this dependency for a range of conditions. The best way to perform experiments for such an investigation is to measure the temperature in the bed simultaneously during the moisture content measurement by the MRI technique.

Reasonable agreements between the temperatures and concentrations from the experiment and numerical model during hydration and dehydration are found. The influence of the distribution of the initial state of charge in the bed on the performance of the reactor is found to be significant. Therefore, the final state of charge of the zeolite bed as a function of the radial and axial coordinate obtained after dehydration is used as an initial condition of the hydration simulation. It confirms the importance of the durations of the charging and discharging processes.

A parameter study is done on the effect of dehydration and rehydration duration on the average power and total efficiency of the reactor. Optimum operating conditions, and durations of charging and discharging processes are determined. The effect of bed diameter-to-height aspect ratio, ranging from 0.5 to 3.0, on the efficiency of the reactor is found to be negligible. As expected, the COP increases continuously by increasing the aspect ratio, because of smaller pressure drop over a bed with larger bed diameter-to-height aspect ratio.

7.4 System improvement

Keeping the reaction zone (the part of the material which participates in and/or is affected by the reaction) small is important for the performance of the system. Segmentation is introduced as a method to reduce the reaction zone, to make the system less inertial, more controllable and efficient. By segmentation, the material is packed in separate reactor segments and only one segment is run at a time. The segmentation concept provides simplicity and low auxiliary energy need of the packed bed reactor design, while also meeting the limited reaction zone requirement. In this way, it is possible to run the segments in sequence with a constant power, while providing the required average demand. The produced energy can be stored in a short-term heat storage water tank, to provide peak power.

An open sorption heat storage system based on segmented packed beds of zeolite is developed and realized, in order to provide hot tap water. The system consists of a bubble column humidifier, a sorption reactor, an air-to-water heat exchanger in a water vessel and an air-to-air heat exchanger as recuperator. By implementing the air-to-air heat exchanger in order to recuperate the heat in the outflow of the system to preheat the inlet humid air, the 60^oC temperature requirement for hot tap water is achieved. The system test setup is modelled numerically and is validated by the experimental results. The model is used to establish a complete energy map of an up-scaled thermochemical heat storage system.

When the reaction front reaches the bottom of the bed in the near-wall region, the thermal output power reduces gradually, until the whole bed has reacted. During this period, which is denoted here as the "tail period", a lower reaction power is produced compared with the average power of the reactor. The energy present in the tail period of the discharge phase cannot be utilized because of the low power. Therefore, the system efficiency is higher in the case the discharge process stops before the tail period compared to the case in which the discharge process continues till the end. However, stopping the discharge of a segment before the tail means losing the energy associated with the tail period, and this leads to a lower energy density for the system. The Subsequent Heat Recovery (SHR) strategy is proposed, in order to recover the heat produced in one segment during its tail period to the subsequent segment by running them in series. By the help of the model, it is shown that the extracted energy from a segment can be increased by around 20%.

7.5   Pilot realization

A large scale high power pilot is realized, based on the segmentation concept. The total amount of zeolite 13XBF material in the four segments is about $170kg$ ($250L$). Experiments are performed on the pilot in order to determine the energy storage density and to demonstrate the power. For the charging process an inlet temperature of around 190^oC is used, and for the discharging process a water vapor pressure of around $1kPa$ ($5g$ of water per kg of air) at the temperature of about 10^oC is used. Average energy densities of $198kWh/m^3$ and $108kWh/m^3$ are calculated for material and reactor, respectively. The energy density of the reactor can be improved by filling more material in the reactor, but it needs to be checked whether this will not cause unequal flow distribution.

The total energy released during the discharge process is about $50kWh$, which is almost 70% of the supplied energy during the charging process. This can be improved to 80% by optimizing the duration of the charging process. A maximum total power of $3.6kW$ can be achieved, lasting for almost 10 hours. This power can be improved by reducing the pressure drop over the system, and hence, the humidity generated in the humidifier. During the first 10 hours of the discharge process, about 75% of the total energy is released with a constant high power. The rest of the energy is released during the final 5 to 8 hours of the discharge process by a gradually declining power, which can be recovered to the next segment by the earlier introduced SHR strategy, but this still needs to be tested experimentally.

Thanks to a good reactor design, the pressure drop over the bed is very small (about $30Pa$), which results in a large reactor COP. Since the pressure drop over the bed is found to be small, the critical pressure drops in a real system seem to be the ones over other parts of the system, such as piping and heat exchangers. The largest pressure drop in the pilot is over the heater, which would not be part of a real thermochemical heat storage system. Therefore, high system COP is achievable in a real system.

Bibliography

[1] Saheb, Y. Modernising building energy codes to secure our global energy future. The IEA Policy Pathway series, 2011.

[2] (ESTTP), E. S. T. T. P. Solar heating and cooling for a sustainable energy future in europe (revised). *Renewable Energy House*, 2009.

[3] Rindt, C., Lan, S., Gaeini, M., Zhang, H., Nedea, S., and Smeulders, D. M. Phase change materials and thermochemical materials for large-scale energy storage. In *Continuous Media with Microstructure 2*, pages 187–197. Springer, 2016.

[4] Koninklijk nederlands meteorologisch instituut (knmi). projects.knmi.nl, 2016.

[5] Centraal bureau voor de statistiek (cbs). statline.cbs.nl, 2016.

[6] Tatsidjodoung, P., Le Pierrès, N., and Luo, L. A review of potential materials for thermal energy storage in building applications. *Renewable and Sustainable Energy Reviews*, 18:327–349, 2013.

[7] Aydin, D., Casey, S. P., and Riffat, S. The latest advancements on thermochemical heat storage systems. *Renewable and Sustainable Energy Reviews*, 41:356–367, 2015.

[8] N'Tsoukpoe, K. E., Liu, H., Pierrès, N. L., and Luo, L. A review on long-term sorption solar energy storage. *Renewable and Sustainable Energy Reviews*, 13(9):2385 – 2396, 2009.

[9] Zondag, H., Kikkert, B., Smeding, S., de Boer, R., and Bakker, M. Prototype thermochemical heat storage with open reactor system. *Applied Energy*, 109:360 – 365, 2013.

[10] Yu, N., Wang, R., and Wang, L. Sorption thermal storage for solar energy. *Progress in Energy and Combustion Science*, 39(5):489 – 514, 2013.

[11] Michel, B., Neveu, P., and Mazet, N. Comparison of closed and open thermochemical processes, for long-term thermal energy storage applications. *Energy*, 72:702–716, 2014.

[12] Zondag, H., Schuitema, R., Bleijendaal, L., Gores, J. C., van Essen, V., Van Helden, W., and Bakker, M. R&d of thermochemical reactor concepts to enable seasonal heat storage of solar energy in residential houses. In *ASME 2009 3rd International Conference on Energy Sustainability collocated with the Heat Transfer and InterPACK09 Conferences*, pages 831–837. American Society of Mechanical Engineers, 2009.

[13] Zondag, H., Kalbasenka, A., van Essen, M., Bleijendaal, L., Schuitema, R., van Helden, W., and Krosse, L. First studies in reactor concepts for thermochemical storage. In *Proc. Eurosun*, 2008.

[14] Jänchen, J., Ackermann, D., Stach, H., and Brösicke, W. Studies of the water adsorption on zeolites and modified mesoporous materials for seasonal storage of solar heat. *Solar Energy*, 76(1):339–344, 2004.

[15] N'Tsoukpoe, K. E., Schmidt, T., Rammelberg, H. U., Watts, B. A., and Ruck, W. K. A systematic multi-step screening of numerous salt hydrates for low temperature thermochemical energy storage. *Applied Energy*, 124:1 – 16, 2014.

[16] Alibaba.com.

[17] Jänchen, J., Schumann, K., Thrun, E., Brandt, A., Unger, B., and Hellwig, U. Preparation, hydrothermal stability and thermal adsorption storage properties of binderless zeolite beads. *International Journal of Low-Carbon Technologies*, 7(4):275–279, 2012.

[18] Scapino, L., Zondag, H. A., Van Bael, J., Diriken, J., and Rindt, C. C. Sorption heat storage for long-term low-temperature applications: A review on the advancements at material and prototype scale. *Applied Energy*, 190:920–948, 2017.

[19] Sun, L., Amar, N. B., and Meunier, F. Numerical study on coupled heat and mass transfers in an absorber with external fluid heating. *Heat recovery systems and CHP*, 15(1):19–29, 1995.

[20] Amar, N. B., Sun, L., and Meunier, F. Numerical analysis of adsorptive temperature wave regenerative heat pump. *Applied Thermal Engineering*, 16(5):405–418, 1996.

[21] Zhang, L. Z. and Wang, L. Effects of coupled heat and mass transfers in adsorbent on the performance of a waste heat adsorption cooling unit. *Applied Thermal Engineering*, 19(2):195–215, 1999.

[22] Duquesne, M., Toutain, J., Sempey, A., Ginestet, S., and del Barrio, E. P. Modeling of a nonlinear thermochemical energy storage by adsorption on zeolites. *Applied Thermal Engineering*, 71(1):469–480, 2014.

[23] Mette, B., Kerskes, H., Drück, H., and Müller-Steinhagen, H. Experimental and numerical investigations on the water vapor adsorption isotherms and kinetics of binderless zeolite 13x. *International Journal of Heat and Mass Transfer*, 71:555–561, 2014.

[24] Lan, S., Zondag, H., van Steenhoven, A., and Rindt, C. Kinetic study of the dehydration reaction of lithium sulfate monohydrate crystals using microscopy and modeling. *Thermochimica Acta*, 621:44–55, 2015.

[25] Ahn, H. and Lee, C.-H. Effects of capillary condensation on adsorption and thermal desorption dynamics of water in zeolite 13x and layered beds. *Chemical engineering science*, 59(13):2727–2743, 2004.

[26] Dawoud, B., Vedder, U., Amer, E.-H., and Dunne, S. Non-isothermal adsorption kinetics of water vapour into a consolidated zeolite layer. *International Journal of Heat and Mass Transfer*, 50(11):2190–2199, 2007.

[27] Sircar, S. Linear-driving-force model for non-isothermal gas adsorption kinetics. *Journal of the Chemical Society, Faraday Transactions 1: Physical Chemistry in Condensed Phases*, 79(4):785–796, 1983.

[28] Sircar, S. and Hufton, J. Why does the linear driving force model for adsorption kinetics work? *Adsorption*, 6(2):137–147, 2000.

[29] Schumann, K., Unger, B., Brandt, A., and Scheffler, F. Investigation on the pore structure of binderless zeolite 13x shapes. *Microporous and Mesoporous Materials*, 154:119 – 123, 2012. Special Issue: Characterisation of Porous Solids {IX}.

[30] Glueckauf, E. Theory of chromatography. part 10.-formulae for diffusion into spheres and their application to chromatography. *Transactions of the Faraday Society*, 51:1540–1551, 1955.

[31] Ruthven, D. M. *Principles of adsorption and adsorption processes*. John Wiley & Sons, 1984.

[32] Wakao, N. and Funazkri, T. Effect of fluid dispersion coefficients on particle-to-fluid mass transfer coefficients in packed beds: correlation of sherwood numbers. *Chemical Engineering Science*, 33(10):1375–1384, 1978.

[33] Thomas, W. J. and Crittenden, B. D. *Adsorption technology and design*. Butterworth-Heinemann, 1998.

[34] Chapman, S. and Cowling, T. G. *The mathematical theory of non-uniform gases: an account of the kinetic theory of viscosity, thermal conduction and diffusion in gases*. Cambridge university press, 1970.

[35] Crank, J. *The mathematics of diffusion*. Oxford university press, 1979.

[36] Sing, K. S. Reporting physisorption data for gas/solid systems with special reference to the determination of surface area and porosity (recommendations 1984). *Pure and applied chemistry*, 57(4):603–619, 1985.

[37] Ryu, Y. K., Lee, S. J., Kim, J. W., and Leef, C.-H. Adsorption equilibrium and kinetics of h2o on zeolite 13x. *Korean Journal of Chemical Engineering*, 18(4):525–530, 2001.

[38] Do, D. D. *Adsorption analysis*. World Scientific, 1998.

[39] Bering, B., Dubinin, M., and Serpinsky, V. Theory of volume filling for vapor adsorption. *Journal of colloid and interface science*, 21(4):378–393, 1966.

[40] Delgado, J. A critical review of dispersion in packed beds. *Heat and mass transfer*, 42(4):279–310, 2006.

[41] Kandula, M. On the effective thermal conductivity of porous packed beds with uniform spherical particles. *Journal of Porous Media*, 14(10):919–926, 2011.

[42] Ahn, H., Kim, M.-B., and Lee, C.-H. Effects of heat-transfer coefficients on thermal dynamics in a near-adiabatic fixed bed. *Separation science and technology*, 39(11):2627–2654, 2004.

[43] Michel, B., Mazet, N., and Neveu, P. Experimental investigation of an innovative thermochemical process operating with a hydrate salt and moist air for thermal storage of solar energy: Global performance. *Applied Energy*, 129:177 – 186, 2014.

[44] Ferchaud, C. *Experimental study of salt hydrates for thermochemical seasonal heat storage*. PhD thesis, Ph. D. thesis) Eindhoven University of Technology, 2016.

[45] N'Tsoukpoe, K. E., Rammelberg, H. U., Lele, A. F., Korhammer, K., Watts, B. A., Schmidt, T., and Ruck, W. K. A review on the use of calcium chloride in applied thermal engineering. *Applied Thermal Engineering*, 75:513 – 531, 2015.

[46] DOW. Calcium chloride handbook. *The Dow Chemical Company*, 2003.

[47] Wagman, D. D., Evans, W. H., Parker, V. B., Schumm, R. H., and Halow, I. The nbs tables of chemical thermodynamic properties. Technical report, DTIC Document, 1982.

[48] Rammelberg, H. U., Myrau, M., Schmidt, T., and Ruck, W. An optimization of salt hydrates for thermochemical heat storage. In *IMPRES 2013, Fukuoka, 04.-06*. 2013.

[49] Iyimen-Schwarz, Z. and Lechner, M. Energiespeicherung durch chemische reaktionen. i. dsc-messungen zur quantitativen verfolgung der enthalpieänderungen von speicherstoffen für die hin-und rückreaktion. *Thermochimica Acta*, 68(2):349 – 361, 1983.

[50] Aristov, Y. I., Tokarev, M. M., Cacciola, G., and Restuccia, G. Selective water sorbents for multiple applications, 1. cacl2 confined in mesopores of silica gel: Sorption properties. *Reaction Kinetics and Catalysis Letters*, 59(2):325–333, 1996.

[51] Ristić, A., Maučec, D., Henninger, S. K., and Kaučič, V. New two-component water sorbent cacl2 - fekil2 for solar thermal energy storage. *Microporous and Mesoporous Materials*, 164:266–272, 2012.

[52] Levitskij, E., Aristov, Y., Tokarev, M., and Parmon, V. Chemical heat accumulators: A new approach to accumulating low potential heat. *Solar Energy Materials and Solar Cells*, 44(3):219 – 235, 1996.

[53] Zhu, D., Wu, H., and Wang, S. Experimental study on composite silica gel supported cacl2 sorbent for low grade heat storage. *International Journal of Thermal Sciences*, 45(8):804 – 813, 2006.

[54] Jänchen, J., Ackermann, D., Weiler, E., Stach, H., and Brösicke, W. Thermochemical storage of low temperature heat by zeolites; sapo's and impregnated active carbon. In *7 th Workshop of IEA/ECES, annex*, volume 17, 2004.

[55] Kerskes, H., Mette, B., Asenbeck, S., Drück, H., and Müller-Steinhagen, H. Experimental and numerical investigations on thermo-chemical heat stoarge. In *Proceedings of the EUROSUN*, 2010.

[56] Aristov, Y. I. Novel materials for adsorptive heat pumping and storage: Screening and nanotailoring of sorption properties. *JOURNAL OF CHEMICAL ENGINEERING OF JAPAN*, 40(13):1242–1251, 2007.

[57] Milián, Y. E., Gutiérrez, A., Grágeda, M., and Ushak, S. A review on encapsulation techniques for inorganic phase change materials and the influence on their thermophysical properties. *Renewable and Sustainable Energy Reviews*, 73:983–999, 2017.

[58] Cuypers, R., de Jong, A., Eversdijk, J., van't Spijker, J., Oversloot, H., Ingenhut, B., Cremers, R., and Papen-Botterhuis, N. Microencapsulation of salts for enhanced thermochemical storage materials. In *40th Annual Meeting and Exposition of the Controlled Release Society, 21-24 July 2013, Honolulu, Hawaii, USA, 1-2*, 2013.

[59] Lan, S., Zondag, H., van Steenhoven, A., and Rindt, C. An experimentally validated numerical model of interface advance of the lithium sulfate monohydrate dehydration reaction. *Journal of Thermal Analysis and Calorimetry*, 124(2):1109–1118, 2016.

[60] Korhammer, K., Druske, M.-M., Fopah-Lele, A., Rammelberg, H. U., Wegscheider, N., Opel, O., Osterland, T., and Ruck, W. Sorption and thermal characterization of composite materials based on chlorides for thermal energy storage. *Applied Energy*, 162:1462 – 1472, 2016.

[61] Vortmeyer, D. and Schuster, J. Evaluation of steady flow profiles in rectangular and circular packed beds by a variational method. *Chemical Engineering Science*, 38(10):1691 – 1699, 1983.

[62] Winterberg, M., Tsotsas, E., Krischke, A., and Vortmeyer, D. A simple and coherent set of coefficients for modelling of heat and mass transport with and without chemical reaction in tubes filled with spheres. *Chemical Engineering Science*, 55(5):967 – 979, 2000.

[63] Giese, M., Rottschäfer, K., and Vortmeyer, D. Measured and modeled superficial flow profiles in packed beds with liquid flow. *AIChE Journal*, 44(2):484–490, 1998.

[64] Punčochář, M. and Drahoš, J. Limits of applicability of capillary model for pressure drop correlation. *Chemical Engineering Science*, 55(18):3951 – 3954, 2000.

[65] Ergun, S. Fluid flow through packed columns. *Chem. Eng. Prog.*, 48:89–94, 1952.

[66] Nemec, D. and Levec, J. Flow through packed bed reactors: 1. single-phase flow. *Chemical Engineering Science*, 60(24):6947 – 6957, 2005.

[67] Mehta, D. and Hawley, M. Wall effect in packed columns. *Industrial & Engineering Chemistry Process Design and Development*, 8(2):280–282, 1969.

[68] Reichelt, W. Calculation of pressure-drop in spherical and cylindrical packings for single-phase flow. *Chemie Ingenieur Technik*, 44(18):1068, 1972.

[69] Eisfeld, B. and Schnitzlein, K. The influence of confining walls on the pressure drop in packed beds. *Chemical Engineering Science*, 56(14):4321 – 4329, 2001.

[70] Montillet, A., Akkari, E., and Comiti, J. About a correlating equation for predicting pressure drops through packed beds of spheres in a large range of reynolds numbers. *Chemical Engineering and Processing: Process Intensification*, 46(4):329 – 333, 2007.

[71] Cheng, N.-S. Wall effect on pressure drop in packed beds. *Powder Technology*, 210(3):261 – 266, 2011.

[72] Dixon, A. G. Correlations for wall and particle shape effects on fixed bed bulk voidage. *Canadian Journal of Chemical Engineering*, 66(5):705–708, 1988.

[73] Ribeiro, A., Neto, P., and Pinho, C. Mean porosity and pressure drop measurements in packed beds of monosized spheres: side wall effects. *International Review of Chemical Engineering*, 2(1):40–46, 2010.

[74] Einstein, A. A new determination of molecular dimensions. *Ann. Phys*, 19(2):289–306, 1906.

[75] Brinkman, H. A calculation of the viscous force exerted by a flowing fluid on a dense swarm of particles. *Applied Scientific Research*, 1(1):27–34, 1949.

[76] Bey, O. and Eigenberger, G. Fluid flow through catalyst filled tubes. *Chemical Engineering Science*, 52(8):1365 – 1376, 1997.

[77] Giese, M. *Strömung in porösen Medien unter Berücksichtigung effektiver Viskositäten*. 1998.

[78] Cohen, Y. and Metzner, A. Wall effects in laminar flow of fluids through packed beds. *AIChE Journal*, 27(5):705–715, 1981.

[79] Nield, D. Alternative model for wall effect in laminar flow of a fluid through a packed column. *AIChE Journal*, 29(4):688–689, 1983.

[80] Felice, R. D. and Gibilaro, L. Wall effects for the pressure drop in fixed beds. *Chemical Engineering Science*, 59(14):3037 – 3040, 2004.

[81] Kwapinski, W., Salem, K., Mewes, D., and Tsotsas, E. Thermal and flow effects during adsorption in conventional, diluted and annular packed beds. *Chemical Engineering Science*, 65(14):4250 – 4260, 2010.

[82] Digitron p200ul manometer, www.digitron.com/dig19-ismanometers.pdf.

[83] Tsi 8386 anemometer, www.tsi.com/1980321j-8384-86-velocicalc-plus.pdf.

[84] Donkers, P. A., Pel, L., and Adan, O. C. Dehydration/hydration of granular beds for thermal storage applications: A combined {NMR} and temperature study. *International Journal of Heat and Mass Transfer*, 105:826 – 830, 2017.

[85] Hornak, J. P. The Basics of NMR. *Department of Chemistry, Rochester Institute of Technology, Rochester, NY*, 2002.

[86] Callaghan, P. *Principles of Nuclear Magnetic Resonance Microscopy*. Oxford University Press, Oxford, 1 edition, 1994.

[87] Bejan, A. *Convection Heat Transfer: Fourth Edition*. John Wiley & Sons, Inc., 2013.

[88] Tsotsas, E. and SchlÃČÂijnder, E. On axial dispersion in packed beds with fluid flow. *Chemical Engineering and Processing: Process Intensification*, 24(1):15 – 31, 1988.

[89] Zehner, P. and Schlünder, E. U. Wärmeleitfähigkeit von schüttungen bei mäßigen temperaturen. *Chemie Ingenieur Technik*, 42(14):933–941, 1970.

[90] Tsotsas, E. Wärmeleitung und dispersion in durchströmten schüttungen. *VDI-Wärmeatlas*, 1997.

[91] Aris, R. and Amundson, N. R. Some remarks on longitudinal mixing or diffusion in fixed beds. *AIChE Journal*, 3(2):280–282, 1957.

[92] Cheng, P. and Vortmeyer, D. Transverse thermal dispersion and wall channelling in a packed bed with forced convective flow. *Chemical Engineering Science*, 43(9):2523 – 2532, 1988.

[93] Vortmeyer, D. and Haidegger, E. Discrimination of three approaches to evaluate heat fluxes for wall-cooled fixed bed chemical reactors. *Chemical Engineering Science*, 46(10):2651 – 2660, 1991.

[94] Givler, R. and Altobelli, S. A determination of the effective viscosity for the brinkman–forchheimer flow model. *Journal of Fluid Mechanics*, 258:355–370, 1994.

[95] Mette, B., Kerskes, H., Drück, H., and Müller-Steinhagen, H. New highly efficient regeneration process for thermochemical energy storage. *Applied Energy*, 109:352 – 359, 2013.

[96] Weber, R., Asenbeck, S., Kerskes, H., and Drück, H. Solspaces–testing and performance analysis of a segmented sorption store for solar thermal space heating. *Energy Procedia*, 91:250–258, 2016.

[97] Zettl, B., Englmair, G., and Steinmaurer, G. Development of a revolving drum reactor for open-sorption heat storage processes. *Applied Thermal Engineering*, 70(1):42 – 49, 2014.

[98] Johannes, K., Kuznik, F., Hubert, J.-L., Durier, F., and Obrecht, C. Design and characterisation of a high powered energy dense zeolite thermal energy storage system for buildings. *Applied Energy*, 159:80 – 86, 2015.

[99] England, E. S. T. Measurement of domestic hot water consumption in dwellings. *Monitoring/Housing professionals/Publications/Home (England)*, 2008.

[100] Bales, C., Gantenbein, P., Jaenig, D., Kerskes, H., Summer, K., van Essen, M., and Weber, R. Laboratory tests of chemical reactions and prototype sorption storage units. *A Report of IEA Solar Heating and Cooling programme-Task*, 32, 2008.

[101] de Boer, R., Smeding, S., Zondag, H., and Krol, G. Development of a prototype system for seasonal solar heat storage using an open sorption process. In *Eurotherm Seminar# 99, Advances in Thermal Energy Storage*, pages 28–30, 2014.

[102] Schnieders, J., Feist, W., and Rongen, L. Passive houses for different climate zones. *Energy and Buildings*, 105:71–87, 2015.

[103] Gaeini, M., Zondag, H., and Rindt, C. Effect of kinetics on the thermal performance of a sorption heat storage reactor. *Applied Thermal Engineering*, 102:520 – 531, 2016.

symbol	description	unit
A	cross-sectional area	$[m^2]$
b	isotherm model affinity constant	$[-]$
B	shape factor	$[-]$
c	concentration of water in gas phase	$[mol/m^3]$
C_P	specific heat capacity	$[J/kg.K]$
d	diameter	$[m]$
D	dispersion coefficient; bed diameter	$[m^2/s]$; $[m]$
ΔE	activation energy of desorption	$[J/mol]$
ΔH	adsorption enthalpy	$[J/mol]$
H	height of the bed	$[m]$
k	kinetics coefficient	$[s^{-1}]$
K	dispersion model parameter	$[-]$
L	loading; length	$[mol_{water}/mol_{salt}]$; $[m]$
m	mass	$[kg]$
M	molecular mass	$[kg/mol]$
n	isotherm model exponent constant	$[-]$
N	number of moles	$[mol]$
p	pressure	$[Pa]$
P	average reactor power	$[W]$
q	water loading in solid phase	$[mol/kg]$
Q	air flow rate	$[m^3/s]$
r	radial coordinate	$[m]$
R	reactor radius; heat resistance	$[m]$; $[m.K/W]$
S	heat transfer surface area	$[m^2]$
t	time	$[s]$
T	temperature	$[K]$
u	velocity	$[m/s]$
V	volume	$[m^3]$
z	axial coordinate	$[m]$

Table 7.1: List of Roman symbols

symbol	description	
α	isotherm model parameter; conversion; viscous term constant	$[-]$
β	particle to gas thermal conductivity ratio; inertial term constant	$[-]$
γ	driving force	$[-]$
δ	diffusivity	$[m^2/s]$
ϵ	porosity	$[-]$
η	efficiency of the reactor	$[-]$
θ	dimensionless time	$[-]$
λ	conductivity	$[W/m.K]$
Λ	thermal dispersion coefficient	$[W/m.K]$
μ	viscosity	$[Pa.s]$
ρ	density	$[kg/m^3]$
τ	tortuosity; residence time	$[-]; [s]$
ϕ	volumetric gas flow rate	$[m^3/s]$

Table 7.2: List of Greek symbols

symbol	description
a	air; air side of WV
amb	ambient
b	bed
c	core region; cold side of HE
deh	dehydration
eff	effective
eq	equilibrium
g	gas phase
h	heat; hot side of HE
HE	air-to-air heat exchanger
i	inner
in	inlet
ins	insulation layer
LDF	Linear Driving Force
m	mass
o	outer
out	outlet
p	particle; pipe
reh	rehydration
R	reactor body
s	solid phase
SS	stainless steel layer
tef	teflon layer
v	water vapor
w	water side of WV
WV	water vessel (air-to-water heat exchanger)

Table 7.3: List of subscript symbols

Summary

Thermochemical seasonal heat storage for the built environment: a multi-scale investigation

According to the International Energy Agency, the built environment is the sector with the largest energy use. In this sector, space heating and domestic hot water production are the largest single energy end-uses. To reduce fossil fuel consumption and reduce CO_2 emission, replacing fossil fuel by renewable energy is of high interest. In particular, solar energy is seen as a promising sustainable energy source for space heating and domestic hot water production in the built environment. However, for solar heating, the seasonal mismatch between solar supply and heating demand requires long term heat storage to reach high thermal solar fractions. Potentially good candidates for long term heat storage are thermochemical materials, TCMs. The reversible adsorption-desorption reactions, which are exothermic in the hydration direction and endothermic in the reverse dehydration direction, can be used to store heat. The technological maturity on thermochemical heat storage systems can be improved on three levels: material, reactor and system. Most of the research on heat storage is devoted to only one of these scales. However in order to develop an optimized thermochemical heat storage system, simultaneous investigation on all scales is required. In this work, a multi-scale approach is effectively used to investigate the thermochemical heat storage for the built environment.

On material scale, an optimized material should be prepared with enough stability, sufficiently fast kinetics to obtain the required power, and adequately high energy density. Calcium chloride salt hydrate, as a promising TCM, is tested in pure form, encapsulated in an inert material and impregnated in porous matrices. Samples of approximately $10 mg$ of the materials are tested in a TGA-DSC apparatus, in order to evaluate stability, cyclability, kinetics and energy density. Encapsulated calcium chloride showed high stability and fast kinetics with negligible decrease of energy density.

On reactor scale, a detailed understanding of the transport phenomena occurring in the reactor is needed, in order to evaluate the performance of the reactor, as the main part of the heat storage system. During the re/de-hydration process in a cylindrical packed bed reactor, the wall creates radial effects due to heat losses, flow channeling and non-uniform state of charge for the subse-

quent re/de-hydration. A detailed 2D model for the transport phenomena in a packed bed, considering also the radial terms, is developed. The model is validated using experimental data measured in a $1L$ lab-scale setup by comparing the pressure drop over the bed, velocity profile below the bed and temperature profile inside the bed. In addition, the concentration of adsorbed water is compared with unique experimental results from MRI experiments. An accurate validated model for the dynamic thermal performance of an adsorption bed on reactor scale is obtained, which is employed to understand the significance of the above mentioned effects and to present suggestions to optimize the charging and discharging process times, hence, to improve the performance of the reactor. In addition, it is shown that by implementing segmentation in the reactor design and, as such, reducing the size of the reactive part, the performance of the reactor can be improved.

On system scale, in order to investigate the performance of the system, an $8L$ lab-scale thermochemical heat storage system is designed and optimized for providing hot tap water. During the hydration process, humid air is introduced to the packed bed reactor filled with dehydrated zeolite 13X, and the released heat of adsorption heats up the air passing through the reactor. The hot outflow air is led to an air-to-water heat exchanger to provide hot tap water. The residual heat in the exhaust air is used to preheat the reactor inflow air in an air-to-air heat exchanger. The temperatures of all system components are measured, and the thermal powers and heat losses in the system are mapped. By employing air-to-air heat recovery in this way, a temperature of 60^oC is achieved, as required for hot tap water. Based on the energy map of the system, the efficiency of the system is improved by recovering heat from one segment to the subsequent segment in the process.

Finally, a proof-of-principle prototype is successfully built in order to demonstrate the feasibility of the thermochemical heat storage concept for application in the built environment. The prototype consists of four reactor segments of $62.5L$ each. It can provide a maximum constant power of around $4kW$ for 10 hours, or a stable average power of $1kW$ for 40 hours. By upscaling this system from 4 to 150 segments, this system can provide the heating demand of a typical passive house.

Acknowledgements

During my research, a number of students worked on their graduation or internship projects under my supervision. Their work has been a significant contribution to this project. Therefore, I would like to thank my students, in the order of graduation date, Erik de Jong (constructed the system setup), Cristina Sconosciuto (improved the system setup), Tim Spee (studied the options for material), Luuk Saris (improved the system model), Lars Joosten (constructed the segmented reactor), Chara Kassianidi (calibrated the TGA-DSC apparatus), Robbert Wind (improved the reactor model), Rashed Javed (constructed the prototype), Toon Rouws (performed the material experiments), Chris Kwikkers (tested the system setup) and Rens van Alebeek (tested the prototype).

I would like to thank people in the Energy Technology group, especially the secretary Linda Essink for helping in all the administrative matters, and all the former and current collogues, Junghan, Eldhose, Gokalp, Claire, Pim, Raluca, Manoj, Amar, Luca, Max, Mauro, Joy, Zhipeng, Esubalew, Maurice, Kees, Ernst, Valliappan, Steven, Cong, Jingqian, Leila, Sami, Stephanie and Remco. Especial thanks to Shuiquan and Huaichen.

I am grateful for encountering many wonderful friends in my life that makes it difficult to name them all. As I express my gratitude to all of my friends, I must never forget that the highest appreciation is not to utter words, but to live by them. Especial thanks to my good friends and my paranymphs in the doctoral defence ceremony Sara Motahari and Arash Pourtaherian.

I would like to take this opportunity to thank my parents for everything they have done for me. I am happy to have my father beside me to celebrate this achievement, and I feel the presence of my mother in my whole life.

At last, my best appreciations to Sara Nikouyeh who has always been there for me selflessly, and Alireza Gaeini for his unconditional support.

List of publications

Journal publications

- M. Gaeini, H.A. Zondag, and C.C.M. Rindt, Effect of kinetics on the thermal performance of a sorption heat storage reactor. *Applied Thermal Engineering*, 102, 520–531, 2016.

- M. Gaeini, H. Ouwerkerk, H.A. Zondag and C.C.M. Rindt, Development of a validated 2D model for flow, moisture and heat transport in a packed bed reactor using MRI experiment and a lab-scale reactor setup, submitted to *International Journal of Heat and Mass Transfer*.

- M. Gaeini, M.R. Javed, H. Ouwerkerk, H.A. Zondag and C.C.M. Rindt, Realization of a 4kW thermochemical segmented reactor in household scale for seasonal heat storage, submitted to *Energy Procedia*.

- M. Gaeini, H. Ouwerkerk, H.A. Zondag and C.C.M. Rindt, New efficient heat recovery in a thermochemical heat storage system with a segmented reactor for domestic hot tap water production, submitted to *Energy*.

- M. Gaeini, A.L. Rouws, H.A. Zondag and C.C.M. Rindt, Characterization of microencapsulated and impregnated porous host composite materials based on calcium chloride for thermochemical heat storage, submitted to *Applied Energy*.

- S. Lan, M. Gaeini, H.A. Zondag, A.A. van Steenhoven and C.C.M. Rindt, Direct numerical simulation of the thermal dehydration reaction in a TGA experiment, submitted to *Applied Thermal Engineering*.

- Y.M. Lau, K. Thiruvalluvan Sujatha, M. Gaeini, N.G. Deen and J.A.M. Kuipers, Experimental study of the bubble size distribution in a pseudo-2D bubble column, *Chemical Engineering Science*, 98, 203–211, 2013.

Other publications

- M. Gaeini, L. Joosten, H. Ouwerkerk, H.A. Zondag, and C.C.M. Rindt, Segmented open reactor concept for a thermochemical seasonal heat storage

system in the built environment, 10th International Renewable Energy Storage Conference (IRES 2016) , Dusseldorf, Germany, March 2016.

- M. Gaeini, L. Saris, H.A. Zondag, and C.C.M. Rindt, Improvement in performance of a thermochemical heat storage system by implementing an internal heat recovery system, Proceedings of The 13th International Conference on Energy Storage (IEA GREENSTOCK 2015), Beijing, China, May 2015.

- M. Gaeini, H.A. Zondag, and C.C.M. Rindt, Non-isothermal kinetics of zeolite water vapor adsorption into a packed bed lab scale thermochemical reactor, Proceedings of the 15th International Heat Transfer Conference (IHTC-15), Kyoto, Japan, August 2014.

- M. Gaeini, E.C.J. de Jong, H.A. Zondag, and C.C.M. Rindt, Design of a thermochemical heat storage system for tap water heating in the built environment, Proceedings of the Advances in Thermal Energy Storage conference (IEA EUROTHERM 99), Lleida, Spain, May 2014.

- C.C.M. Rindt, S. Lan, M. Gaeini, H. Zhang, S.V. Nedea and D.M.J. Smeulders, Continuous Media with Microstructure 2, chapter Phase Change Materials and Thermochemical Materials for Large-Scale Energy Storage, pages 187–197. Springer International Publishing, Cham, 2016.

- R. van Alebeek, M.A.J.M. Beving, M. Gaeini, C.C.M. Rindt and H.A. Zondag, Design and experimental investigation of a high power segmented zeolite 13X/water sorption energy storage system, The 4th Sustainable Thermal Energy Management International Conference (SusTEM 2017), Alkmaar, June 2017.

Curriculum vitae

Mohammadreza Gaeini was born on September 15th 1985 in Tehran, Iran. He received his Bachelor of Science degree in Chemical Engineering in 2009 at Amirkabir University of Technology in Tehran. He then moved to the Netherlands to study the master program Process Engineering in the Chemical Engineering Department at the Eindhoven University of Technology. In 2012, Mohammadreza finished his Master thesis in the Multiphase Reactors group under the supervision of prof. Hans Kuipers and Dr. Niels Deen, and received his Master of Science degree. In 2013, Mohammadreza started his PhD project in the Energy Technology group in the Mechanical Engineering Department at the Eindhoven University of Technology. The PhD project entitled "Thermochemical seasonal heat storage for the built environment: a multi-scale investigation" was supervised by prof. Herbert Zondag, Dr. Camilo Rindt and Prof. David Smeulders. The results of his research are presented in this dissertation